Ab-initio simulations of the intrinsic Deformation Mechanisms in Body Centered Cubic Al-Cr-Mo-Nb-Ti and Hf-Nb-Ta-Ti-Zr alloys

Zur Erlangung des akademischen Grades eines

DOKTORS DER INGENIEURWISSENSCHAFTEN
(Dr.-Ing.)

von der KIT-Fakultät für Maschinenbau des
Karlsruher Instituts für Technologie (KIT)

angenommene

DISSERTATION

von

M.Sc. Korbinian Wendelin Deck

Tag der mündlichen Prüfung:	08.12.2023
Hauptreferent:	Prof. Dr. mont. Christoph Kirchlechner
Korreferent:	Dr. Christian Brandl

Kurzfassung

Hochentropie Legierungen (*engl.* High Entropy Alloys (HEA)) bestehen aus mehreren Legierungselementen. Diese Legierungsklasse ist seit einigen Jahren im Fokus aktueller Forschung, da einiger ihrer Verteter exzellente mechanische Eigenschaften besitzen. Kubisch raumzentrierte hochentropie Legierungen gelten als vielversprechende Kandidaten für Hochtemperaturanwendungen, da einige Vertreter auch bei hohen Temperaturen eine vergleichsweise hohe Festigkeit aufweisen. Jedoch ist neben der hohen Festigkeit, häufig auch eine hohe Sprödigkeit bei Raumtemperatur in dieser Legierungsfamilie zu finden, was einem Einsatz in kritischen Bauteilen entgegensteht. Bis heute sind die Hintergünde dieser Sprödigkeit nicht vollständig verstanden. Daher behandelt die vorliegende Arbeit systematisch die Deformationsmechanismen in den beiden Besipiellegierungen AlCrMoTi und HfNbTiZr. Beide weisen bei Raumtemperatur eine vergleichsweise hohe Festigkeit auf. AlCrMoTi ist jedoch bei Raumtemperatur spröde und HfNbTiZr duktil. Die Diskussion der Deformationsmechanismen efolgt auf Basis von Modellen aus der Versetzungstheorie. Die benötigten Modelparameter wurden mit Hilfe von ab-initio Rechnungen gewonnen, welche auf der Dichtefunktionaltheorie basieren.

Abstract

High entropy alloys (HEA) consist of several alloying elements. This class of alloys has been the focus of current research for several years, as some of its representatives have excellent mechanical properties. Body-centered cubic (BCC) HEA are considered promising candidates for high-temperature applications, as some representatives exhibit comparatively high strength even at high temperatures. However, in addition to their high strength, this family of alloys is often highly brittle at room temperature, which makes them unsuitable for use in critical components. To date, the reasons for this brittleness are not fully understood. Therefore, this thesis systematically examines the deformation mechanisms in the two example alloys, AlCrMoTi and HfNbTiZr. Both exhibit comparatively high strength at room temperature. However, AlCrMoTi is brittle at room temperature, and HfNbTiZr is ductile. The discussion of the deformation mechanisms is based on models from dislocation theory. The required model parameters were obtained using ab-initio calculations based on density functional theory.

Contents

1 Introduction

The term *High Entropy Alloys* (HEA) defines a new material class, primarily by containing alloys with five or more elements in equimolar or near equimolar composition. This material class has attracted increasing attention in the past years due to the outstanding material properties of some of its members[1]. The subfamily of body-centered cubic (BCC) HEA is the focus of recent research since it contains promising candidates with outstanding mechanical properties[1,2]. Some BCC HEA retain high yield strength up to 1600°C[3]. This is remarkable since Ni-based superalloys have excellent mechanical properties at temperatures up to 1000 °C, but their use at higher temperatures is limited[2]. Other BCC HEA show a unique combination between high yield strength and room temperature ductility[4]. The combination of high yield strength and room temperature ductility is particularly interesting because BCC HEA usually show brittle to ductile transition temperatures above room temperature[1]. The connection between strength and ductility and the chemical composition of a HEA still needs to be fully understood and is thus the focus of recent research[2,1]. For example, Al-Cr-Mo-Nb-Ta-Ti and Hf-Nb-Ta-Ti-Zr alloys show comparable high yields strengths, but Al-Cr-Mo-Nb-Ta-Ti-alloys are room temperature brittle[5] and Hf-Nb-Ta-Ti-Zr alloys are room temperature ductile[4,6,7,8].

Experimental studies indicated that the room temperature brittleness of Al-Cr-Mo-Nb-Ti alloys is connected to a B2-type ordered phase existing at temperatures $\lesssim$ 1000°C[9,10]. But the exact elemental manifestation of the B2-type ordered structure and how crystallographic order could influence the deformation behavior of BCC HEA remains unclear.

Based on the assumption that dislocations mediate plastic deformation in HEA, the question arises if and how the appearance of chemical ordering changes their mobility through the crystal matrix. On the one hand, introducing B2-type chemical ordering changes the system's shortest lattice translation invariance, which determines possible Burgers vectors and affects glide system selection[11,12].

In B2-ordered alloys, gliding dislocations create deformation-induced anti-phase boundaries (APB)[11]. The creation of APBs causes a restoring stress opposing dislocation glide. The restoring stress correlates with the anti-phase boundary energy (APBE)[11,12]. The magnitude of the APBE in the Al-Cr-Mo-Nb-Ti system and the influence of chemical fluctuations along the crystal matrix have yet to be investigated[11]. Consequently, the influence of the APBE on the strength of Al-Cr-Mo-Nb-Ti alloys remains unclear[11].

Moreover, chemical order could influence other material properties, which are either connected to dislocation properties (e.g., the dislocation line energy) or the dislocation matrix interaction. For example, chemical order could influence the elastic tensor and the magnitude of lattice distortions in BCC HEA.

Until today, no study exists that showed an unambiguous connection between crystallographic ordering and room temperature brittleness in BCC HEA, which may be linked to the experimental difficulties in characterizing ordering in HEA. Therefore, the effect of chemical ordering on room temperature brittleness in BCC HEA remains unclear.

Of course, besides chemical ordering, other aspects could explain the high yield strengths and room temperature brittleness of BCC HEA. In BCC metals and alloys, the observed high room temperature yield strengths are explained by the low screw dislocation mobility in these materials[13,14,12]. The low screw dislocation mobility is explained by a substantial potential barrier against screw dislocation glide, i.e., the Peierls potential[15]. The Peierls potential denotes a barrier against dislocation motion and results from a periodic variation of the dislocation core energy[16]. In BCC metals, the nonplanar core of screw dislocations represents a sessile core configuration, which has to be transformed into a glissile configuration to move the dislocation[17,18,19].

The Peierls potential and the resulting low screw dislocation mobility also explain the strong temperature dependence of yield strength of conventional BCC metals and alloys since thermally activated plasticity predicts that thermal energy can support dislocations to overcome the Peierls potential[13,12,20]. Hence, the necessary stress to move a dislocation, i.e., the Peierls stress, increases for low temperatures around room temperature and reduces for higher temperatures [13,12,20]. The reduced screw dislocation mobility in conventional BCC metals and alloys at low temperatures can bring the low-temperature flow stress to levels at which other mechanisms than dislocation slip, namely twinning and fracture, took over [21].

A well-established theory for describing thermally activated plasticity in BCC metals is the kink pair nucleation theory [21]. Kink pair nucleation theory predicts that partial overlaps of the dislocation line from one Peierls valley into the neighboring one (i.e., a double kink) reduce the flow stress since the resulting non-screw elements can glide with lower flow stress along the screw dislocation line [21]. The necessary amount of energy to form a double kink (i.e., the double kink formation enthalpy) determines the dependence of the flow stress on temperatures and applied strain rate [13]. The flow stress dependence of the kink pair formation energy (or another activation energy) defines the so-called activation volume [13]. The activation volume can be determined by temperature and strain rate-dependent flow stress measurements and can consequently be used to identify the dominant deformation mechanism at a specific temperature [13,21]. Thermal energy can support the advance of immobile screw dislocations by forming kink pairs [21]. Kink pair nucleation theory further predicts that a temperature exists, providing enough energy to form double kinks without external stress contribution (i.e., the knee temperature) [22]. Consequently, the knee temperature denotes a thermal-athermal transition temperature of the flow stress. Experimentally determined temperature-flow stress curves and activation volumes of BCC metals are consistent with kink pair nucleation theory [22,23,24,25,26].

Experimental findings found strong indications also in BCC HEA a Peierls barrier exists, reducing screw dislocation mobility. Transmission electron microscopy (TEM) observed mainly long and straight screw dislocations in BCC HfNbTaTiZr [7,27], which is consistent with experimental results from pure BCC metals and dilute BCC alloys [28,29,30,31]. The measured activation volumes of 20-50 b^3 are in the range of activation volumes measured for BCC metals (see, e.g., [20]). Consequently, the observation of long straight screw dislocations and the measured activation volumes in HfNbTaTiZr propose that they have the same deformation mechanisms as BCC metals and dilute BCC alloys.

Moreover, experiments observed temperature-dependent flow stress at low temperatures and a thermal-athermal transition at high temperatures in several BCC HEA[32] similar to observations from BCC metals[22,23,24,25,26]. However, although the experiments found similar temperature-flow stress profiles in BCC metals and HEA, the experiments also showed that HEA have higher flow stresses than BCC metals from low to high temperatures[32]. Identifying the reason for the high flow stress of BCC HEA is the focus of recent research[2,1].

In contrast to the findings of mainly long straight screw dislocations, after plastic deformation for HfNbTaTiZr[7,27], other studies found a significant amount of non-screw-dislocations during deformation in the BCC random alloys MoNbTi, NbTaTiV, and CrMoNbV[33,34]. The significant amount of non-screw-dislocations during deformation indicates that in some BCC HEA, the mobility of edge dislocations also plays a decisive role.

Identifying the reasons behind the higher yield strengths in BCC HEA compared to BCC metals and conventional alloys[32] and low edge dislocation mobility in some BCC HEA[33,34] is still the focus of recent research. There exist several solid solution strengthening (SSS) theories aiming to describe plastic deformation in BCC HEA[35,36,37]. Table 1.1 provides an overview about three SSS theories: The Maresca-Curtin (MC) theories and the Rao theory.

1.1 Strength Models

The solid solution strengthening (SSS) theories from Table 1.1 consider every atom within the random matrix as a solute atom; hence, the HEA is at 100% solute concentration. The SSS theories assume that the interaction between dislocations and solute fluctuations within the crystal matrix reduces dislocation mobility and causes strengthening. However, the MC-I and the Rao theory are focused on the interaction of screw dislocations and the random crystal matrix, and the MC-II theory is focused on edge dislocation - random matrix interactions. Within the Rao theory[37], kink pair nucleation does not create a barrier for dislocation mobility; the only relevant deformation mechanism is kink glide. The flow stress

Theory	Focused dislocation type	Key deformation mechanisms
MC-I[35]	Screw dislocations	Cross-Kink failure Peierls-type motion Lateral kink glide
MC-II[36]	Edge dislocations	Dislocation glide
Rao[37]	Screw dislocations	Lateral kink glide

Table 1.1: Overview of recent solid solution strengthening (SSS) theories for BCC HEA.

results from different solutes entering and leaving the dislocation core during lateral kink glide[37]. Thus, the double-kink nucleation energy and, consequently, the single-kink energy E_k do not play a role in this theory.

The MC-I model considers screw dislocations as pre-kinked caused by energetically favorable and unfavorable environments resulting from chemical fluctuations (see Figure 1.1). Based on the pre-kinked structure, the MC-I model considers three different mechanisms as rate controlling: Peierls mechanism, kink glide (similar to the Suzuki model), and cross-kink breaking (see Figure 1.1). The individual flow stresses resulting from the different mechanisms highly depend on a length parameter describing the typical distance between two kinks. This parameter depends on the dislocation/solute interaction parameter $\Delta\tilde{E}_p$ and the single kink energy E_k. The theories from Table 1.1 are consistent with various experimental results. A comparison between the yield strengths of several BCC HEA from the Rao model and experimental values revealed a standard error of 13%[37].

The MC-I theory could deliver reasonable temperature-dependent flow stress results for BCC Fe_{1-x}-Si_x alloys in the dilute limit ($x = 5 - 8\%$) and for BCC $\mathrm{Nb}_{1-x}\mathrm{Mo}_x$ for $x = 5 - 25\%$[35]. The MC-I model further showed consistent flow stress results for two TiNbZr-alloys, however, with limited experimental data points[35]. A comparison between results from the MC-I model with experimental results corresponding to HEA (with four elements or more) is lacking because determining the needed input parameter is difficult[35].

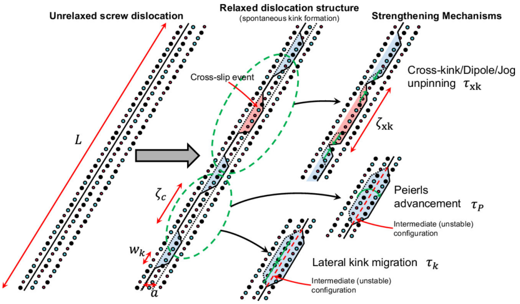

Figure 1.1: Figure from[35]. Predicted structure and motion of a screw dislocation from the MC-I model[35]. A long straight screw dislocation minimizes its energy by adopting a pre-kinked structure to energetically favorable and unfavorable environments. Blue-shaded areas denote kinks on one plane, and red-shaded planes denote kinks on different planes (cross-slip events).

The edge strengthening mechanism predicted by the MC-II model can rationalize the high yield strengths of MoNbTaW and MoNbTaVW at temperatures over half the melting temperature $> 0.5T_M$. However, observing long straight screw dislocations in deformed HfNbTaTiZr at room temperature shows that the MC-II model is inconsistent with the low edge dislocation mobility assumption in HfNbTaTiZr. Quantitative deviations between theoretical predictions from the SSS models and experimental data could evolve from the limited accuracy of the used screw dislocation/solute interaction parameter $\Delta\tilde{E}_p$ and the single kink energy calculated by Molecular Dynamics (MD) simulations[35,36,37]. Density functional theory (DFT) calculated $\Delta\tilde{E}_p$, and E_k could improve the accuracy of the model predictions[35]. Consequently, reduced models are supposed to use input parameters accessible by DFT calculations[37,38]. A reduced model (initially proposed in[37]) agrees well with the screw dislocation/solute interaction energy within the molecular statics framework. The reduced model approximates $\Delta\tilde{E}_p$ by the interaction energy between the unstable stacking fault (USF) at $\frac{1}{6}[111]$ and a solute atom. The advantage of the reduced model is that it can be applied within a DFT framework due to its reduced complexity.

The importance of the $\frac{1}{6}[111]$ USF/solute interaction energy indicates a strong influence of the generalized stacking fault energy (GSFE) on dislocation mobility.

A combined experimental and MD simulations study showed that GSFE fluctuations serve as dislocation pinning points in face-centered cubic (FCC) HEA[39]. However, a systematic investigation of the GSFE of BCC HEA and the implications on the strength is lacking. This might be connected with difficulties in calculating GSFE of HEA evolving from the random crystal lattice (see Section 2.5).

Further, a reduced model within the MC-II theory to determine the edge dislocation/solute interaction energy ΔE_b has been proposed[36]. Within the reduced model, ΔE_b is approximated by the elastic interaction between the dislocation and the misfit volume caused by the solute atom[36]. The advantage of the reduced model is that all necessary parameters are accessible by DFT calculations or even experimentally. However, neglecting other contributions to ΔE_b (e.g., non-elastic contributions) also reduces the accuracy[36].

Since the atomic misfit parameter used by the reduced model and the atomic size difference (ASD) are linearly correlated, the reduced model can explain the observed correlation between hardness and ASD[5]. The observed correlation implicates a dominant role of edge dislocation mobility for the flow stress within the investigated Al-Cr-Mo-Nb-Ti HEA.

Besides the difficulties with inaccurate input parameters, all presented SSS theories might suffer from the fact that they are based on the assumption of a perfectly random crystal matrix. Thus, they did not consider the effects of chemical ordering. But at least some BCC HEA show evidence of chemical ordering at room temperature[9,10,40].

1.2 Outline

Based on the presented state of the art, this work elaborates intrinsic deformation mechanisms of different BCC HEA. This work systematically investigates material parameters linked to deformation mechanisms, mainly in room-temperature brittle BCC Al-Cr-Mo-Nb-Ti and ductile Hf-Nb-Ta-Ti-Zr HEA. The material parameters are calculated by DFT.

Chapter 2 introduces the calculation methods used. Chapter 3 investigates the chemical order-disorder phase formation behavior of AlCrMoTi and HfNbTiZr. Chapter 4 presents and discusses the DFT-calculated material parameters of different BCC HEA. Finally, Chapter 5 discusses the calculated material properties in the context of deformation mechanisms by applying and comparing different models from dislocation theory.

2 Simulation methods

2.1 Density Functional Theory

This work aims to study the influence of the distinct chemical composition of BCC HEA on their intrinsic deformation mechanisms. Since plastic deformation in BCC metals and alloys is supposed to be carried by dislocations, this work uses models from dislocation theory to predict deformation mechanisms. Hence, input parameters from Density Functional Theory (DFT) calculations are necessary for applying dislocation models in this work. The advantage of the DFT approach is that it generates input parameters (e.g., elastic constants or stacking fault energies) faster and more cost-efficient than experimental methods. Cost-efficient approaches are crucial in the case of HEA since only time and cost-efficient approaches allow the exploration of the vast composition space.

The DFT calculations are performed by the Vienna ab Initio Simulation Package (VASP)[41,42]. VASP is a simulation package that can calculate electronic ground state properties using DFT.

DFT is an *ab initio* approach based on the Hohenberg-Kohn Theorem[43]. It shows the existence of an energy functional $E[\rho]$, which reveals the exact ground state energy to the corresponding exact ground state density:

$$E_0 = E[\rho(r)]. \tag{2.1}$$

The functional E reaches its minimum for the exact density ρ, which yields a variation principle to determine ρ and the ground state energy.

This theory allows the description of a many-body system by its particle density $\rho(\vec{r})$. This reduces the 3N-dimensional problem ($\psi(\vec{r}_1, \vec{r}_2, ..., \vec{r}_N)$) to an 3 dimensional problem $\psi(\vec{r})$. Hence, the Hohenberg-Kohn Theorem reduces the complexity of the many-body problem without an approximation. This work was extended in 1965 by the Kohn-Sham-theory[44], which delivers an ansatz to define the density functional.

Defining the density functional is challenging, and it is for real crystal systems only possible with approximations. The crucial point is the exchange-correlation energy functional $E_{\text{xc}}[\rho]$. It contains all non-classical interaction effects, which cannot be determined since that would equal solving the many body problem. Theoretically $E_{\text{xc}}[\rho]$ depends on $\rho(\mathbf{r})$ at every point $\mathbf{r}$, which leads to enormous complexity. Thus, the local density approximation (LDA) and the generalized gradient approximation (GGA) have been developed. The exchange-correlation energy is approximated within the LDA by the homogenous electron gas. DFT calculations with the LDA tend to overestimate the binding strength. The GGA includes the electron density gradient to reduce the error. Both approximations deliver reliable results for weakly interacting electron systems like metals[45].

Although DFT offers good accuracy for metals and alloys, it is computationally costly and has limitations. First, it suffers from a significant systematic underprediction of a BCC shear modulus C_{44} and a systematic overprediction of the Peierls stress[46]. DFT is further only defined at $T = 0\text{K}$[45]; hence, the derived values for some properties may deviate from the values corresponding to higher temperatures. The high computational costs of DFT calculations prohibit the direct study of extended defects in HEA since sampling much larger supercells compared to conventional materials is necessary due to their compositional fluctuations[46].

Therefore, this work does not directly study dislocation structures within DFT since the required material quantities like lattice constants, elastic constants, stacking fault energies, and atomic misfit volumes will be computed and used as input parameters for dislocation theory models to predict macroscopic material parameters, for example, strength and ductility.

2.2 Simulation setup

The first step of performing electronic structure calculations is the definition of the crystal lattice. Since VASP uses periodic boundary conditions, one has to define a unit cell containing lattice vectors and atomic positions. In the case of elemental BCC materials, this process can be done by defining a primitive unit cell (e.g., Figure 2.1 a).

Defining a lattice structure is difficult for random alloys, where different elements randomly occupy the lattice sites. Since the random site occupation breaks the translation invariant within the HEA crystal lattice, a unit cell of infinite size would be necessary to model the true random state. The virtual crystal approximation (VCA) and the site coherent-potential approximation (SCPA)[47] have been developed to address this problem.

The VCA considers the alloy to have only one averaged atom type, and the SCPA treats all elements equivalently surrounded by a uniform effective medium. Therefore, both theories are beneficial for mean-field approaches, which are also used by atomistic simulations of dislocations in HEA[48].

The VCA method can calculate material parameters (e.g., the elastic tensor) from unit cells containing only one atom, which reduces computational costs compared to larger supercells with explicit disorder. However, the application of this approach is generally limited to systems where the local environmental-dependent effects (e.g., local lattice distortions) can be neglected[49].

This limitation has been addressed by investigating structural defects like local lattice distortions by the insertion of solute atoms into the mean matrix[48]. The calculations are repeated several times for the different types of solute atoms, which reduces the efficiency of the VCA approach. The fact that calculations involve supercells consisting of more than one atom to avoid artifacts evolving from the interactions through periodic boundary conditions further reduces the efficiency of the VCA approach. Hence, for complex problems that depend on the actual lattice structure, the advantages of structural approaches where supercells consisting of the different types of atoms model the crystal lattice emerge. In contrast to the non-structural VCA approach (consisting of only one sort of average atoms), a simple structural approach is the definition of supercells containing N atoms randomly distributed on the lattice sites. The atomic positions can be relaxed by minimizing the total energy and, in a second step, used to determine quantities like the elastic constants and stacking fault energies. The disadvantage of this procedure is that different individual structures will lead to different results, deviating from the actual random alloy. The emerging error decreases with an increasing number of atoms in the supercell. However, the statistical limit is approached very slowly ($N^{\frac{1}{2}}$ even in the case of a binary random alloy[50]). Therefore, one can either repeat the DFT calculations with a set of configurations or define a large supercell (10^3 atoms). Since both approaches are computationally expensive, special quasi-random structures (SQS) have been developed.

2.2.1 Special quasi-random structures

An SQS is a supercell constructed in a way that mimics for finite size (N atoms) the correlation functions of a random alloy better than a supercell of the same size with randomly distributed atoms. The underlying theory[50] has been extended to multicomponent sublattice alloys in[51]. The Alloy Theoretic Automated Toolkit (ATAT)[51] is used to generate the SQS supercells. During the SQS generation, the algorithm searches for the periodic unit cell in which the next neighbor correlations are closest to the random structure. However, periodic structures always insert

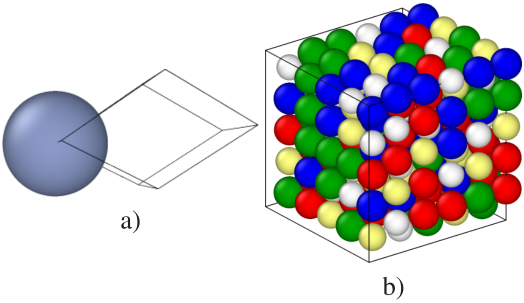

Figure 2.1: a) Primitive unit cell and b) SQS supercell.

correlations beyond a certain distance[50]. Therefore, in the generated SQS, these so-called "periodicity errors" are deferred from the next neighbor shells to more distant ones.

Periodicity errors can be reduced by increasing the size of the SQS, but the time to find the SQS increases with increasing N. Another significant drawback of using larger SQS is the O(N^3) scaling of the computational costs to the DFT calculations. Hence, it is worth investigating the impact of periodicity errors on the calculated physical quantity by repeating the same calculation with different SQS of the same size. The standard deviation of such calculations can be used to measure the periodicity error. Increasing the cell size should reduce the standard deviation, and the mean values of different-sized sets of SQS should converge at a specific size. In this manner, computational costs and periodicity errors are minimized. The small set of ordered structures (SSOS) offers a more advanced and systematic method.

2.2.2 Small set of ordered structures

The cluster expansion (CE) is a successful method to model the thermodynamics of multicomponent systems[52]. The small set of ordered structures (SSOS) concept uses CE and enables very efficient ab initio calculations[49]. The basic idea is to reduce the number of atoms involved in the calculations due to the $O(N^3)$ scaling of DFT calculations. Hence, a physical property f of a random alloy can be calculated from a weighted average of the same property calculated with a small set of ordered structures σ_i^{SSOS}

$$\langle f \rangle_R \approx \sum_{i=1}^{n} \omega_i f(\sigma_i^{\mathrm{SSOS}}), \tag{2.2}$$

with the number of structures n and the weights ω_i[49]. In the case of a five-component HEA, a small SSOS (see Figure 2.2) can mimic the first few neighbor shells as precisely as a comparable large SQS (125 atoms)[49]. Thus SSOS provides an efficient method to compute every material property, which can be

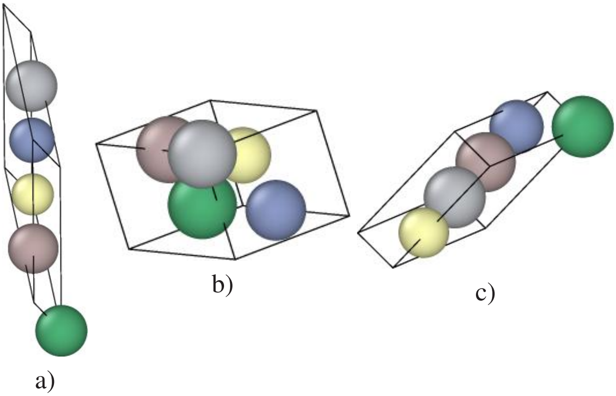

Figure 2.2: Small Set of Ordered structures for a five-component BCC HEA.

modeled by a short-range cluster expansion[49]. For instance, the SSOS approach is suitable for calculating lattice constants or elastic constants of multicomponent random alloys (Appendix A.2).

2.3 Structure optimization

Before starting to calculate material properties, the used lattice structure modeled by the SQS (or SSOS) has to be relaxed into its equilibrium structure. The conjugate gradient algorithm is applied for the relaxation, already implemented in VASP[53].

The Broyden–Fletcher–Goldfarb–Shanno (BFGS) algorithm from the Atomic Simulation Environment[54] was used during running stacking fault energy calculations for structure optimizations. The optimization process itself can be performed with different degrees of freedom. For example, depending on the investigated property and the symmetry of the investigated material, either full relaxations with respect to cell shape and volume as well as the single atomic positions or relaxations with a limited degree of freedom can be necessary.

An essential detail of the relaxation process is the applied convergence criteria.

This work mainly used force criteria of $0.01\mathrm{eV}/\text{Å}$ as the maximum force on every single atom. Alternatively, one can use an energy criterion, which stops the calculation, if the energy difference between ionic relaxation steps is below the chosen value ($1\mathrm{meV}$ per atom).

2.4 Calculation of elastic constants

Calculating the elastic tensor is an integral part of this work since it serves as an input quantity to calculate dislocation properties, e.g., the dislocation line energy. Experimental results for single crystal HEA are rare and revealed mainly by ultrasonic measurements on polycrystals yielding isotropic elastic constants[6,5]. This work applies the SQS or SSOS approach to compute the elastic constants of HEA. Here, some care should be taken that in contrast to unit cells from the VCPA approach, the SQS (and SSOS), in principle, break the cubic symmetry. Since the actual material should have cubic symmetry, an averaging approach can map the non-cubic elastic tensor onto a cubic representation[55]. This method calculates the cubic elastic constants as an average over the cubic equivalent elastic constants

$$\overline{C}_{11} = C_{11} + C_{22} + C_{33} \tag{2.3}$$

$$\overline{C}_{12} = C_{12} + C_{13} + C_{23} \tag{2.4}$$

$$\overline{C}_{44} = C_{44} + C_{55} + C_{66}. \tag{2.5}$$

The deviation from cubic symmetry will also be reflected in the fact that the equilibrium cell shape of the SQS might be only partially cubic. Nevertheless, this effect should converge to zero with increasing cell size.

This work used the following method for the determination of elastic constants: The SQS is relaxed regarding atomic positions, cell volume, and shape to avoid artificial stresses, which could influence the elastic constant calculation.

Two different ways can perform the calculation of the individual elastic tensor entries:

- Using a routine already implemented in VASP. This routine performs a symmetry-dependent number of finite distortions on the lattice and determines the elastic constants by a linear fit on the resulting strain-stress relation[56].
- Using a polynomial fit on the resulting energy-strain relation[57]. This approach can measure inharmonic contributions (e.g., third-order elastic constants).

Comparisons within this work revealed that the choice of the calculation method does not influence the constant elastic results (see Appendix A.1).

2.5 Generalised stacking fault energies

Another essential material property calculated and used within this work is generalized stacking fault energy (GSFE), often denoted as γ-surface. The concept of GSFE computes the energy density change by rigidly shifting two half lattice relatives to each other to mimic dislocation slip on a defined slipe plane[58]. Dislocation slip occurs in the direction of the shortest lattice translation invariant (i.e., the Burgers vector b). The slip planes are usually the planes with the highest atom density[13]. For pure BCC metals, the Burgers vector is $b = \frac{a_0}{2}\langle 111\rangle$, and the most relevant slip planes are $\{110\}$-, $\{112\}$- and $\{123\}$-planes. The γ-surface is calculated by

$$\gamma(\mathbf{x}) = \left(E_0 - E(\mathbf{x})\right)/A. \tag{2.6}$$

E_0 denotes the energy of the initial structure, while $E(x)$ is the structure's energy with a given relative shift $\mathbf{x}$ in a fault plane with area A. The method uses the following protocol: The crystal is virtually cut along the considered glide plane. Subsequently, the upper half is displaced with respect to the lower half by the displacement vector $\mathbf{x}$. The corresponding calculation routine is frequently explained in the literature for pure metals and intermetallics (e.g.,[59]). This section will focus on the specific details corresponding to the peculiarities of the GSFE calculations in HEA. Due to Neumann's principle, $\gamma(x)$ shares the

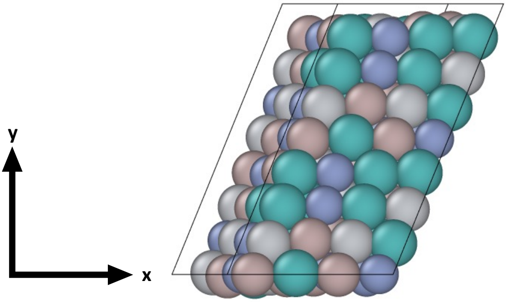

Figure 2.3: SQS supercell with dimensions $4 \times 8 \times 4$ representing the lattice of a four-component BCC HEA used for GSFE calculation.

periodicity of the crystal lattice. Consequently, the function $\gamma(x)$ (with a shift x in b-direction) of a perfect BCC lattice consisting of only one atom sort is b-periodic with maxima at $\frac{nb}{2}$ (unstable stacking faults) and minima at nb (stable stacking faults).

However, for random alloys, the situation is more complex. While modeling the random lattice by a CPA approach preserves the b-periodicity, the usage of the SQS approach leads to a sampling of chemical fluctuations by $\gamma(x)$ along the fault direction. Consequently, $\gamma(x)$ depends on the specific atomic configuration, which varies along the displacement path. It still has local maxima and minima at nb and $\frac{n}{2}b$, but the b-periodicity is broken. The influence of chemical fluctuations is expected to average in the limit of an infinite large fault plane. The resulting GSFE $\overline{\gamma}(x)$ corresponds to a conceptual mean alloy and is supposed to be b-periodic. The average can be performed over the same SQS cell by calculating several $\gamma_i(x)$, where the index i denotes different symmetry equivalent fault planes and taking the average

$$\overline{\gamma}(x) = \sum_{i=1}^{N_p} \gamma_i(x), \tag{2.7}$$

with the number of fault planes N_p.

Figure 2.4 shows three example γ-surface cross-sections $\gamma_1(x)$, $\gamma_2(x)$, $\gamma_2(x)$ from three different $\{110\}$-planes and the corresponding averaged function $\overline{\gamma}(x)$

of an SQS representing the BCC HEA AlCrMoTi (see Figure 2.3). Thus, the $4b$ displacement corresponds to the total displacement of the SQS along the x-direction in a $\{110\}$-plane. The curves vary around their mean curve, which

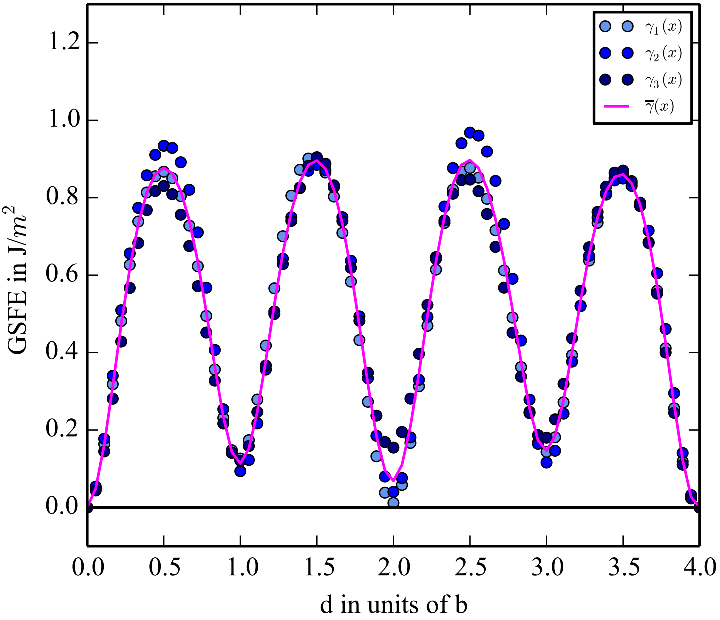

Figure 2.4: Two example γ-surface cross-sections of two symmetry equivalent fault planes within the same SQS. Points denote stacking fault energies with respect to displacement b. Lines are to guide the eye

seems almost b-periodic. However, with the difference, the minima at b, $2b$, and $3b$ show values above zero. The deviation from the b-periodicity is caused by the appearance of lattice distortions in the random crystal matrix, where lattice distortions lead to an additional energy contribution on the γ-surface since the fault is introduced in an already relaxed SQS. Shifting the upper half of the crystal with respect to the lower one changes the spatial arrangement of elements within the crystal matrix. The resulting structure is at its energetic minimum once all

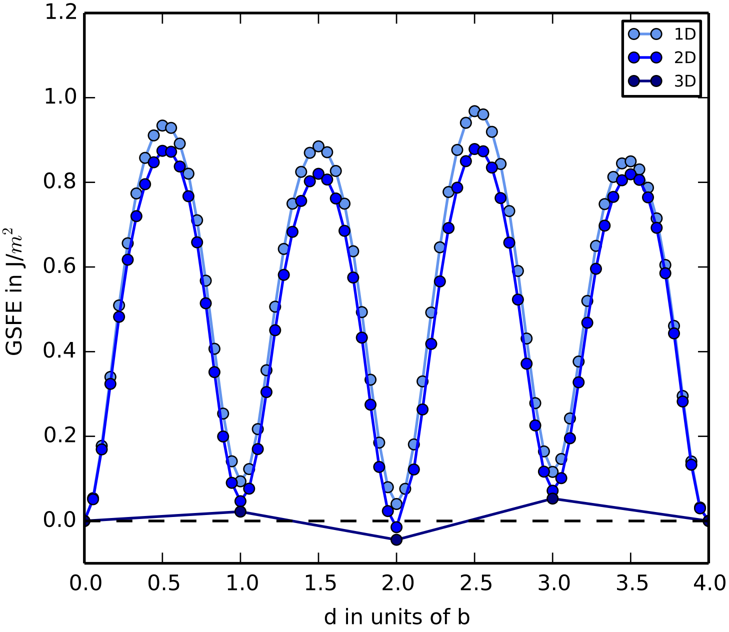

Figure 2.5: γ-surface cross sections of disordered AlCrMoTi calculated with different degrees of freedom (light blue: 1D, blue: 2D, dark blue: 3D)

atomic positions are relaxed in their new minimum positions. However, during the γ - surface calculation process, relaxations of the atomic positions are restricted, which leads to the additional energy contribution $\Delta E(x)$ yielding

$$\gamma'(x) = \gamma(x) + \Delta E(x). \tag{2.8}$$

Figure 2.5 compares GSFE with different degrees of freedom (1D, 2D, 3D) during the calculation process. The data demonstrate that the GSFE decreases with an increasing degree of freedom. The stable stacking fault values γ_{sf}, which denote the GSFE for $x = nb$, fluctuate around zero if total relaxations (3D) are allowed. Although this is the expected behavior for a disordered structure, it raises the question of how E_0 can be defined reasonably. Figure 2.5 shows that the energy of the initial structure ($x = 0$) was chosen as E_0. Considering that in the case of a disordered alloy, the energies due to displacements $x = nb$ are equivalent, the choice of $E_0 = \gamma(0)$ is ambiguous.

To address the discussed peculiarities of HEA GSFE, this work established the following workflow for the GSFE determination in random alloys. First, a set of discrete displacements $x_i \in [x_0, x_1, x_2, \ldots, x_N]$ is applied on the SQS and the corresponding energies $E^{\text{1D}}(x_i)$ are generated by minimizing the energy of the displaced structures by 1D relaxations. Displacement with even indices belong to local minimum energy positions $x = nb$ and displacements with uneven indices belonging to maximum energy positions $x = \frac{n+\frac{1}{2}}{b}$. In the second step, the energy calculations are repeated using 3D-relaxations yielding $E^{\text{3D}}(x_i)$. Then, the energy differences between 1D- and 3D-relaxed structures are determined by

$$\Delta E^{\text{1D-3D}}(x_{2n}) = E^{\text{1D}}(x_{2n}) - E^{\text{3D}}(x_{2n}). \tag{2.9}$$

The energy differences are used as correction terms for the maximum energies calculated from 1D-relaxed SQS. The maximum energies calculated by 1D-relaxations are corrected by the mean energy differences of the two neighboring minimum energy positions

$$E^{\text{c}}_{\text{max}}(x_{2n+1}) = E^{\text{1D}}_{\text{max}}(x_{2n+1}) - \frac{\Delta E^{\text{1D-3D}}(x_{2n}) + \Delta E^{\text{1D-3D}}(x_{2n+2})}{2}. \tag{2.10}$$

The calculations are performed on symmetric equivalent glide planes within the same SQS.

The next step depends on whether the structure has a b (disordered lattice) or a $2b$-periodicity (B2-type ordered lattice) in the displacement direction **b**. Sections 2.5.1 and 2.5.2 propose methods for describing these two specific cases.

2.5.1 Crystallographic disordered BCC structures

As stated in the previous section, the unstable stacking fault energy configuration can not be fully relaxed (3D relaxation). In order to incorporate this effect, a b-periodic γ-surface is enforced by approximating it by the periodic function

$$\gamma(x) = \overline{\gamma}_u \sin^2\left(\frac{x\pi}{b}\right). \tag{2.11}$$

The unstable stacking fault energy γ_u is determined by averaging the differences of neighboring minimum and maximum energies:

$$\gamma_u^{\pm}(x_{2n+1}) = E_{\text{max}}^{\text{c}}(x_{2n+1}) - E_{\text{min}}^{\text{3D}}(x_{(2n+1)\pm 1}). \tag{2.12}$$

Fluctuations can be considered by the corresponding standard deviation or by observed minimum and maximum values of γ_u.

2.5.2 Partially B2-type ordered structures

As previously stated, the shortest lattice invariant (Burgers vector b) in B2-type ordered lattices is twice that of disordered BCC lattices ($2b$). Thus, the GSFE of $2b$-periodic structures are approximated by the function

$$\gamma(x) = \overline{\gamma}_s \sin^2\left(\frac{x\pi}{2b}\right) + (\overline{\gamma}_u - \overline{\gamma}_s/2)\sin^2\left(\frac{x\pi}{b}\right), \tag{2.13}$$

with the average unstable stacking fault energy $\overline{\gamma}_u$ and the average stable stacking fault energy $\overline{\gamma}_s$. The average unstable stacking fault energy $\overline{\gamma}_u$ is determined by averaging all differences of neighboring minimum energies, which correspond to structures restoring the initial crystal structure and all maximum energies:

$$\gamma_u^{\pm}(x_{(4n+2)\pm 1}) = E_{\text{max}}^{\text{c}}(x_{(4n+2)\pm 1}) - E_{\text{min}}^{\text{3D}}(x_{(4n+2)\pm 2}). \tag{2.14}$$

The stable stacking fault energies are calculated by averaging the difference between energies corresponding to stable stacking fault positions and energies corresponding to neighboring positions, which restore the initial crystal structure:

$$\gamma_s^{\pm}(x_{4n+2}) = E^{\text{3D}}_{\text{min}}(x_{4n+2}) - E^{\text{3D}}_{\text{min}}(x_{(4n+2)\pm 2}). \tag{2.15}$$

3 Crystallographic ordering in AlCrMoTi and HfNbTiZr

The emergence of a new material class of High Entropy Alloys (HEA) opened up an enormous materials design space[60]. Combining elements beyond the traditional alloying paradigm with a majority base element and minority alloying elements to tune materials properties allows unprecedented materials properties (e.g., strength-ductility trade-off) or tuning of materials properties. In HEA, the concept of a main alloying base element is not anymore given; instead, the mixture beyond the dilute limit of usually five (and more) different elements functions as a base alloy with an anticipated random elemental distribution on a crystal lattice. Defects like dislocations and solutes and their interactions determine decisive material properties like strength and ductility. It is experimentally established that the fundamental mechanisms and defects operating in HEA are those of standard alloys (see, e.g.,[1]). However, one has to reconsider the concept of the classical definition of such defects since, in HEA, dislocations interact with atomic scale defects created by the random crystal matrix. The concept of *'Design using randomness'* argues that the behaviors of defects in HEA can be modified due to the high degree of atomic randomness[60]. The modification is based on the change of average defect properties at different length scales.

Considering the whole random alloy, with n components at concentrations $c_i = c_1, \ldots, c_n$ yields on average $c_i N$ atoms of type i. However, within a subvolume with several atoms $N' < N$, fluctuations are scaling with $\propto \sqrt{c_i N'}$ around the average value of the actual number of atoms. The actual number of atoms determines the actual defect energy through interaction with a defect, which differs from the average defect energy. Consequently, randomness leads to scale-dependent defect energy fluctuations. In order to minimize the system's energy defects move from high-energy areas to low-energy areas or change their structure.

For instance, Maresca and Curtin argue for BCC HEA that screw dislocations have a pre-kinked dislocation structure minimizing the dislocation-solute interaction energy[35]. The pre-kinked dislocation structure has a typical kink length, which depends on the defect energy fluctuation due to the solute interaction. Based on this picture, a complete theory predicts a typical kink length and the average dislocation properties, which determine the yield strength of the solid-solution alloy with high solute concentration. Therefore, changing the degree of chemical randomness within the crystal matrix can control the mechanical properties of a HEA (e.g., the yield strength).

This work explores the case of BCC Al_xCrMoTi HEA, where the *'Design using randomness'* has already been experimentally tested[9]. AlCrMoTi has a B2-type ordered structure at room temperature and undergoes an order-disorder phase transformation at 1260K[9]. Moreover, Laube et al.[10] showed that a reduction of the Al concentration c_{Al} in Al_xCrMoTi affects the order-disorder transition temperature and even inhibits the formation of the ordered B2 phase if it falls below a critical value. With vanishing ordered B2 phase, the HEA shows more room-temperature ductility.

However, both experimental observations did not reveal the exact elemental manifestation of the ordered lattice structure of AlCrMoTi. Therefore, neither observation can explain the connection between the Al-content and the order-disorder transition. Hence, a theoretical study with atomic resolution is necessary to complete the understanding of the phase formation behavior of AlCrMoTi. Such theoretical studies investigated the phase formation behavior of the BCC HEA MoNbTaW using first principle calculations either to inform free energy models[40,61] or Monte Carlo simulations[62,63]. However, a theoretical investigation of the phase formation behavior of AlCrMoTi is lacking. This work sheds light on this dark spot by calculating the electronic ground state energies of disordered and differently ordered lattice configurations of AlCrMoTi. The calculations have been performed by Density Functional Theory (DFT) calculations. Using a free energy approach allowed the determination of order-disorder transition temperatures depending on the distinct elemental manifestation of the B2-type order[64]. This model describes the free energy by competition between enthalpy and entropy contribution:

$$F_\alpha = E_\alpha - TS_\alpha^{\mathrm{conf}}. \tag{3.1}$$

Since the crystal system aims to minimize its free energy, one expects that decreasing temperature will drive the lattice to undergo a disorder-order phase transition. Here E_α and S_α^{conf} denote the electronic ground state energy and the ideal configuration entropy belonging to the phase α (e.g., disordered, B2-type ordered). According to the free energy model, the critical temperature corresponding to the phase transformation can be calculated by

$$T_c = \frac{\Delta E_{\alpha_1,\alpha_2}}{\Delta S_{\alpha_1,\alpha_2}^{\mathrm{conf}}}, \tag{3.2}$$

with $\Delta E = E_{\alpha_1} - E_{\alpha_2}$ and $\Delta S^{\mathrm{conf}} = S_{\alpha_1}^{\mathrm{conf}} - S_{\alpha_2}^{\mathrm{conf}}$.
In a second step, our work revealed a relation between the electronic free energy of a distinct lattice configuration with its Al-Al and Al-Ti bond shares. Finally, in combination with the free energy approach, this allowed the formulation of a relation between the Al-concentration in Al$_x$CrMoTi and its order-disorder transition temperature. Consequently, the findings of this study support the hypothesis that the Al concentration can control the mechanical properties of Al$_x$CrMoTi by changing the degree of chemical randomness within the crystal matrix.
In addition to analyzing the phase formation behavior in Al$_x$CrMoTi-alloys, this work analyses the free energies of different B2-type ordered lattice configurations of HfNbTiZr. As a result, observing only minor differences between the free energy corresponding to the disordered phase and the free energy of several B2-type ordered phases predicts that this alloy is disordered from RT to high temperatures. Since this is consistent with the experimental analysis of[8], this supports the applicability of the used method.

3.1 Ground state energies of crystallographic disordered and ordered BCC AlCrMoTi and HfNbTiZr

The ground state energies E_0 (per atom) of different crystallographic disordered and ordered lattices of AlCrMoTi are necessary for applying the Free Energy model to predict the phase formation behavior.
The considered crystallographic ordered structures are B2-type and denoted in the following way: The BCC lattice is divided into two simple cubic superlattices, SL1 and SL2 (see Figure 3.1). Here, the denotation (AB)(CD) means that A and B atoms randomly occupy lattice sites within SL1, while C and D atoms randomly occupy lattice sites within SL2. By contrast, (A)(B)CD defines a structure where A-atoms randomly occupy SL1 lattice sites, and B-atoms occupy SL2 lattice sites. The C- and D-atoms randomly occupy the whole BCC crystal lattice.

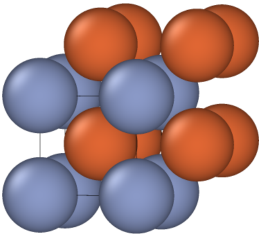

Figure 3.1: BCC supercell divided into two simple cubic superlattices SL1 (red) and SL2 (blue)

DFT calculations determined the ground state energies by relaxing 128 atom SQS with respect to their energy. The different SQS represent the differently ordered and disordered lattice structures. The minimization process relaxed the atomic positions until the system's energy reached the convergence criterion of $1\ \mathrm{meV}$ per atom. In order to minimize the periodicity error, this calculation process has been performed four times with different SQS for each lattice structure. The average energy from different minimized SQS representing the same lattice structure is thus used as the resulting E_0^α of the considered lattice configuration α.

Figure 3.2 shows the resulting ground state energies of possible elemental manifestations of (A)(B)CD and (AB)(CD) ordered lattices of equimolar Al-Cr-Mo-Ti alloys with respect to the ground state energy of the disordered lattice

$$E_0^{\alpha'} = E_0^{\alpha} - E_0^{\text{disordered}}, \tag{3.3}$$

with the excess ordering energy $E_0^{\alpha'}$. The data reveal a hierarchical structure reaching from negative to positive $E_0^{\alpha'}$. The (AlMo)(CrTi)-ordered lattice configuration has the lowest $E_0^{\alpha'}$ with -37 ± 5 meV per atom and the (AlTi)(CrMo)-ordered lattice configuration has with $E_0^{\alpha'} = 54 \pm 15\ \mathrm{meV}$ per atom the highest one.

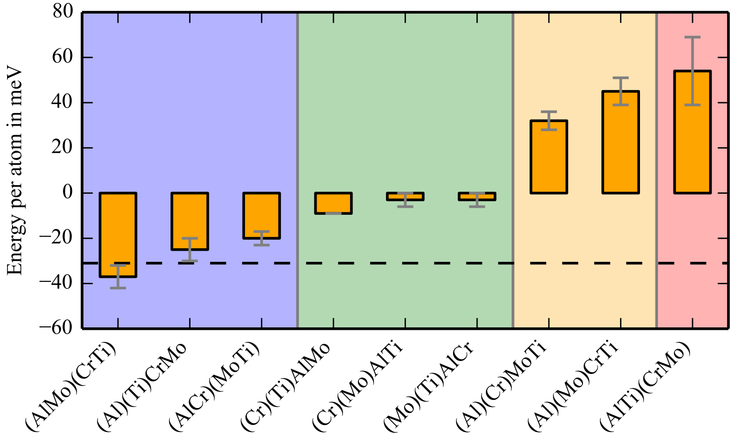

Figure 3.2: Excess ordering energy of differently ordered lattice configurations of AlCrMoTi. Colors are due to a classification of the free energy values into four groups. The broken line indicates the excess ordering energy in MoNbTaW calculated by Koermann and Sluiter[40].

The standard deviation of the free energies from different SQS representing the (AlTi)(CrMo) ordered lattice is 15meV per atom. This standard deviation is high compared to standard deviations of 0 - 6 meV per atom of the other B2-type lattice structures. The high standard deviation of (AlTi)(CrMo) denotes a strong dependency on the distinct elemental spatial distribution. Hence, a larger SQS would be necessary to improve the accuracy of the free energy calculation.

Since E_0 of the disordered lattice has been used as reference energy, a negative $E_0^{\alpha'}$ denotes an energetically favorable lattice structure, and a positive $E_0^{\alpha'}$ an energetically unfavorable. A detailed analysis of the free energy hierarchy indicates that the free energy depends on the Al-Al and Al-Ti bonds-shares. Hence, this work formulates the hypothesis that Aluminium plays a crucial role in the free energy hierarchy of differently chemically ordered lattice configurations in AlCrMoTi and, consequently, in the phase formation behavior of this alloy. Section 3.1.1 further analyses the stated hypothesis.

As a next step, this study compares the ground state energy results corresponding to different lattice configurations of AlCrMoTi to ground state energy results corresponding to different lattice configurations of HfNbTiZr.

Figure 3.3 shows the resulting $E_0^{\alpha'}$ of all possible elemental manifestations of (A)(B)CD and (AB)(CD) ordered lattices of HfNbTiZr. The results show funda-

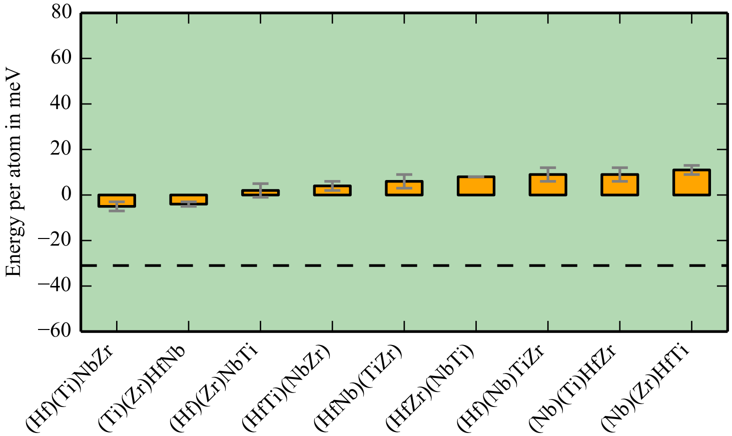

Figure 3.3: Ground state energies of disordered and differently ordered lattice configurations of HfNbTiZr. The broken line indicates the excess ordering energy in MoNbTaW calculated by [40].

mental differences between both alloy systems. While the ground state energy of AlCrMoTi highly depends on the distinct lattice configuration, the ground state energy of HfNbTiZr is nearly independent of the distinct lattice configuration. In AlCrMoTi, the lowest and highest observed E_0 differ by $91\mathrm{meV}$ per atom, while in HfNbTiZr, the lowest and highest E_0 differ only by $16\mathrm{meV}$ per atom.

DFT-calculations revealed an energy difference of -$31\mathrm{meV}$ per atom between the disordered phase and the (MoW)-ordered phase of the BCC HEA MoNbTaW[40]. Based on this finding, they predict a disorder-order phase transition at $T >$RT. The excess order energy of MoNbTaW is indicated in Figures 3.2 and 3.3. Comparing the different $E_0^{\alpha'}$ of AlCrMoTi and HfNbTiZr shows that the excess ordering energy in MoNbTaW is comparable to the lower ones in AlCrMoTi.

Figure 3.3 shows that in HfNbTiZr, all $E_0^{\alpha'}$ appear much higher than the excess order energy in MoNbTaW. The large $E_0^{\alpha'}$-values of AlCrMoTi and the low $E_0^{\alpha'}$-values of HfNbTiZr suggest that AlCrMoTi has a B2-type ordered lattice configuration at RT, while HfNbTiZr is disordered.

One must involve the systems' entropy for more detailed predictions corresponding to the disorder-order transition temperature. Hence, within Sections 3.2.1 and 3.2.3, a free energy model is performed, which involves the ideal configuration entropy. The model is applied to predict the temperature-dependent phase formation behavior of AlCrMoTi and HfNbTiZr.

The results are compared to experiments investigating the appearance of ordered phases in these alloys.

3.1.1 The role of Aluminium in the free energies of B2-type ordered states in AlCrMoTi

This section analyzes the influence of different Al bond concentrations on the free energies E_0^{α} of differently chemically ordered lattice configurations in AlCrMoTi. The free energy of disordered AlCrMoTi E_0^{dis} is used as off set energy ($E_0^{\alpha} \to E_0^{\alpha'} = E_0^{\alpha} - E_0^{\text{dis}}$). The analysis assumes that the different $E_0^{\alpha'}$ of differently chemically ordered and disordered AlCrMoTi result from different shares of energetically favorable and unfavorable direct neighbor bonds. This assumption is similar to the broken bond model, which connects the energy of an anti-phase boundary with the redistribution of direct neighbor bonds along the fault plane[12]. The matrices p_{ij}^{α} describe the different (ideal) bond shares of chemical disordered and (A)(B)CD- and (AB)CD-ordered (equimolar) four-component HEA. The matrices p_{ij}^{α} depend on the lattice configuration of phase α. For instance, $p_{ij}^{\text{(A)(B)CD}}$ describes the share of ij-bonds in a (A)(B)CD B2-type ordered four-component HEA. Figure 3.4 shows the matrices for the lattice configurations considered in this work. The matrices p_{ij}^{α} show that introducing or changing the chemical order leads to redistributing the bond shares. In order to find out which chemical bonds are favorable or unfavorable in AlCrMoTi, the disordered and ordered lattice configurations have been qualitatively classified by their $E_0^{\alpha'}$ into four different groups (see Figure 3.2).

Now considering the three lattice configurations with the lowest $E_0^{\alpha'}$ (blue group in Figure 3.2) leads to the insight that these structures are the three structures with the largest shares of Al-Ti bonds (0.25%), while the structure with the highest $E_0^{\alpha'}$ (red group in Figures 3.2) is the one with no Al-Ti bonds at all. Consequently, our data indicate that the Al-Ti bond content influences $E_0^{\alpha'}$. However, it remains to clarify the difference between the group of configurations with $E_0^{\alpha'}$ close to zero and the group of configurations with higher $E_0^{\alpha'}$ (orange group in Figure 3.2) since the Al-Ti bond content is equal in both groups (12.5%).

In the group with higher $E_0^{\alpha'}$, Al is distributed only on one superlattice, which leads to an elimination of Al-Al bonds, while the share of Al-Cr bonds in (Al)(Cr)MoTi or the share of Al-Mo bonds in (Al)(Mo)CrTi is increased.

Hence, Al-Al bonds are energetically more favorable than Al-X bonds, with

$$p^{\text{A2}} = \begin{pmatrix} 0.065 & 0.125 & 0.125 & 0.125 \\ 0.125 & 0.065 & 0.125 & 0.125 \\ 0.125 & 0.125 & 0.065 & 0.125 \\ 0.125 & 0.125 & 0.125 & 0.065 \end{pmatrix} \tag{3.4}$$

$$p^{\text{(A)(B)CD}} = \begin{pmatrix} 0 & 0.25 & 0.125 & 0.125 \\ 0.25 & 0 & 0.125 & 0.125 \\ 0.125 & 0.125 & 0.065 & 0.125 \\ 0.125 & 0.125 & 0.125 & 0.065 \end{pmatrix} \tag{3.5}$$

$$p^{\text{(AB)(CD)}} = \begin{pmatrix} 0 & 0 & 0.25 & 0.25 \\ 0 & 0 & 0.25 & 0.25 \\ 0.25 & 0.25 & 0 & 0 \\ 0.25 & 0.25 & 0 & 0 \end{pmatrix}. \tag{3.6}$$

Figure 3.4: Matrices p_{ij}^{α} describing the different (ideal) bond shares of chemical disordered and (A)(B)CD- and (AB)CD-ordered (equimolar) four-component HEA.

X=Cr,Mo. The observation that configurations with energies close to zero have the same sum of Al-Ti and Al-Al bond shares as the disordered lattice further supports the hypothesis that Al-Al and Al-Ti bonds are energetically more favorable than Al-X bonds.

Together, our data suggest that $E_0^{\alpha'}$ of different lattice configurations of AlCrMoTi strongly depend on the sum of Al-Ti and Al-Al bond shares. Figure 3.5 further supports the view of energetically favorable Al-Al and Al-Ti bonds in AlCrMoTi. The graph connects $E_0^{\alpha'}$ with the sum of Al-Ti and Al-Al bond shares of the corresponding lattice configuration. It shows a linear correlation (with correlation coefficient q=-0.93) between the free energy and the sum of Al-Al and Al-Ti bond shares. Note that the presented model cannot explain the energy differences between lattice configurations with the same Al-Al and Al-Ti shares and would require analyzing bonds beyond nearest neighbors. Including different bond-types increases complexity. However, Figure 3.5 shows that energy differences between lattice configurations, which share the same Al-Al and Al-Ti bond concentrations,

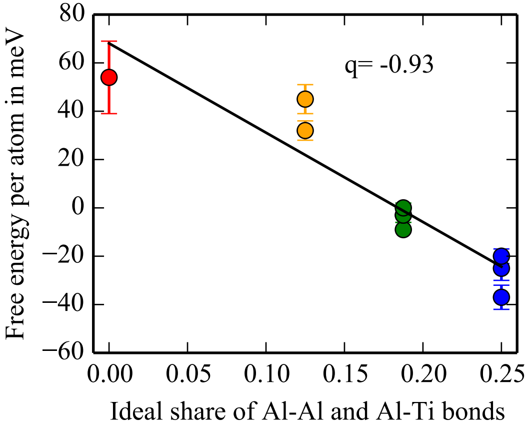

Figure 3.5: Ideal share of Al-Al and Al-Ti bonds in AlCrMoTi. Colors of dots belong to the classification of free energy values used in Figure 3.2.

are minor compared to energy differences between lattice configurations, which have different Al-Al and Al-Ti bond concentrations. Consequently, this study neglects bonds, which include other elements such as Al and Ti, and bonds beyond nearest neighbors.

The model presented in this section can connect $E_0^{\alpha'}$ with the share of specific bonds in phase α in the particular case of AlCrMoTi because one can classify $E_0^{\alpha'}$ into four groups, which belong to different shares of Al-Al and Al-Ti bond shares. By contrast, the free energies of disordered and differently ordered HfNbTiZr (see Figure 3.3) are much closer than those of AlCrMoTi. Consequently, one cannot classify the free energies of HfNbTiZr into different groups, which indicates that there is no specific bond type with an energy advantage high enough to be the dominating contribution to the free energy. The lack of energetically favorable bonds in HfNbTiZr may explain a stable disordered phase in HfNbTiZr at low temperatures.

The following section discusses the implications of the emerging phase formation behavior and the effect on the free energy of AlCrMoTi and HfNbTiZr.

3.2 Ordering transitions in BCC AlCrMoTi and HfNbTiZr

This section uses the previously presented excess ordering energies $E_0^{\alpha'}$ to predict order-disorder transitions in AlCrMoTi and HfNbTiZr. Considering only configuration entropy contributions, the appearance of ordered phases in HEA can be attributed to a competition of enthalpy and an entropy contribution in the free energy $F^\alpha = E_0^\alpha - TS^{\text{conf}}$. The system strives to minimize F. Consequently, at low temperatures, E_0^α is the dominant contribution. E_0^α depends on particle interactions, which the introduction of chemical ordering can reduce.
With increasing temperature, the ideal configuration entropy S^{conf} becomes the dominant contribution, implicating a disorder as high as possible[65]. S^{conf} can be calculated by $S^{\text{conf}} = -k_B \sum_i^N p_i \ln(p_i)$ with the microstate probability p_i, the number of different elements N and the Boltzmann constant k_B.
Tabular 3.1 summarises S^{conf} for the disordered and differently ordered lattice configurations considered in this work. At a temperature at which the free energies of two differently ordered phases (α, β) are equal, the system undergoes a phase transformation between two differently ordered lattice structures. The corresponding transition or critical temperature is calculated by

	S^{conf}
disordered	$k_B \ln 4$
(A)(B)CD	$\frac{k_B}{2} \ln 8$
(AB)(CD)	$k_B \ln 2$

Table 3.1: Ideal configuration entropy for four component equiatomic HEA for disordered and superlattice ordered state.

$$T_c = \frac{E_0^\alpha - E_0^\beta}{S_\beta^{\text{conf}} - S_\alpha^{\text{conf}}}. \tag{3.7}$$

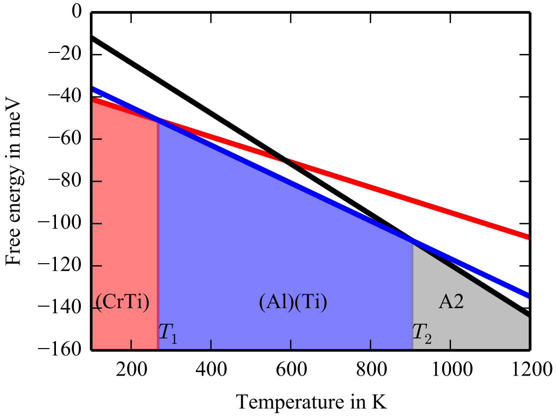

Figure 3.6: Free energies of disordered (black), (Al)(Ti)CrMo-ordered (blue) and (AlMo)(CrTi)-ordered (red) AlCrMoTi. $T_1 = 268\text{K}$ and $T_2 = 904\text{K}$ denote the critical temperatures.

3.2.1 Order-disorder transitions in AlCrMoTi

This section uses the presented free energy model to predict the order-disorder phase formation behavior in AlCrMoTi. Figure 3.6 describes the predicted phase formation behavior of AlCrMoTi based on the electronic ground state energy results and the derived $E_0^{\alpha'}$ from Section 3.1. It shows three free energies, with two of them representing the free energy F^{α} of the energetically most favorable chemical ordered lattice configurations $F^{(\text{CrTi})}$ (red) and $F^{(\text{Al})(\text{Ti})}$ (blue). The third one represents the free energy of the disordered lattice F^{dis} (black).

The data reveal that the (AMo)(CrTi)-ordered lattice configuration has the lowest free energy for low temperatures ($T < T_1 = 268\text{K}$), while the (Al)(Ti)CrMo-ordered lattice structure has the lowest free energy for intermediate temperatures ($T_1 = 268\text{K} < T < T_2 = 904\text{K}$).

For high temperatures ($T > T_2 = 904\ \text{K}$), the disordered lattice structure is energetically most favorable. Hence, the theoretical free energy approach predicts two phase transformations at $T_1^{\text{th}} = 268\text{K}$ and $T_2^{\text{th}} = 904\text{K}$.

Chen et al. found superlattice spots corresponding to a B2-type ordered crystal structure by TEM-selected area diffraction (TEM-SAD) investigations at room temperature[9]. They further performed Differential Scanning Calorimetry (DSC) in order to determine the derivative of the enthalpy with respect to temperature $\frac{dH}{dT}$. They found a λ-shaped peak at $T_2^{\text{exp}} = 1263\text{K}$, which indicates, according to Chen et al., a second-order phase transformation corresponding to a transformation from a B2-type ordered to a disordered lattice structure.

The appearance of a phase with a B2-type ordered lattice and an order-disorder phase transition at high temperatures is consistent with the theoretical free energy approach results.

However, the experimentally measured T_2 is higher than this work's theoretically determined transition temperature. One could attribute the inconsistency between the theoretically predicted and experimentally measured T_2 to the free energy approach and the fact that it neglects contributions to the free energy from lattice vibrations and electronic excitation.

However, the DFT calculations revealed that the predicted ordering temperature in MoNbTaW changes only by 9K if electronic and vibration contributions are involved[40], which indicates that vibrational contributions can be neglected for order-disorder transition temperatures in BCC HEA.

Another aspect that could rationalize the discrepancy between theoretical and experimental T_2 is that the theoretical approach at all temperatures anticipates ideal mixing. The assumption of ideal mixing could lead to an overestimation of the configuration entropy of the disordered lattice since this approach does not capture short-range ordering.

Further, the λ-shaped peak from the DSC measurements indicates a phase transformation of second order (within Ehrenfest definition). At the same time, the free energy approach can only describe a first-order phase transformation. In the case of ordering transformations in HEA, a continuous transition between disorder and order could be a reasonable approach to describe the ordering process. The approach of continuous ordering is based on the assumption that there is no sharp transition from disorder to order at $T = T_2$. Moreover, there already exist (Al)(Ti)-ordered clusters within the chemically disordered crystal lattice at temperatures above T_2. The share of ordered clusters decreases with increasing temperatures $T >> T_2$. With decreasing temperatures approaching T_2, the share ordered clusters increases. The consequence is that there is no sharp transition of the S^{conf} at T_2, and one would have to describe S^{conf} as a continuous function of T.

However, the prediction of the detailed phase formation behavior of BCC HEA is outside the scope of this work. This work aims to rationalize the existence of disorder-order phase transitions and to determine the participating elements. These findings reveal further insights into the connection between the different chemistry and the macroscopic mechanical properties of BCC HEA.

The idea that there is a connection between the distinct lattice configuration of AlCrMoTi and its mechanical properties is consistent with experiments[10], which showed that reducing the Al-share leads to the disappearance of the ordered phase and improves ductility. The strong influence of the Al-share is consistent with the findings of this work, where Al is participating in the predicted ordered phases. Based on these findings, the following section investigates the role of Al in the phase formation behavior in more detail.

3.2.2 Influence of Al-reduction on the order-disorder critical temperature in AlCrMoTi

The results presented in Section 3.2.1 combined with the experimental findings of Chen et al.[9] suggest that AlCrMoTi is at room temperature B2-type ordered with Al and Ti occupying the two different simple cubic superlattices. The findings of Section 3.1.1 combined with the experimental results of Laube et al.[10] suggest that Al plays a crucial role in the order-disorder phase formation in AlCrMoTi. Hence, the question arises if the reduction of Al can suppress the ordered phase. In order to address this question, a relationship between the Al share x and the order-disorder transition temperature

$$T_c(x) = \frac{\Delta E(x)}{\Delta S^{\text{conf}}(x)} \tag{3.8}$$

is derived. It assumes that the energy difference between the disordered and ordered lattice configuration $\Delta E(x)$ follows the linear relation in Section 3.1.1 (see Figure 3.5)

$$\Delta E(x) = m \cdot \Delta p(x), \tag{3.9}$$

with slope m and the difference between the ideal share of Al-Al plus Al-Ti bonds in the disordered and ordered lattice

$$\Delta p(x) = p^{\mathrm{A2}}(x) - p^{\mathrm{B2}}(x). \tag{3.10}$$

For the calculation of $p^{\mathrm{A2}}(x)$ and $p^{\mathrm{B2}}(x)$, the Al-share dependent site occupation probabilities have to be determined. Within a disordered lattice, all sites are equally occupied. Hence

$$p^{\mathrm{A2}}(x) = x^2 + \frac{2x}{3}(1-x) \tag{3.11}$$

models the Al-Al and Al-Ti ideal bond shares in the disordered lattice depending on the Al-share x.

For the partially B2-ordered lattice, the sites of the two simple cubic superlattices SL1 and SL2 are occupied differently. Tabular 3.2 summarises the elemental site occupation probabilities for a lattice, which is ordered in the following way: Al atoms occupy only one superlattice (SL1). On the other hand, Cr and Mo atoms occupy both superlattices evenly. The Ti atoms fill the remaining share. This ordering leads to a Ti-enriched superlattice (SL2) and a Ti-depleted superlattice (SL1). Based on this partially B2-type ordered distribution

$$p^{\mathrm{B2}}(x) = 2x\left[\frac{1}{3}(1-x) + x\right] \tag{3.12}$$

describes the ideal share of Al-Al and Al-Ti bonds. The Al-share dependent site occupation probabilities allow the calculation of the ideal configuration entropy difference $\Delta S^{\mathrm{conf}} = S^{\mathrm{conf}}_{\mathrm{A2}} - \frac{k_B}{2}\left(S^{\mathrm{SL1}}_{\mathrm{B2}} + S^{\mathrm{SL2}}_{\mathrm{B2}}\right)$ with

	SL1	SL2
Al	$2x$	0
Ti	$\frac{1}{3}(1-x)-x$	$\frac{1}{3}(1-x)+x$
Cr	$\frac{1}{3}(1-x)$	$\frac{1}{3}(1-x)$
Mo	$\frac{1}{3}(1-x)$	$\frac{1}{3}(1-x)$

Table 3.2: Elemental occupation probability of simple cubic superlattices SL1 and SL2 in Al$_x$CrMoTi.

$$\begin{aligned}
S_{\mathrm{A2}}^{\mathrm{conf}}(x) &= -k_B\left[(1-x)\ln\left(\frac{1}{3}(1-x)\right)+x\ln(x)\right]\\
S_{\mathrm{B2}}^{\mathrm{SL1}}(x) &= 2x\ln(2x)+\frac{2}{3}(1-x)\ln\left(\frac{1}{3}(1-x)\right)\\
&\quad+\frac{2}{3}(1-x)\ln\left(\frac{1}{3}(1-x)\right)\\
&\quad+\left(\frac{1}{3}-\frac{4x}{3}\right)\ln\left(\frac{1}{3}-\frac{4x}{3}\right)\\
S_{\mathrm{B2}}^{\mathrm{SL2}}(x) &= \frac{2}{3}(1-x)\ln\left(\frac{1}{3}(1-x)\right)\\
&\quad+\left(\frac{1}{3}+\frac{2x}{3}\right)\ln\left(\frac{1}{3}+\frac{2x}{3}\right).
\end{aligned}$$

Figure 3.7 displays the introduced model parameters depending on the Al content x of Al$_x$CrMoTi. It shows, that p^{B2} increases stronger with increasing Al-share x as p^{A2}. For decreasing Al-share p^{B2} and p^{A2} converge to zero. Consequently, $\Delta E(x)$ increases with increasing x. The A2 configuration entropy $S_{\mathrm{A2}}^{\mathrm{conf}}$ is monotonic increasing with increasing x, while $S_{\mathrm{B2}}^{\mathrm{conf}}$ has a maximum at $x \approx 0.08$. For decreasing x, both configuration entropy contributions approach the value of a disordered three-component alloy (≈ 1.1). Figure 3.8 depicts the predicted Al-share dependent T_c. The data reveal that $T_c(x)$ initially increases with decreasing x until a maximum value of $T_c = 962\mathrm{K}$ is reached at $x = 0.23$). If x is further reduced, T_c decreases monotonically. The graph further shows that a T_c

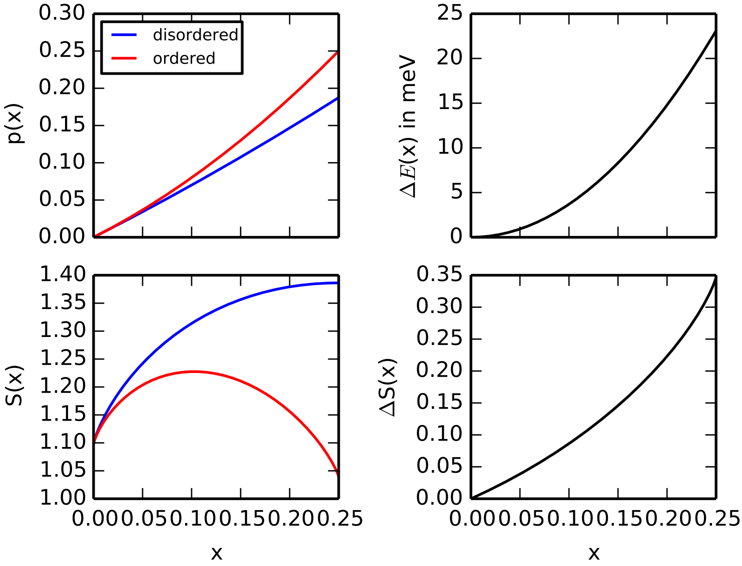

Figure 3.7: Upper left: Al-Al plus Al-Ti bond share of a disordered (blue) vs. ordered (red) lattice configuration. **Upper right:** Energy difference between disordered and ordered lattice. **Lower left:** Ideal configuration entropy depending on Al-share of disordered (blue) vs. ordered (red) lattice configuration. **Lower right:** difference between the configuration entropy of a disordered and ordered lattice depending on Al-share.

of 300K is reached for an Al-share slightly below 0.05.

The predictions of the presented model are now discussed in the context of experimental results[5,9,10]. The experimental studies investigate samples with varying Al-share ($x = 0.03, 0.05, 0.1, 0.15, 0.25$) by X-ray diffraction (XRD) and transmission electron microscopy (TEM) in order to detect reflections indicating an ordered lattice. The study used dynamic scanning calorimetry (DSC) to measure the first derivative of the enthalpy with respect to temperature.

The XRD measurements yielded Bragg peaks according to a disordered lattice in Al_xCrMoTi for x=0.03, 0.05, 0.15, 0.25. Indications of B2-type ordering could not be found for these Al concentrations. For x=0.1, superlattice peaks have been observed, which indicate the appearance of a B2-type ordered phase.

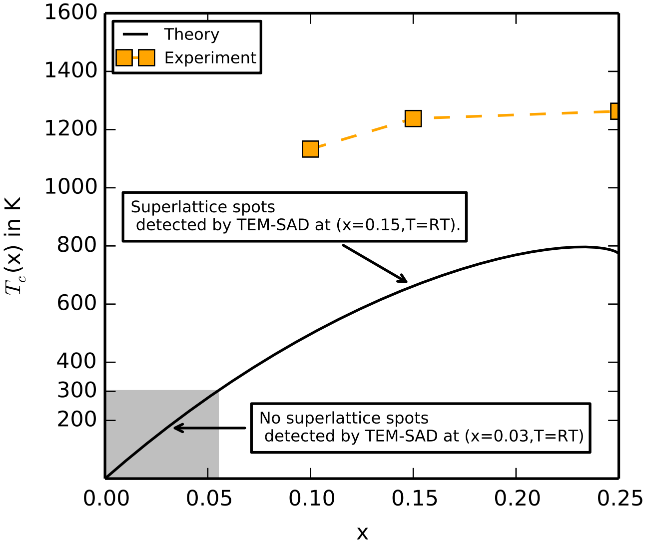

Figure 3.8: Black line: Predicted order-disorder transition temperature with respect to Al-share x in Al_xCrMoTi. **Orange squares:** Experimentally determined T_c from DSC measurements [9,10]

The site occupation might not differ sufficiently from a disordered structure, which leads to a vanishing Bragg intensity for the B2 superlattice peaks [9,10]. Using TEM-SAD, with its compared to XRD higher dynamic range on $\mathrm{Al}_{0.25}$CrMoTi, $\mathrm{Al}_{0.15}$CrMoTi, and $\mathrm{Al}_{0.03}$CrMoTi revealed superlattice peaks corresponding to a B2-type order for x=0.15, but no indications of B2 ordering for x=0.03 [9,10]. This result is consistent with the results from the model presented in this work since the predicted T_c for $x = 0.03$ is below RT, while the predicted T_c for $x = 0.15$ is 758K (see Figure 3.8).

However, the data from the DSC measurements indicate the appearance of A2-B2 phase transformation in the alloys with $x = 0.25, 0.15, 0.1$ with corresponding T_c of 1263K, 1238K and 1133K. Thus the measured transition temperatures are above the theoretically predicted T_c-curve.

Section 3.2.1 already discussed possible explanations for the theoretically underestimated transition temperatures from the theoretical approach. Although the experimental transition temperatures are higher than the predicted transition temperatures, the experimentally measured course of $T_c(x)$ is qualitatively consistent with the model predictions. The experimental T_c decreases less between $x = 0.25$ and $x = 0.15$ as between $x = 0.15$ and $x = 0.1$.

3.2.3 Lack of ordering transitions in HfNbTiZr

This section uses the already presented electronic ground state energy results and the derived excess ordering energies $E_0^{\alpha'}$ within the free energy approach to discuss the existence of B2-type ordering in HfNbTiZr. To this date, experiments have not found any indications of long-range crystallographic ordering in HfNbTiZr or the related five-component HfNbTaTiZr. The lack of long-range crystallographic ordering in HfNbTiZr is in contrast to Al-Cr-Mo-Nb-Ti alloys, where strong experimental and theoretical indications have been found for the existence of B2-type ordering.

Comparing Figure 3.6 and Figure 3.9 can rationalize the different phase formation behavior of these two alloy families. It shows that the order-disorder phase transition with the highest T_c is predicted for AlCrMoTi at $T_2 = 904\text{K}$. In contrast, HfNbTiZr has only one order-disorder transition with a very low T_c of 167K is predicted. The very low T_c is attributed to the small E_0^{α}-differences between ordered and disordered phases in HfNbTiZr.

The question remains if the slight energetic advantage of two ordered structures ((Hf)(Ti)NbZr and (Ti)(Zr)HfNb) compared to the disordered state can cause short-range ordering. The clarification of this question is outside the scope of this work.

The predicted difference between the disordered HfNbTiZr and chemically ordered AlCrMoTi could explain the different mechanical properties of HfNbTiZr and AlCrMoTi. This work will later investigate the influence of crystallographic ordering on fundamental material properties.

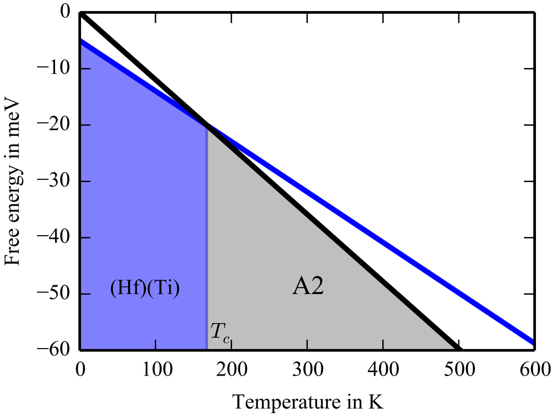

Figure 3.9: Free energies of disordered (black) and (Hf)(Ti)-ordered (blue) HfNbTiZr.

3.3 Conclusions

DFT calculations have been employed to determine ground state energies of disordered and different B2-type ordered lattice configurations of AlCrMoTi and HfNbTiZr.

- Three B2-type ordered lattice configurations in AlCrMoTi are predicted to have lower free energies below the free energy of the disordered lattice.
- Minimising the free energy predicts for AlCrMoTi a transition at $T_1 = 268\text{K}$ from an (AlMo)(CrTi)- to an (Al)(Ti)CrMo-ordered lattice and a second transition at $T_2 = 904\text{K}$ from an (Al)(Ti)CrMo-ordered to a disordered AlCrMoTi lattice.
- The ground state energy of an AlCrMoTi lattice configuration depends on its Al-Ti and Al-Al bond share. This finding predicts a relation between the Al-concentration c_{Al} and the order-disorder transition temperature.

- The minor differences between the ground state energies of chemically disordered and differently ordered lattice structures in HfNbTiZr rationalize the experimentally observed lack of crystallographic ordering in this alloy.

4 Equilibrium structure and material properties

After discussing ordering in the two HEA alloy systems, this chapter focuses on the quantitative prediction of their detailed crystal structure and properties to identify the most efficient simulation methodology to predict these. The lattice constant (Section 4.1) is needed to predict the Burgers vectors. The Burgers vectors, elastic constants (Section 4.2), lattice distortions (Section 4.3), and generalized stacking fault energies (GSFE) (Section 4.4) serve as input parameters for dislocation mobility models. In Chapter 5, this work used dislocation mobility models to discuss the different plastic behaviors of different BCC HEA since dislocations are assumed to control plastic deformation in HEA.

4.1 Mean equilibrium lattice constant

This section presents mean lattice constants a_0 of BCC HEA from DFT calculations and the rule of mixtures (ROM). A comparison to experimental values allows validation of both approaches. The DFT approach determines a_0 by relaxing supercells representing the alloys. The relaxation occurs with respect to the atomic positions, cell shape, and volume. After the successful relaxation process, a_0 is determined through the equilibrium volume.

Another possibility is to calculate the energy of a supercell with respect to its cell volume. Here the relaxation is due to atomic positions and cell shape only. The determination of a_0 is performed by fitting the equation of state (EOS) on the energy-volume relation. Both methods are explained more in detail in Section 2.3.

Note that in the case of random alloys, the interatomic distances are approximately normal-distributed (see later in Section 4.3 for a detailed analysis), and the presented a_0 values denote the mean lattice constants. Besides the DFT approach, a rule of mixtures approach has been used, which calculates a_0 of a N component HEA by

$$a_0^{\mathrm{ROM}} = \sum_{i=1}^{N} c_i a_0^i, \tag{4.1}$$

with the element concentrations c_i. The values of the lattice constants of pure BCC metals a_0^i correspond to a BCC configuration. Since not all elements crystallize in BCC configuration, theoretical DFT values (listed in Table A.1) have been used instead of experimental values. Table 4.1 shows the calculated a_0 for a series of BCC HEA, and Figure 4.1 illustrates the deviations of a_0^{DFT} and a_0^{ROM} from experimental values a_0^{exp}.

The data show that for the most HEA, the a_0^{DFT} and a_0^{ROM} reproduce the experimentally measured values with deviations $\leq \pm 1\%$. The largest deviation between theoretically calculated and experimentally measured a_0 appears in HfNbTiZr. Here a_0^{DFT} and a_0^{ROM} underestimate a_0^{exp} by 2.4% and 2.8%.

The significant deviation is remarkable since the ROM and DFT approach can

HEA	a_0^{DFT} [Å]	a_0^{exp} [Å]	a_0^{ROM} [Å]	$\frac{\Delta a_0^{\mathrm{DFT}}}{a_0^{\mathrm{exp}}}$	$\frac{\Delta a_0^{\mathrm{ROM}}}{a_0^{\mathrm{exp}}}$
AlCrMoTi	3.090 ±0.001	3.101 ± 0.018[5]	3.128	-0.4%	0.9%
(Al)(Ti)CrMo	3.089 ±0.001	-	-	-	-
(AlMo)(CrTi)	3.089 ±0.001	-	-	-	-
AlCrMoNbTi	3.146	3.149 ± 0.021[5]	3.167	0.0%	0.6%
AlCrMoTaTi	3.148	3.152[9]	3.167	-0.1%	0.5%
AlCrMoTiV	3.072	-	3.101	-	-
AlCrMoTiW	3.109	3.093/3.102[66]	3.140	0.2%	1.2%
AlMoNbTaTi	3.244	-	3.257	-	-
AlMoNbTaV	3.199	-	3.205	-	-
HfNbTiZr	3.435 ± 0.001	3.519[8]	3.414	-2.4%	-3.0%
HfNbTaTiZr	3.412	3.404[4]	3.396	0.2%	-0.2%
HfMoNbTiZr	3.372	3.371[67]	3.365	0.0%	-0.2%
HfNbTiVZr	3.358	3.385[68]	3.330	-0.8%	-1.6%
AlFeNbTiV	3.092	-	3.125	-	-
CrMoHfTiZr	3.280	-	3.275	-	-
MoNbTaVW	3.198	3.183[69]	3.198	0.5%	0.5%
MoNbTaW	3.240	3.213[69]	3.249	0.8%	1.1%
MoNbTi	3.232	-	3.247	-	-

Table 4.1: Lattice constants of different BCC HEA predicted by DFT calculations and the rule of mixture. Values are compared to experiments.

predict a_0 of chemically similar HfNbTaTiZr and HfMoNbTiZr much more accurately. This observation indicates that the large deviation is connected to the large fraction (75%) of elements with a hexagonal closed-packed (HCP) equilibrium lattice structure.

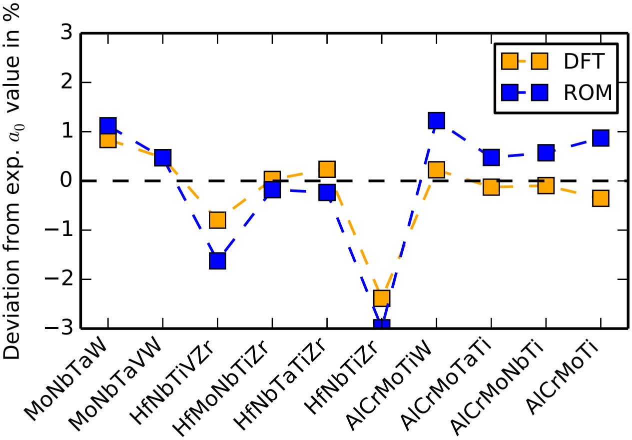

Figure 4.1: Comparison between lattice constants, which have been experimentally measured, calculated by DFT, and calculated by using the ROM. The DFT values correspond to disordered SQS.

Additionally, Figure 4.1 shows that the a_0^{DFT} and a_0^{ROM} follow the same trend for a broad spectrum of BCC HEA. The DFT approach can predict experimental values more accurately. Although the data illustrate that the ROM tends to overestimate a_0 for BCC HEA based on AlCrMoTi, the ROM produces a_0, which aligns very well with a_0^{DFT} and a_0^{exp}. Thus, it allows determining a_0 of BCC HEA with minimal computational or experimental effort.

Further a_0^{ROM} can be used as an accurate start parameter for DFT calculations to relax the investigated structure in its energetic minimum, the starting point for further calculations of material quantities like stacking fault energies and elastic constants.

4.2 Elastic Constants

This work investigates the influence of the distinct chemical composition of a random alloy on its plastic deformation behavior. The chemical composition of a material determines its elastic properties. While the elastic tensor at first glance defines only the elastic deformation, a closer look reveals its crucial role in the plastic behavior of metals and alloys. The motion of dislocations carries crystal plasticity. Simultaneously, interactions of dislocations with other defects crucially influence the material strength.

Although continuum theory is a poor approximation of the discrete crystal structure, it accurately describes the distortion generated by a dislocation as long as the dislocation core region is excluded. Consequently, the continuum approximation enables the calculation of the elastic dislocation energy.

Here the elastic tensor, the Burgers vector, and the dislocation line direction are the necessary input parameters[12]. The dislocation line energy or the closely related line tension are necessary input quantities for several models describing crystal plasticity (see Section 5.1).

The Cottrell-Bilby formula, which this work uses in the context of solid solution strengthening, was derived using continuum theory to describe the interaction of dislocations with point defects. The shear modulus μ and the Poisson ratio ν are necessary input quantities[13]. Based on the Cottrell-Bilby formula, recent models have been developed to describe the strength of random alloys and HEA[48,36]. Besides these mechanistically motivated theories, phenomenological laws connect certain materials' ductility with their elastic properties. The Pugh relation states that materials are ductile if the ratio between the shear- and the bulk modulus (μ/B) is small[70] and Pettifor connected ductility to a positive Cauchy pressure $C_{12} - C_{44}$[71]. The presented examples show that the knowledge of the elastic tensor is crucial for investigating deformation mechanisms in metals and alloys.

However, especially for HEA with their huge composition space, the experimental determination of C_{ij} reaches the limit of practicability. Hence, methods are needed to determine elastic constants quickly and with little effort. The results in Appendix A.2 show that using the SSOS approach instead of the SQS approach enables a comparable fast calculation of elastic constants by DFT calculations. Furthermore, the use of Vegard's law enables the calculation of HEA elastic constants with minimal computational effort. This section presents elastic constant results from both approaches. It compares elastic constants from DFT and Vegard's law and experiments to analyze the theoretical approaches' predictive power. Finally, the elastic constant data for a series of different BCC HEA are used in order to discover trends that connect the specific chemical composition of a HEA with its elastic tensor. Finally, this work uses the trend as a guideline for material design.

4.2.1 Elastic constants of a series of BCC HEA

This section presents elastic constant results of a series of BCC HEA. DFT calculations have generated the results using the methods described in Section 2.4. Table 4.2 lists the DFT-calculated values of a series of BCC HEA. Besides the DFT approach, a rule of mixture approach has been used in order to calculate elastic constants by

$$C_{ij} = \sum_{k=1}^{N} c_k C_{ij}^{k}, \tag{4.2}$$

with the concentration c_k and the elastic constants C_{ij}^{k} of element k . The elastic constants of the pure elements are DFT values and have been extracted from Materials Project[72]. DFT values have the advantage that values can be used, which correspond to a BCC configuration, even if the material prefers another crystal structure.

Figure 4.2 illustrates the relative deviation between values from DFT and ROM. It shows that most deviations are less than 20%. On the other hand, the ROM approach reveals larger values for C_{11} compared to the DFT approach. This trend seems to be independent of the chemical composition. For HfTiZr-containing alloys, the ROM predicts C_{12} values $\approx 20\%$ higher than the DFT values. The differences between C_{12} values from DFT and ROM are relatively small for the remaining alloys. The most considerable relative deviations appear for C_{44}. For

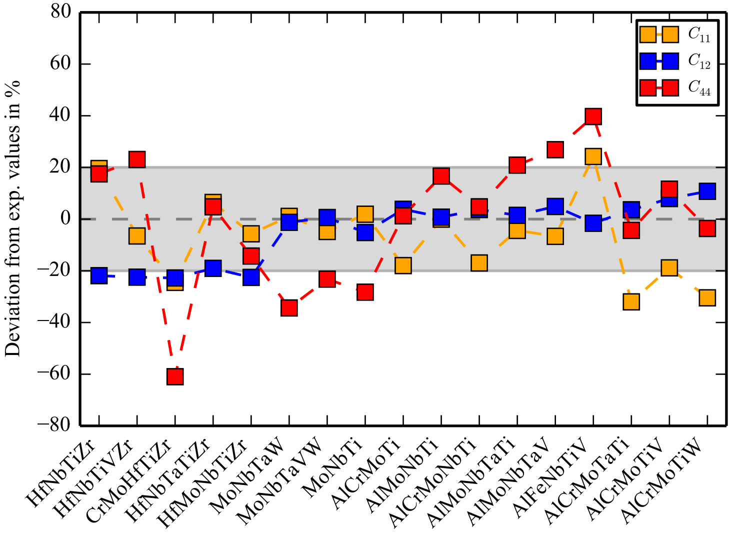

Figure 4.2: Relative deviation of elastic constant values from DFT and ROM. The DFT values correspond to disordered SQS.

C_{44}, no systematic tendencies of the deviations are visible in the present data. Here the question arises whether the DFT or the ROM approach reveals elastic constants which closely describe the actual material's elastic properties. Since anisotropic elastic constants from experiments are unavailable for BCC HEA, both approaches are validated against experimental isotropic shear modulus data μ^{exp}. Figure 4.3 shows that the DFT and ROM approaches predict larger shear modulus values μ^{DFT} and μ^{ROM} for AlMoTi-containing alloys compared to the value of HfNbTaTiZr. The differences in the predicted shear modulus values of AlMoNbTi, AlCrMoTi, and AlCrMoNbTi are comparatively small. Both trends are consistent with the experimental data.

Due to the large C_{44} value of Cr ($\approx 100\text{GPa}$), the ROM predicts an increasing shear modulus with increasing c_{Cr}. The data from DFT show an increasing shear modulus with increasing c_{Cr} as well, but less pronounced. The experimental results do not follow this trend. Hence, both approaches show inconsistency with

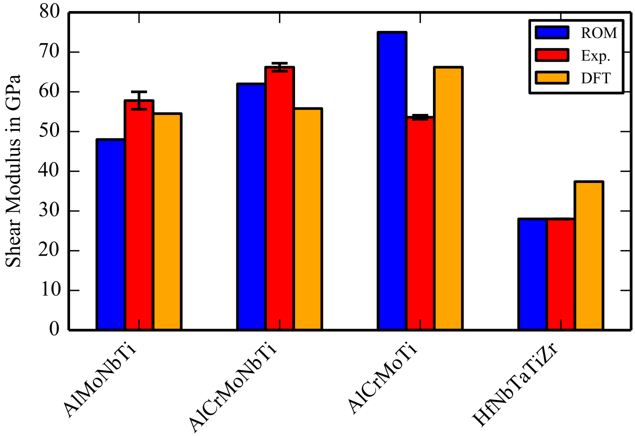

Figure 4.3: Comparison of shear modulus μ values of BCC HEA from DFT, ROM, and experiment. The DFT values correspond to disordered SQS.

the experimental data, where AlCrMoNbTi has the highest shear modulus value among the four compared alloys.

The differences between μ^{DFT} and μ^{exp} vary between 5% and 34% and the differences between μ^{ROM} and μ^{exp} between 0% and 40%. The experimental values have been determined by ultrasound measurement [5,6]. For AlCrMoTi, AlMoNbTi and AlCrMoNbTi the relative errors vary between 1% and 5%. Hence, the deviations might be attributed to the limitations of the used theoretical approaches. The ROM is based on the assumption that an alloy's elastic properties depend linearly on the properties of its constituents. In the case of elastic constants, which describe the response of a quantum mechanical many-body system (i.e., the crystal) to an external modification (i.e., the distortion), this linear approach is a fairly rough approximation. However, it is all the more surprising that within this study, the performance of the ROM approach is comparable to that of the DFT approach, which is based on an ab initio theory developed for the description of such quantum mechanical many-body systems. Of course, the DFT approach also suffers from limitations arising from several approximations (see Section 2.1). Nevertheless, the study shows that despite their limitations, both theoretical approaches can predict μ of BCC HEA within 0-40% relative error.

A direct consequence of the ROM's validity for BCC HEA elastic properties is that only average elastic properties are expected for these materials. Hence, equiatomic BCC HEA, which have extraordinarily high or low elastic constants compared to pure BCC metals, should be unlikely. One could consider the inability to produce equiatomic HEA with extraordinary elastic properties as a substantial drawback of the HEA approach corresponding to the goal of exploring materials with extraordinary mechanical properties. However, this study suggests a way out of this material's design pitfall. HfNbTiZr, for instance, has elastic constants, which are relatively small compared to the ones of most pure BCC metals. The fact that the averaging over its components does not lead to elastic properties of an average BCC material is based on the fact that it consists of 75% of non-BCC elements. Therefore, using large shares of non-BCC elements to reveal BCC alloys with (for BCC metals) extraordinary elastic properties could be practicable.

The BCC preference effect shows how this design approach could be realized[73]. Solid solutions consisting of several elements prefer to crystallize in BCC configuration if the atomic size differences of the single elements are large. The BCC preference effect holds even for large shares of non-BCC elements.

Elastic constants may play an essential role in mechanical properties, but elastic constants are not the only decisive factor. Hence, it should be investigated if there are other important material properties for which the ROM is not valid.

Another aspect of HEA is the possibility of chemical ordering. The following section investigates the influence of chemical ordering on elastic constants.

4.2.2 Influence of B2 - type chemical ordering on the elastic constants of AlCrMoTi

This section investigates the influence of crystallographic ordering on the elastic constants in AlCrMoTi. DFT calculations determined the elastic constants of AlCrMoTi and (Al)(Ti)CrMo for the investigation. Four different relaxed SQS with $N_{\text{atoms}} = 128$ have been used to determine nine strain-energy relations. Polynomial fitting and averaging over the cubic equivalent indices yielded the three cubic

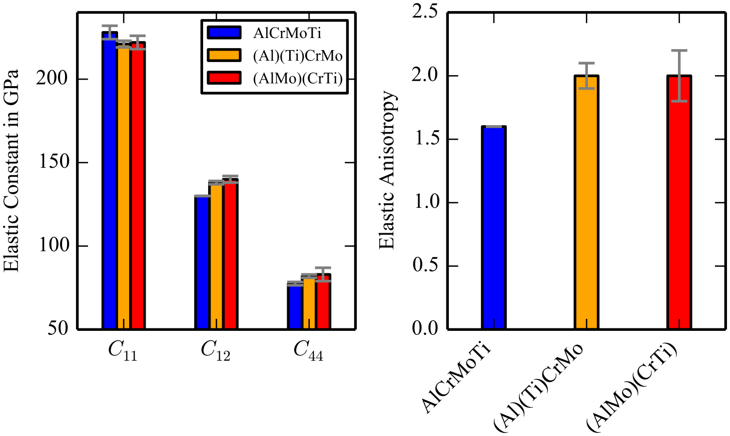

Figure 4.4: Cubic elastic constants of chemical disordered AlCrMoTi (blue) and chemically ordered (Al)(Ti)CrMo (orange) and (AlMo)(CrTi) (red) calculated by DFT-calculations. Error bars correspond to the standard deviation resulting from different SQS.

elastic constants (C_{11}, C_{12}, C_{44}) for each SQS.

The calculation procedure was different in the case of (AlMo)(CrTi). Here a set of five different $N_{\text{atoms}} = 64$ SQS have been relaxed due to cell volume and atomic positions. Then only three instead of nine strain-energy relations have been determined. Consequently, the fact that the SQS of a HEA generally breaks the cubic symmetry has been neglected. It is assumed that the different calculation methods do not affect the results. This assumption is based on the detailed analysis in Appendix A.1.

Figure 4.4 compares the resulting elastic constants of the different lattice configurations. It shows that C_{11} decreases from disorder to order, while C_{12} and C_{44} increase from disorder to order. This leads to an increased elastic anisotropy factor $A = \frac{2C_{44}}{(C_{11}-C_{44})}$ from disorder to order.

The increased anisotropy of ordered structures compared to the disordered lattice can be attributed to the change of specific bond shares from order to disorder. In the disordered alloy, the probability of finding an XY- or XX-bond is independent of the element X or Y. The probability of finding an XY- and XX-bond in the ordered alloy depends on the specific element combination of X and Y. In the case of AlCrMoTi, this leads to an increased directional dependent elastic tensor.

4.2.3 Conclusions

This section showed elastic constant results of several equiatomic BCC HEA. The results have been generated directly by DFT calculations or by using the rule of mixtures with DFT-determined elastic constants of pure metals.

- In most cases, results from the rule of mixture and DFT results are consistent within 22 % margins. However, deviations up to 60% have been observed as well. The validity of Vegard's law implicates that equiatomic BCC HEA with mainly BCC elements have elastic properties, which are average among BCC materials. However, the BCC preference effect[73] enables the development of equiatomic BCC HEA with extraordinary elastic properties by using large amounts of non-BCC elements. The comparable low elastic constants found in HfNbTiZr and HfNbTaTiZr support this hypothesis.
- The differences between μ^{DFT} and μ^{exp} vary between 5% and 34% and the differences between μ^{ROM} and μ^{exp} between 0% and 40%.
- The introduction of long-range chemical ordering increases the elastic anisotropy of AlCrMoTi.

HEA	C_{11} [GPa]	C_{12} [GPa]	C_{44} [GPa]
HfNbTiZr	143	96	40
HfNbTiVZr*	138	98	39
CrHfMoTiZr*	192	101	41
HfNbTaTiZr	155	105	42
HfMoNbTiZr*	176	102	42
MoNbTaW	374	163	64
MoNbTaVW	335	160	56
MoNbTi	263	135	46
AlCrMoTi	228	131	78
AlMoNbTi	203	129	66
AlCrMoNbTi	224	135	63
AlMoNbTaTi*	206	136	67
AlMoNbTaV*	240	143	67
AlFeNbTiV*	227	125	68
AlCrMoTaTi*	203	138	69
AlCrMoTiV*	228	138	69
AlCrMoTiW*	243	158	83

Table 4.2: Cubic elastic constants calculated for different BCC HEA with DFT calculations. The * marks alloys whose values were determined using the SSOS-approach. The SQS-approach was used to determine the elastic constants of the other alloys.

4.3 Interatomic distance and atomic volume distributions

This section investigates different quantities from interatomic distance and atomic volume distributions as descriptors of lattice distortions in BCC HEA. Lattice distortions are particularly interesting since they are one of the signature properties of HEA. Quantities strongly connected to lattice distortions, e.g., the atomic misfit volume, serve as input parameters for solid solution strengthening (SSS) theories. In SSS theories, interactions between dislocations and chemical fluctuations reduce dislocation mobility and increase the material's strength[48,35,36].
In the SSS model[48], the strength of a random alloy can be increased by increasing the mean square misfit volume and shear modulus. This theory is based on the assumption of a minor contribution of the Peierls stress and is consequently more reasonable for the description of FCC random alloys. Nevertheless, the FCC solid solution strengthening model from[48] can rationalize a correlation between the misfit volume and strength in a series of BCC Al-Cr-Mo-Nb-Ti alloys[5]. This correlation can be attributed to a reduced edge dislocation mobility existing in at least some BCC HEA[34,33].
Within the MC-II[36] model specifically developed for BCC random alloys, edge dislocations interact with chemical fluctuations. The alloy strength scales with an atomic misfit parameter M_v, i.e., the average misfit volume due to the different elements within the crystal matrix[36]:

$$M_v = \sqrt{\sum_i^N c_i \left(\Delta \overline{V}_i^2 + \sigma^2_{\Delta V_i} \right)}, \tag{4.3}$$

The quantity $\Delta \overline{V}_i = \overline{V} - \overline{V}_i$ denotes the average misfit volume of solute i and $\sigma^2_{\Delta V_i}$ the corresponding standard deviation. One can transform M_v into the atomic size difference

$$\delta = \sqrt{\sum_i c_i \left(1 - \frac{r_i}{\overline{r}} \right)^2}, \tag{4.4}$$

with the mole fraction c_i of element i, the mean atomic radius $\overline{r}$ of the considered HEA and the elemental atomic radii r_i [5]. The transformation is based on a mean-field approach. The random crystal lattice can be described by an effective mean lattice parameter $\overline{a}_0$ and the variation around this value. Within this picture, the different atomic radii of the elements cause variations in the interatomic distances around the lattice parameter. This model neglects the influence of the specific chemical environment. The advantage of this model is that there exists experimental access to δ via X-ray diffraction (XRD).

XRD is used to determine the effective mean lattice parameter [5], which allows the calculation of $\overline{r}_i = \frac{\sqrt{3}}{4}\overline{a}_0$. However, XRD can not directly determine the single r_i element specific [5]. Therefore, r_i is commonly taken from the corresponding pure elements. However, this procedure ignores that some elements of the considered HEA have non-BCC configurations in their elemental state (e.g., Al, Ti). Hence, the bond length in BCC configuration differs from that in their preferred configuration (e.g., FCC, HCP) [48].

The study [5] approached this issue by solving the linear equation system connecting the element-specific atomic radii of pure elements with the (XRD) measured mean atomic radii of different BCC HEA:

$$\begin{pmatrix} 1 & 0 & 0 & 0 & 0 \\ 0 & 1 & 0 & 0 & 0 \\ 0 & 0 & 1 & 0 & 0 \\ c_{\mathrm{Cr},1} & c_{\mathrm{Mo},1} & c_{\mathrm{Nb},1} & c_{\mathrm{Al},1} & c_{\mathrm{Ti},1} \\ c_{\mathrm{Cr},2} & c_{\mathrm{Mo},2} & c_{\mathrm{Nb},2} & c_{\mathrm{Al},2} & c_{\mathrm{Ti},2} \\ c_{\mathrm{Cr},3} & c_{\mathrm{Mo},3} & c_{\mathrm{Nb},3} & c_{\mathrm{Al},3} & c_{\mathrm{Ti},3} \\ & & \vdots & & \end{pmatrix} \begin{pmatrix} r_{\mathrm{Cr}} \\ r_{\mathrm{Mo}} \\ r_{\mathrm{Nb}} \\ r_{\mathrm{Al}} \\ r_{\mathrm{Ti}} \end{pmatrix} = \begin{pmatrix} r_{\mathrm{Cr}} \\ r_{\mathrm{Mo}} \\ r_{\mathrm{Nb}} \\ \overline{r}_1 \\ \overline{r}_2 \\ \overline{r}_3 \\ \vdots \end{pmatrix}, \qquad (4.5)$$

with concentrations $c_{x,y}$, where the first index denotes the element. The second index $i = \{1, 2, 3, \dots\}$ corresponds to different HEA (e.g., 1 =AlCrMoTi).

For example, $c_{\text{Nb},1} = 0$ yields AlCrMoTi that is represented by index 1 and $\overline{r}_1$ corresponds to the mean atomic radius measured by XRD[5]:

$$c_{\text{Cr},1} \cdot r_{\text{Cr}} + c_{\text{Mo},1} \cdot r_{\text{Mo}} + c_{\text{Nb},1} \cdot r_{\text{Nb}} + c_{\text{Al},1} \cdot r_{\text{Al}} + c_{\text{Ti},1} \cdot r_{\text{Ti}} = \overline{r}_1, \tag{4.6}$$

with 1 =AlCrMoTi, $c_{\text{Nb},1} = 0$ and $c_{\text{Al},1} = c_{\text{Cr},1} = c_{\text{Mo},1} = c_{\text{Ti},1} = 0.25$.
Although this model is an improvement compared to using the atomic radii from pure metals, this method still suffers from some constraints. First, the model assumes that the r_i are independent of the specific alloy. Second, the model neglects the influence of the varying chemical environments. The following section investigates the influence of the specific alloy system on the mean atomic radii and the specific atomic environment.

4.3.1 Standard Deviation of interatomic distances and atomic volumes

This section presents standard deviations of interatomic distances and atomic volumes of different BCC HEA from Al-Cr-Mo-Nb-Ti alloys and the Hf-Nb-Ta-Ti-Zr system. The quantities serve as descriptors of lattice distortions accessible from DFT calculations.
The equations

$$\sigma^b = \frac{1}{b}\sqrt{\frac{1}{N_{\text{bonds}}}\sum_i^{N_{\text{bonds}}} (\overline{r}^{\langle 111\rangle} - r_i^{\langle 111\rangle})^2} \tag{4.7}$$

$$\sigma^a = \frac{1}{a_0}\sqrt{\frac{1}{N_{\text{bonds}}}\sum_i^{N_{\text{bonds}}} (\overline{r}^{\langle 100\rangle} - r_i^{\langle 100\rangle})^2} \tag{4.8}$$

$$\sigma^V = \frac{1}{\overline{\overline{V}}}\sqrt{\frac{1}{N_{\text{atoms}}}\sum_j^{N_{\text{atoms}}} (\overline{V} - V_j)^2}, \tag{4.9}$$

define the normalized standard deviations with $r_i^{<111>}$ and $r_i^{<100>}$, the nearest neighbour distances in $\langle 111\rangle$-directions and nearest neighbour distances in $\langle 111\rangle$-directions, and the atomic volumes V_j. The site or bond-specific values are directly extracted from relaxed supercells. The relaxation process minimized the interatomic forces F_i until the convergence criterion of $F_i < 0.01$ eV/Å has been reached. The normalization corresponds to the atomic volume of the relaxed supercell $b = \frac{\sqrt{3}}{2} a_0 = \frac{\sqrt{3}}{2}\left(\frac{2V}{N_{\text{atoms}}}\right)^{\frac{1}{3}}$. Consequently the quantities

$$\overline{r}^{\langle 111\rangle} = \frac{1}{bN_{\text{bonds}}}\sum_i^N r_i^{\langle 111\rangle} \tag{4.10}$$

$$\overline{r}^{\langle 100\rangle} = \frac{1}{a_0 N_{\text{bonds}}}\sum_i^N r_i^{\langle 100\rangle}, \tag{4.11}$$

which describe the normalized average of all next neighbor distances in $\langle xyz\rangle$ - directions are close to one, while the mean value of the normalized distribution of the atomic volumes $\overline{V}$ is exactly one. Figure 4.5 shows exemplary the normalized bond length distribution in $\langle 100\rangle$-directions of AlCrMoTi. The Gaussian fit function shows that the distribution is approximately normally distributed, suggesting that the corresponding standard deviations are reasonable quantities to describe the distorted HEA lattice.

Figure 4.6 compares the calculated standard deviations and the atomic size difference δ of different Al-Cr-Mo-Nb-Ti and Hf-Nb-Ta-Ti-Zr alloys. The atomic size difference values of alloys have been calculated using Equation 4.4 with r_i from DFT calculations, where all elements are considered in BCC configuration (see Table A.1). In Al-Cr-Mo-Nb-Ti alloys σ^b, σ^a, σ^V and δ increase with increasing Cr-concentration c_{Cr}, while the influence of c_{Nb} is comparable weak. Among the values extracted from relaxed SQS, the data reveal $\sigma^b < \sigma^V < \sigma^a$ for all tested HEA, which indicates that the longer bond length in $\langle 100\rangle$-directions leads to a broader nearest-neighbor distance distribution. This effect is especially pronounced in HfNbTiZr and HfNbTaTiZr.

Interestingly, all quantities extracted from relaxed SQS describe a more distorted lattice of Hf-Nb-Ta-Ti-Zr alloys compared to Al-Cr-Mo-Nb-Ti lattice alloys. At

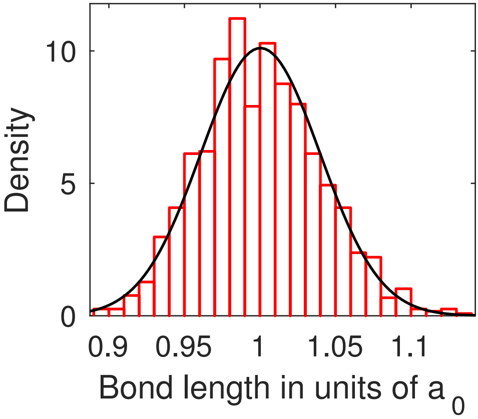

Figure 4.5: Red: Bond length distributions of a random supercell with 512 atoms representing AlCrMoTi normalized by the mean lattice parameter a_0. Black: Gaussian fit function

the same time, the atomic size difference indicates a less distorted lattice of HfNbTiZr and HfNbTaTiZr compared to AlCrMoNbTi, AlCrMoNb$_{0.17}$Ti and AlCrMoTi. Here the question arises whether inaccurate r_i values or the influence of the specific chemical environment lead to discrepancies between σ^a, σ^b, σ^V, and δ. A strong atomic environment influence can cause a broadening of the standard deviations of atomic bond lengths and consequently induce a nonlinear relationship between δ and $\sigma^{a/b/V}$ and question the validity of Vegard's law.

In order to understand the single relationships between σ^a, σ^b, σ^V and δ, Figure 4.7 compares their linear correlations. The data reveal an almost perfect linear relation (q=0.99) between σ^b and σ^V. This result implies that the different atomic radius values still play a crucial role since contractions and dilatations around the atoms cause atomic volume fluctuations. A dominant influence of the atomic environment would cause a somewhat random distribution of next-neighbor bond lengths and weaken the appearance of contractions and dilatation of atomic volumes. The standard deviations σ^b, σ^a and σ^V show a linear relation with $\sigma^a \approx 0.79 \cdot \sigma^V$ and $\sigma^b \approx 1.44 \cdot \sigma^a$. The prefactor 1.44 shows that σ^a is generally larger than σ^b. Broader distributions of $\langle 100 \rangle$-interatomic distances are

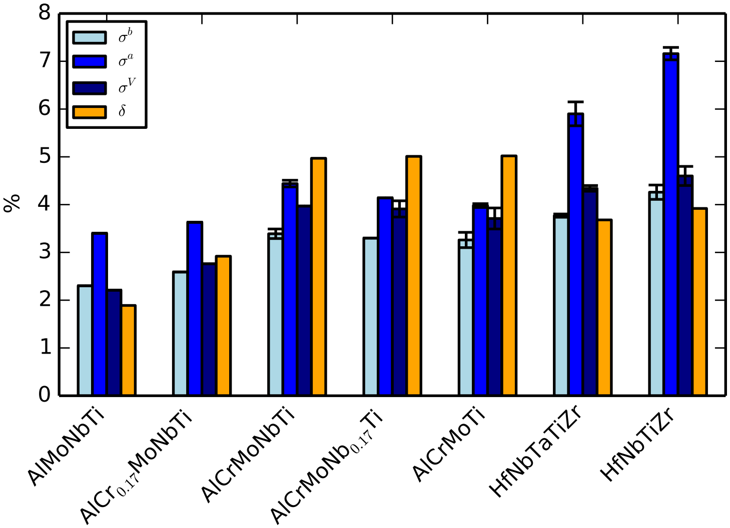

Figure 4.6: Normalised standard deviations of atomic volumes and nearest neighbor interatomic distances in $\langle 111 \rangle$- and $\langle 100 \rangle$-directions compared to the atomic size difference.

reasonable since the interatomic forces are expected to be smaller between two atoms in $\langle 100 \rangle$-directions compared to two atoms in (shorter) $\langle 111 \rangle$-directions. Consequently, the influence of the specific atomic environment is more prominent on $\langle 100 \rangle$-interatomic distances compared to $\langle 111 \rangle$-interatomic distances.

The linear correlation of σ^a and σ^V is less pronounced compared to σ^b and σ^V (q=0.81 vs q=0.99). The weaker linear correlation indicates that the distortions in $\langle 100 \rangle$-directions are partially volume conserving. The data further shows that the broadening of the $\langle 100 \rangle$-nearest neighbor distances is more pronounced for alloys from the Hf-Nb-Ta-Ti-Zr system, which indicates that the atomic environment influence is more decisive in this system. The volume-conserving distortions lead to deviations from cubic symmetry. This observation suggests that the high share of HCP elements causes the volume-conserving lattice distortions in $\langle 100 \rangle$-directions of the Hf-Nb-Ta-Ti-Zr alloys.

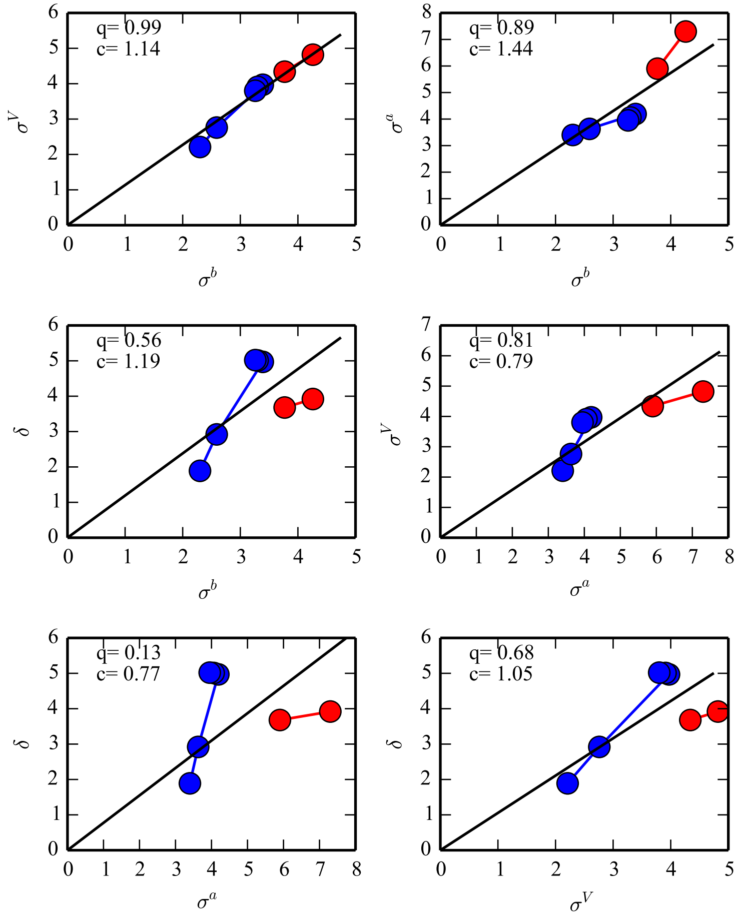

Figure 4.7: Linear correlations of σ^a, σ^b, σ^V and δ. Blue dots correspond to HEA from the Al-Cr-Mo-Nb-Ti alloys, and red dots to HEA from the Hf-Nb-Ta-Ti-Zr system. The quantities q and c denote the linear correlation coefficient and the slope of the linear fit function ($y = c \cdot x$)

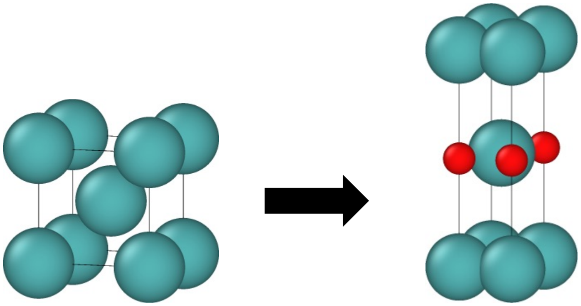

Figure 4.8: Schematic picture of volume conserving distortions on a BCC unit cell (blue atoms) in $\langle 100 \rangle$-directions. The BCC unit cell becomes HCP-like, possibly offering space for interstitials (red atoms) at the octahedral sites.

Figure 4.8 schematically pictures the corresponding distorted BCC cell. Here the question arises whether the observed anisotropy of $\sigma^{\langle xyz \rangle}$ influences the mechanical properties of BCC HEA via an increased receptivity for interstitial atoms. It is conceivable that the comparable high σ^a-values of HfNbTiZr and HfNbTaTiZr lead to an increased receptivity for interstitials in octahedral sites of these alloys. An ab initio study revealed that the octahedral sites are preferred over the tetrahedral sites by C atoms[74]. It further found a wide range of the corresponding solution energy. There exist further indications that oxygen doping increases both strength and ductility of BCC HfNbTiZr[75].

Besides influencing the mechanical properties indirectly by interstitials, there exists the possibility that the $\sigma^{\langle hkl \rangle}$ anisotropy directly influences the mechanical properties through a dislocation solute interaction. Spherical defects, like solutes in dilute alloys, only interact with edge dislocations. However, the analysis of the different interatomic distances of this work showed that in the non-dilute case of HEA, the combination of different solutes led to non-spherical defects, which interact with screw dislocations as well[13]. Hence future studies could address the influence of non-spherical defects on the dislocation solute interaction energy, especially in alloys like HfNbTaTi and HfNbTiZr, which have a pronounced anisotropy of $\sigma^{\langle hkl \rangle}$.

The atomic size misfit shows a weak linear correlation ($q<0.7$) with σ^b, σ^a, and

σ^V, which provides evidence that the atomic radius values from pure elements differ from the ones realized in the HEA. Since the data revealed strong indications that the atomic environment plays not a crucial role for σ^b and σ^V, we suggest the following working hypothesis: The atomic size difference is linearly related to σ^b and σ^V. However, the specific atomic radius values r_i are alloy (-system) specific. The following section will test the stated hypothesis.

4.3.2 Interatomic mean distances

In order to test the latter hypothesis, element-specific bond lengths have been extracted from minimized SQS to calculate the element-pair specific mean bond lengths:

$$\overline{r}^{xy}_{\text{SQS}} = \frac{1}{N_{\text{xy}}} \sum_{i}^{N_{\text{xy}}} r_i^{\text{xy}}. \tag{4.12}$$

Here xy stands for the elements forming the bond (e.g., Al-Al, Al-Ti, Hf-Zr, ...). In the next step, the function

$$f(r^i_{\text{opt}}) = \sum_{i=1} (\overline{r}^{ii}_{\text{SQS}} - r^i_{\text{opt}})^2 + \sum_{i<j} (\overline{r}^{ij}_{\text{SQS}} - \frac{1}{2}(r^i_{\text{opt}} + r^j_{\text{opt}}))^2, \tag{4.13}$$

has been minimized with respect to the variables $r^{i/j}_{\text{opt}}$. The indices i and j run over the elements of the considered HEA (e.g., i =Al, Cr, Mo, Ti). The optimization process yields the atomic radius values r^i_{opt} of the specific elements within the considered alloy. Note that $\min\left[f(r^i)\right]$ is a measure for the validity of Vegard's law in the considered alloy. In a third step, Vegard's law has been used to determine the element-specific bond lengths r^{xy}_{el} with atomic radius values from pure elements.

Figures 4.9 and 4.10 compare the atom-specific nearest neighbor distances (in $\langle 111 \rangle$- and $\langle 100 \rangle$-directions) in AlCrMoTi and HfNbTiZr resulting from different approaches. The analysis reveals, that the values r^{xy}_{opt} reproduce the values of $\overline{r}^{xy}_{\text{SQS}}$

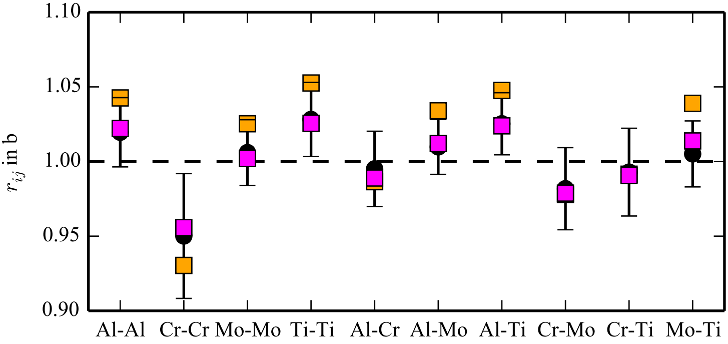

(a)

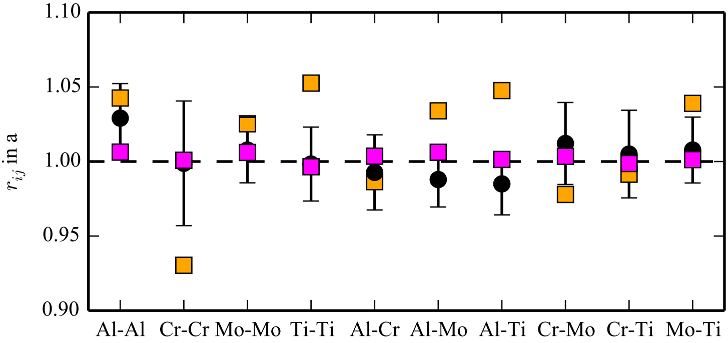

(b)

Figure 4.9: Atom specific interatomic mean bond lengths of AlCrMoTi from different approaches in a) $\langle 111 \rangle$-directions and b) in $\langle 100 \rangle$-directions. **Black dots**: Values directly extracted from relaxed SQS. Here, the error bars correspond to the standard deviation. **Orange squares:** Values correspond to the approach from Chen et al.[5]. **Magenta squares:** Values from the approach presented in this work (Equation 4.13)

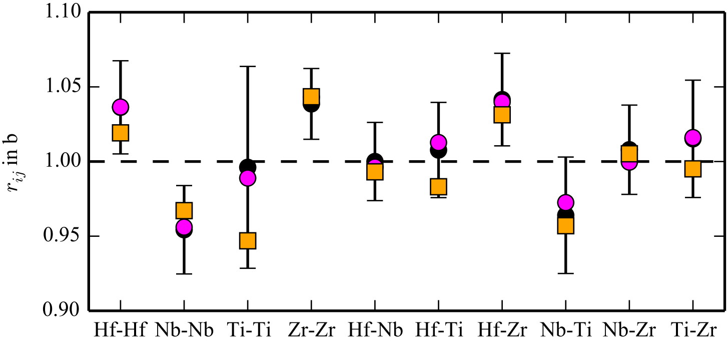

(a)

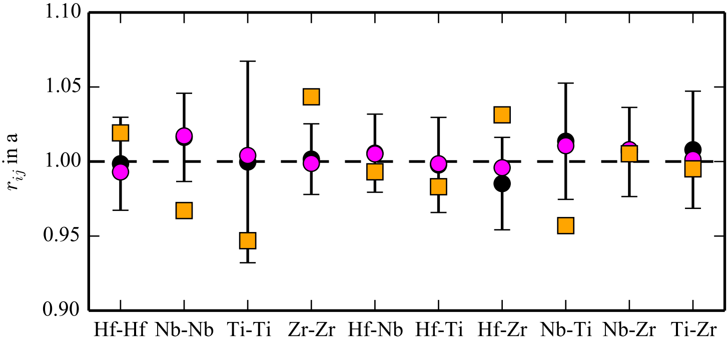

(b)

Figure 4.10: Atom specific interatomic mean bond lengths of HfNbTiZr from different approaches in a) $\langle 111 \rangle$-directions and b) in $\langle 100 \rangle$-directions. **Black dots:** Values directly extracted from relaxed SQS. Here, the error bars correspond to the standard deviation. **Orange squares:** Values correspond to the approach from Chen et al.[5]. **Magenta squares:** Values from the approach presented in this work (Equation 4.13)

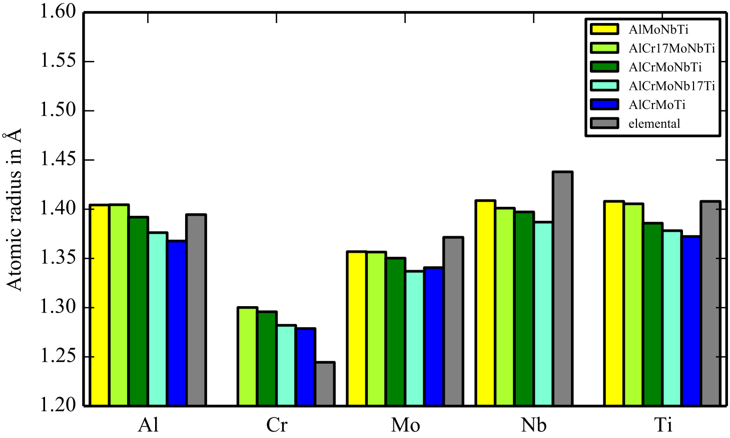

Figure 4.11: Mean atomic radius values of different atoms from HEA from the Al-Cr-Mo-Nb-Ti system compared to atomic radius values from pure elements in BCC configuration.

more accurately as r_{el}^{xy}. This finding indicates that the atomic radius values are alloy specific. Figure 4.11 supports this finding by illustrating $\overline{r}_{\mathrm{SQS}}^{xx}$ in different Al-Cr-Mo-Nb-Ti alloys. The data reveal that the atomic radius values follow the trend of the lattice constant a_0. Increasing c_{Cr} and decreasing c_{Nb} lead to a reduction of a_0 and, simultaneously, the atomic radius values of Al, Cr, Nb, and Ti. Only the atomic radius of Mo is slightly increased in AlCrMoTi compared to the one in AlCrMoNb$_{0.17}$Ti. However, the difference is small and may be attributed to fluctuations resulting from the SQS approach.

One can further observe that the differences between r_{el}^{xy} and r_{SQS}^{xy} are increased for the $\langle 100\rangle$-directions compared to the values corresponding to the $\langle 100\rangle$-directions. This can be rationalized by the observation, that in $\langle 100\rangle$-directions the $\overline{r}_{\mathrm{SQS}}^{xy}$ values fluctuate compared to $\overline{r}_{\mathrm{el}}^{xy}$ more closely around the mean lattice constant a_0. In other words, the interatomic distances in $\langle 100\rangle$-directions, predicted by DFT, adapt the value of the mean lattice constant of the alloy and hence deviate from the element-specific values suggested by Vegard's law. The data reveals that the bond length distribution of nearest neighbor bonds in $\langle 100\rangle$-directions is broader than that in $\langle 111\rangle$-directions.

Within the approach of the SSS model[5], two aspects influence the individual interatomic distances:

- The atomic radii of both contributing atoms.
- The specific atomic environment.

The broader bond length distribution in $\langle 100 \rangle$-directions can be interpreted as an increased influence of the specific atomic environment.
In the third step, the analysis uses the adapted atomic radii to recalculate the atomic size difference δ via Equation 4.4. The atomic radii r^i_{opt}, which minimized equation 4.13, served as input paramezer r_i, yielding δ^b and δ^a.
Figure 4.12 analyzes the linear correlation between σ^b and δ^b and the linear correlation between σ^a and δ^a. It shows an excellent linear correlation between σ^b and δ^b (q=0.99), while the correlation of σ^a and δ^a is almost zero. The poor correlation of σ^a and δ^a further indicates the dominant influence of the specific atomic environment on the nearest neighbor distances in $\langle 100 \rangle$-directions. The data further reveal that the difference between δ and δ^b is increasing with

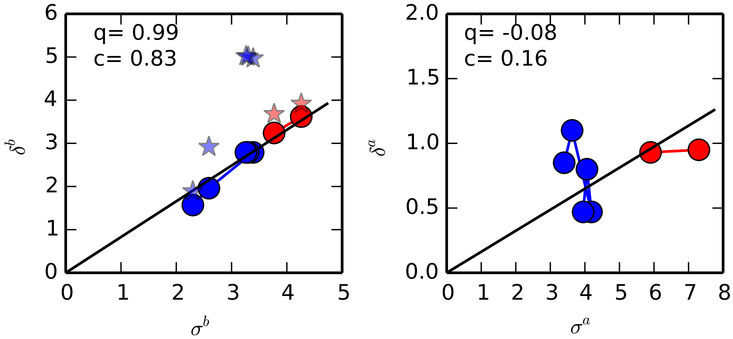

Figure 4.12: Linear correlations of σ^a, σ^b and recalculated δ. Blue dots correspond to Al-Cr-Mo-Nb-Ti HEA, and red dots to HEA from the Hf-Nb-Ta-Ti-Zr system. Stars correspond to the delta values from the atomic radii of pure elements. The quantities q and c denote the linear correlation coefficient and the slope of the linear fit function $(y = c \cdot x)$

increasing Cr-concentration of the alloy. An analysis of Figure 4.11 sheds light on the origin of this behavior. An increasing c_{Cr} leads to increasing differences between the atomic radii one would find in pure metals and atomic radii one finds in the alloy

$$\Delta r^i = |r^i_{\text{el}} - \overline{r^i}_{\text{opt}}|. \tag{4.14}$$

Only for i=Cr, Δr^i is decreased with increasing c_{Cr}. Hence, in this case, δ is an unsuitable descriptor for lattice distortions in Al-Cr-Mo-Nb-Ti HEA since it overestimates the lattice distortions for alloys with high c_{Cr}. Using δ as an input parameter for solid solution strengthening theories leads to overestimating the strengthening contributions due to lattice distortions in Al-Cr-Mo-Nb-Ti HEA with high c_{Cr}.

4.3.3 Misfit parameter

This work aims to explain the connection between the distinct chemical composition and the macroscopic mechanical properties of BCC HEA, like strength and ductility. Recently, solid solution-strengthening (SSS) theories [48,36,33] predicting the strength of HEA through the key misfit parameter

$$M_v = \sqrt{\sum_i^N c_i \left(\Delta \overline{V}_i^2 + \sigma^2_{\Delta V_i}\right)}, \tag{4.15}$$

The quantity $\Delta \overline{V}_i = \overline{V} - \overline{V}_i$ denotes the average misfit volume of solute i and $\sigma^2_{\Delta V_i}$ the corresponding standard deviation. The standard deviation takes the influence of the specific chemical environment into account and is usually neglected [36]. Further, pure elements' atomic radii are often used to determine $\overline{V}_i$ instead of performing direct calculations [5,33]. This section investigates the influence of including standard deviations and the resulting error from using pure metal atomic radii instead of the actual alloy atomic radii.

Figure 4.13 depicts the misfit parameters from DFT calculations with and without taking the standard deviation into account M_v, $M_v^r = \sqrt{\sum_i^N c_i \Delta \overline{V}_i^2}$, and the misfit parameter calculated with atomic radii from pure elements $M_v^{\text{pure}} = \sqrt{\sum_i^N c_i \Delta\overline{V}_{i,\text{pure}}^2}$. The data reveal larger values of M_v^{pure} compared to M_v,

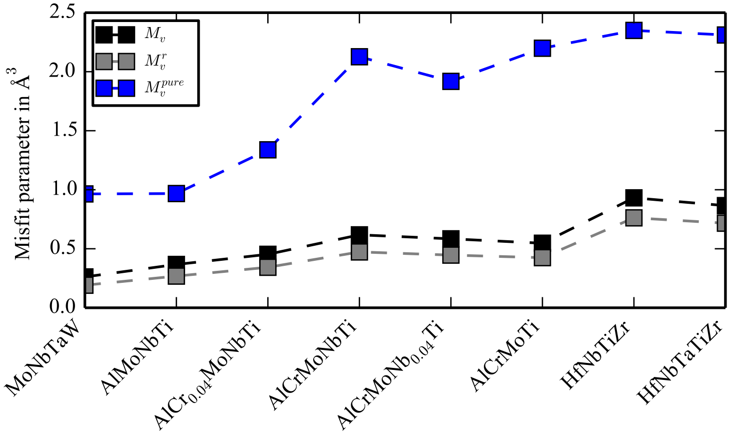

Figure 4.13: Misfit parameter from DFT calculations with and without taking $\sigma_{\overline{V}_i}$ into account (black and grey dots) compared to misfit parameter calculated with atomic radii from pure elements (blue dots).

which can be explained from the finding in the previous section. We showed that the mean atomic radii in the alloy seek to reduce the difference between themselves and the mean atomic radius, which consequently reduces the single atomic misfit volume $\Delta\overline{V}_i$.

The difference between M_v and M_v^r is comparatively small. All parameters show increasing values for increasing x in AlCr$_x$MoNbTi. They have further in common that HfNbTiZr and HfNbTaTiZr have higher misfit parameter values than Al-Cr-Mo-Nb-Ti HEA. The DFT-calculated parameter M_v and M_v^r are almost constant and only slightly decreasing in AlCrMoNb$_x$Ti with decreasing x, while M_v^{pure} shows an alternating course. The misfit parameter of MoNbTaW is the smallest among the tested alloys independent of the calculation method.

Figure 4.14 illustrates a correlation analysis of the misfit parameters M_v, M_v^r, and M_v^{pure}. The analysis reveals an excellent linear correlation (q=1.0) between M_v

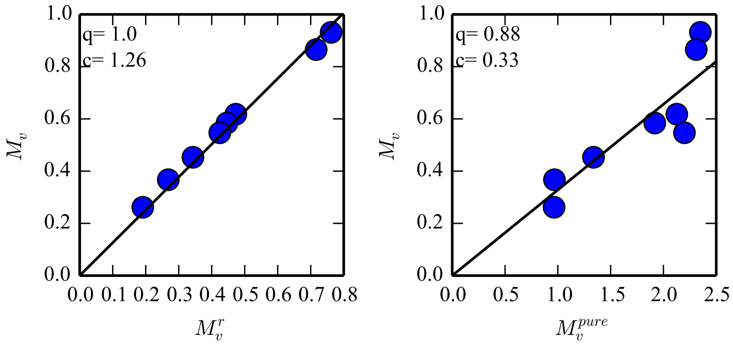

Figure 4.14: Linear correlations between misfit parameters from different calculation methods.

and M_v^r. The excellent linear correlation indicates that the influence of the chemical environment scales with the corresponding misfit volume $\Delta\overline{V}_i = c \cdot \sigma_{\Delta V_i}$. The data further suggest that there exists a linear correlation (q=0.88) between M_v and M_v^{pure}, which supports the idea that M_v^{pure} is a reasonable input parameter for solid solution strengthening theories since it can capture the primary trend of atomic volume fluctuations of different HEA.

However, M_v^{pure} overestimates the fluctuations predicted by DFT calculations. The overestimation can be attributed to the previous section's observation that the different solutes' atomic radii can partially adapt to the HEA's mean atomic radius. Hence, the findings suggest that the parameter M_v presented in this work delivers improved accuracy in describing the atomic volume fluctuations of different HEA. However, further studies are necessary to clarify if this improvement is relevant for predicting HEA strength or if other uncertainties resulting from approximations within the solid solution strengthening theory superimpose the improved accuracy of the misfit parameter is superimposed.

4.3.4 Influence of crystallographic ordering in AlCrMoTi on the misfit parameter

This section investigates the influence of B2-type crystallographic ordering in AlCrMoTi on the misfit parameter M_v. The misfit parameters have been calculated according to the method described in the previous section, with four 128-atom SQS for each lattice structure. The investigated lattice structures are the disordered AlCrMoTi and the ordered (Al)(Ti) CrMo, and (AlMo)(CrTi). According to Section 3.1, these configurations are energetically favored. The SQS have been relaxed with respect to atomic positions, while the cubic cell shape remained fixed. Figure 4.15 compares the resulting mean misfit parameter of AlCrMoTi, (Al)(Ti)CrMo and (AlMo)(CrTi) with the misfit parameters of other derivatives from the Al-Cr-Mo-Nb-Ti family and with HfNbTiZr and HfNbTaTiZr. The data indicate that the differences between the misfit parameters of AlCrMoTi, (Al)(Ti) CrMo, and (AlMo)(CrTi) are minor compared to the misfit parameters of chemically different alloys. Observations of the standard deviations indicate that fluctuations

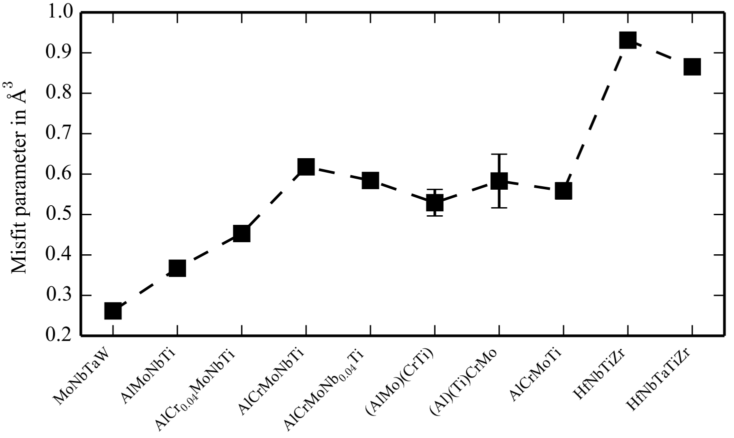

Figure 4.15: Misfit parameter of different BCC HEA and differently ordered AlCrMoTi. In the case of AlCrMoTi, the standard deviation is smaller than the marker size.

due to different spatial atomic arrangements superimpose possible effects from the crystallographic ordering. Thus, the influence of crystallographic ordering on the misfit parameter is small and can be neglected in our alloy systems.

For the CoFeNiTi, a different trend was observed. The FCC HEA showed a decreasing misfit parameter with an increasing degree of chemical short-range order (Ti-Fe pairs) in FCC CoFeNiTi[76]. The different trends of the BCC HEA in this work and the FCC HEA[76] are consistent with the BCC preference effect. The BCC preference effect states that the energetic costs of lattice distortions are smaller in BCC alloys than in FCC alloys[73]. Based on the BCC preference effect, in BCC crystals, the energetic advantage due to the reduction of lattice distortions is smaller than in FCC crystals. Thus, it is likely that increasing the number of energetically favorable bonds drives ordering in BCC HEA more than the reduction of lattice distortions.

Of course, these results are insufficient to make a general statement for all BCC HEA. Especially if the energetic differences of different bond types are minor, minimizing lattice distortions may be able to drive ordering. Hence, further studies are necessary to make more general statements about the interplay between crystallographic ordering and lattice distortions in BCC HEA.

4.3.5 Conclusions

This section analyzed the interatomic distance distributions in $\langle 111 \rangle$- and $\langle 100 \rangle$-directions and the atomic volume distribution of a series of BCC HEA from the Al-Cr-Mo-Nb-Ti and Hf-Nb-Ta-Ti-Zr systems. The distributions have been directly extracted from relaxed supercells, representing the random alloys. The atom specific nearest-neighbour interatomic mean distances $\overline{r}^{xy}$ have been calculated in $\langle 111 \rangle$- and $\langle 100 \rangle$-directions as well as their corresponding normalized standard deviations σ^b and σ^a. The normalized standard deviations of the atomic volumes σ^V have been calculated. Additionally, the atomic size misfit δ has been calculated using elemental atomic radii from DFT calculations. Finally, the misfit parameter, the input parameter for recent solid solution strengthening theories, has been calculated using different approaches. Two misfit parameters have been directly extracted from relaxed supercells with and without considering the specific chemical environment's influence. Another misfit parameter M_v^{pure} was calculated with the atomic radii of the pure elements.

- In Al-Cr-Mo-Nb-Ti HEA, lattice distortions increase with increasing Cr concentration. Lattice distortions in HfNbTiZr and HfNbTaTiZr are more pronounced than lattice distortions of Al-Cr-Mo-Nb-Ti HEA.
- The atomic size difference δ calculated with atomic radii from pure metals is not an accurate descriptor for lattice distortions since an increasing value of δ leads to an increasing overestimation of the actual distortions. The overestimated lattice distortions lead to an overestimated strength of such alloys by solid solution strengthening theories using δ as an input parameter.
- The atomic size difference δ calculated with adapted atomic radii correlates excellently with the standard deviation of nearest neighbor distances.
- The adapted atomic radii are sensitive to the chemical composition of the considered alloy.
- The specific atomic environment has an increased influence on the interatomic nearest neighbor distances in $\langle 100 \rangle$-directions.
- The DFT method presented in this work improves the accuracy of the misfit parameter, an essential input parameter for many solid solution-strengthening theories.
- The influence of crystallographic ordering on the misfit parameter of AlCrMoTi is negligible.

4.4 Generalized Stacking fault energies

This section analyzes the GSFE of the BCC HEA AlCrMoTi and HfNbTiZr. GSFE allow an analysis of bond strengths beyond the limits of linear elasticity [58]. Analytic GSFE functions can be used within other models, e.g., as a place-in for the Peierls energy within the Peierls Nabarro Model [15,39], to study deformation mechanisms based on dislocation mobility. Here the study focuses on GSFE maxima since they can serve as dislocation pinning points and consequently influence the dislocation mobility [39]. Since the results presented in Chapter 3 indicate that AlCrMoTi is B2-type ordered at RT, this chapter investigates the influence of crystallographic ordering on the GSFE. Here, the study focuses on GSFE minima (at multiples of b) since positive or negative values cause antiphase boundary energies, which can influence dislocation mobility.

4.4.1 Generalized Stacking fault energies of disordered AlCrMoTi and HfNbTiZr

This section analyzes the GSFE of chemically disordered AlCrMoTi and HfNbTiZr. The presented data have been revealed by the method described in Section 2.5. Electronic ground state energy calculations have generated the necessary input parameters.

For the DFT-calculations, a SQS with dimensions $8 \times 4 \times 8$ ($N_{\text{atoms}} = 256$) has been used. The SQS was oriented in a way that the x-, y- and z-direction are parallel to $\langle 111 \rangle$- , $\langle 110 \rangle$ and $\langle 112 \rangle$-directions. The discrete displacements x sampled at least all minimum ($x_n = nb$) and maximum ($x_n = \frac{bn}{2}$) positions of the fault plane. The calculations have been performed considering three different symmetry equivalent fault planes for each alloy composition. The calculation setup included a cutoff energy of 600eV, a $3 \times 3 \times 3$ k-point mesh, and the Methfessel-Paxton method with a smearing parameter of $0.1\mathrm{eV}$. Atomic positions have been relaxed perpendicular to the fault plane (1D) or without constraints (3D). The cubic cell shape has been conserved. The convergence criterium for the relaxation loop was set to a force per atom of $0.01\mathrm{eV/\AA}$.

Figure 4.16 illustrates exemplary the calculated GSFE-values of three different planes of HfNbTiZr as well as the adapted theoretical GSFE (or γ)-function from equation (2.11). The sinusoidal γ function follows the mean course of the single calculated GSFE-values, whereby it cannot describe the influence of chemical fluctuations. The influence of chemical fluctuations is considered by evaluating the standard deviation $\sigma_{\gamma_\mathrm{u}}$ of the unstable stacking fault energies, following the approach presented in Section 2.5.

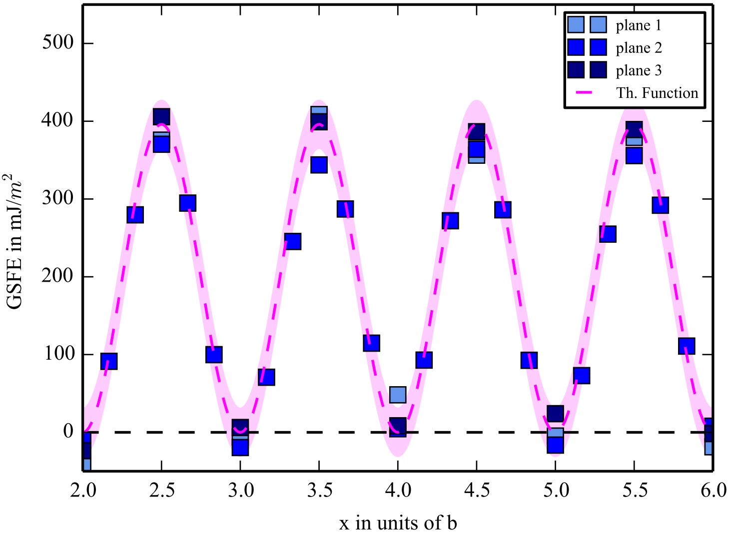

Figure 4.16: GSFE of BCC HEA HfNbTiZr. Squares denote discrete GSFE-values from DFT-values. The broken line illustrates the sinusoidal γ-surface. The standard deviation indicated by the shaded area describes the influence of chemical fluctuations.

Figure 4.17 compares the average unstable stacking fault energies $\overline{\gamma}_\mathrm{u}$ of AlCrMoTi and HfNbTiZr from this work with DFT values of BCC metals[77]. The DFT calculated γ_u-values of pure BCC metals can be divided into two groups: Low and high USF energies.

The first group is Nb, V, and Ta with γ_u values $\approx 700\mathrm{mJ/m^2}$. In the second group

	γ_{us} [mJm^{-2}]		τ_{max} [GPa]	
	val	min/max	val	min/max
HfNbTiZr	396 ± 30	327/461	3.48	2.90/4.22
AlCrMoTi	717 ± 74	571/857	7.30	5.81/8.71

Table 4.3: Unstable stacking fault energy values in mJm^{-2} and ideal shear stress in GPa of AlCrMoTi and HfNbTiZr.

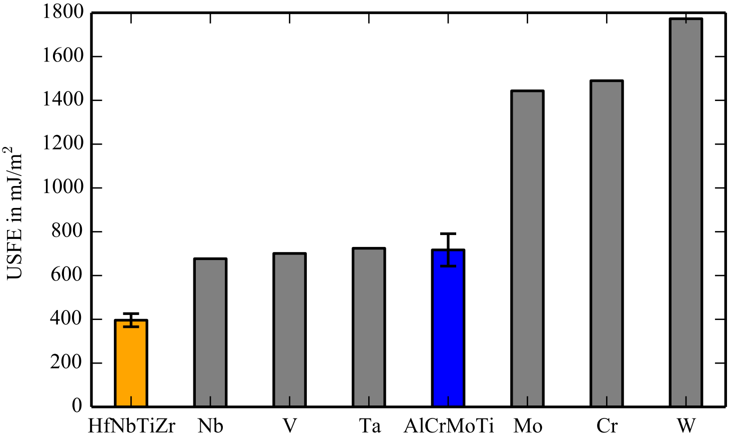

Figure 4.17: Unstable stacking fault energy from DFT calculations of BCC HEA AlCrMoTi and HfNbTiZr compared to values of BCC metals. The error bars denote the standard deviation resulting from calculating the USFE from various displacements within different symmetry equivalent fault planes of the same SQS.

are Mo, Cr, and W, which have values approximately twice as high. The results of this work reveal that AlCrMoTi belongs to the first group. The BCC HEA HfNbTiZr has a γ_{u}-value $\approx 40\%$ lower as the γ_{u}-values of Nb, V and Ta. The exceptionally low γ_{u} might be connected to the high share of non-BCC elements in HfNbTiZr, which could reduce interatomic bond strength.

Besides the unstable stacking fault energies, the corresponding standard deviations are evaluated. The data indicate a wider distribution of γ_{u}-values in AlCrMoTi compared to the ones in HfNbTiZr. The γ_{u}-values of AlCrMoTi have a standard deviation $\sigma_{\gamma_\mathrm{u}} = 74\mathrm{mJ/m}^2$, while $\sigma_{\gamma_\mathrm{u}}$ corresponding to HfNbTiZr is only $30\mathrm{mJ/m}^2$. Thus, $\sigma_{\gamma_\mathrm{u}}$ corresponding to HfNbTiZr is lower by factor ≈ 0.4 compared to the corresponding AlCrMoTi $\sigma_{\gamma_\mathrm{u}}$. In order to exclude the possibility that these findings can be attributed to the different fault areas A, which are used to normalize stacking fault energies with different lattice constants, the energy standard deviations have been recalculated without any normalization. The standard deviations, not normalized by the fault area, yield $\gamma = 503\mathrm{meV}$ for HfNbTiZr and $\gamma = 1003\mathrm{meV}$ for AlCrMoTi. This finding that the standard deviation without normalization is still increased for AlCrMoTi indicates that it results from an increased dependency of the fault energy on the distinct chemical environment along the fault plane. The results presented in Section 3.1 suggest a lack of ordering in HfNbTiZr. The lack of ordering indicates that in HfNbTiZr, the entropy term is dominant, and energy differences between different bonds (e.g., Hf-Hf, Hf-Nb) are minor. Consequently, the low energy differences between different bonds could explain the low standard deviation of GSFE in HfNbTiZr, since this causes a minor contribution of the specific chemical environment along the fault plane. In contrast, the high energy differences between different bonds could explain the low standard deviation of GSFE in AlCrMoTi.

This section focused on the GSFE belonging to disordered AlCrMoTi and HfNbTiZr. The following section will investigate the influence of the crystallographic ordering of AlCrMoTi on its GSFE.

4.4.2 Influence of crystallographic ordering on stacking fault energies in AlCrMoTi

This section investigates the influence of crystallographic ordering on the GSFE of AlCrMoTi. The first part comprises a theoretical discussion of the influence specifically on the stacking fault energies resulting from nb-displacements in the context of the Broken Bond Model.

4.4.2.1 The Broken Bond Model

The γ-surface is supposed to reflect the symmetry of the underlying lattice since introducing a B2-type ordering in a random structure changes the shortest lattice invariance from b to $2b$ (see Figure 4.18). In the limit of an infinite-sized supercell, this changes the periodicity of the γ-surface cross-section of a $\{110\}$-plane in $\langle 111\rangle$-directions from $1b$ to $2b$, with $\gamma^{\infty}(2b) \neq \gamma^{\infty}(b)$.

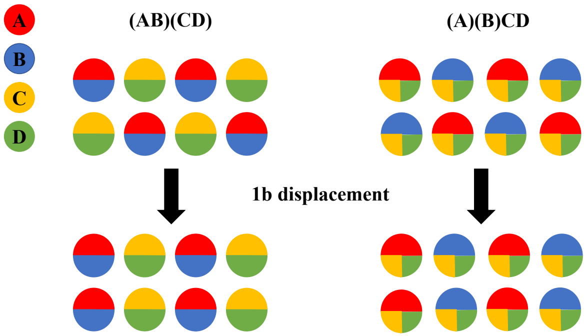

Figure 4.18: Schematic illustration of the shear antiphase boundary (SAPB) created by an uneven displacement $(2n+1)b$ on a B2-type ordered lattice structure.

Since applying a displacement of Burgers vector b creates an antiphase boundary, the corresponding stacking fault energy $\gamma^{\infty}(b)$ can be denoted as shear antiphase boundary energy (SAPBE). The SAPBE depends on the degree of ordering and the individual chemistry of the specific alloy and is related to the γ-surface:

$$E^{\mathrm{SAPB}} = \gamma^{\infty}(2b) - \gamma^{\infty}(b). \tag{4.16}$$

The Broken Bond Model approximates E^{SAPB} of a perfectly B2-ordered two-component alloy by

$$E^{\mathrm{SAPB}} = \frac{2\sqrt{2}}{a_0^2}\frac{1}{2}\left(W_{\mathrm{AA}} + W_{\mathrm{BB}}\right) - W_{\mathrm{AB}}, \tag{4.17}$$

with bond energies, W_{AB} of bonds between element A and B [12]. The basic idea of the model is that the energy difference between the initial and the sheared lattice configuration results from the change of direct neighbor bonds. Contributions of higher-order bonds, like triplets or bonds beyond nearest neighbors, are neglected. In order to describe a partially ordered instead of a fully ordered alloy, one hast to adapt Equation (4.17) by introducing bond share probabilities. Tables 4.4 and 4.5 describe the bond share probabilities within (Al)(Ti)CrMo and (AlMo)(CrTi) corresponding to the unsheared and $1b$-sheared configuration.

According to the given probabilities, one can rewrite equation (4.17) for partially ordered (Al)(Ti)CrMo given by

$$E^{\mathrm{SAPB}}_{\mathrm{(Al)(Ti)}} = \frac{2\sqrt{2}}{a_0^2}\left[\frac{1}{8}\left(W_{\mathrm{AlAl}} + W_{\mathrm{TiTi}}\right) - \frac{1}{4}W_{\mathrm{AlTi}}\right]. \tag{4.18}$$

The SAPBE of (AlMo)(CrTi) involves additional bond pairs, which have been neglected here. The results from Section 3.1.1 indicate that changes of W_{AlTi} and W_{AlAl} dominate the systems energy change since they are the energetically favorable bonds. In contrast, the other bond types contribute similarly to the overall system's energy. Hence, the SAPBE of partially B2-ordered AlCrMoTi can be modeled by

$$E^{\mathrm{SAPB}}_{\mathrm{B2}} = \frac{2\sqrt{2}}{a_0^2}\left[\frac{1}{8}W_{\mathrm{AlAl}} - \frac{1}{4}W_{\mathrm{AlTi}} + \frac{1}{8}W_{\mathrm{ex}}\right], \tag{4.19}$$

where W_{exc} stands for the energy contribution according to all non-Al-Al and Al-Ti bonds.

Approximating $W_{\mathrm{AlAl}} = W_{\mathrm{AlTi}}$ yields that the introduction of a SAPB into partially ordered AlCrMoTi reduces the share of energetically favorable bonds by $\frac{1}{8}$. In

	Al	Ti	Cr	Mo
Al	0 (0.125)	0.25 (0)	0.125	0.125
Ti	-	0 (0.125)	0.125	0.125
Cr	-	-	0.0625	0.125
Mo	-	-	-	0.0625

Table 4.4: Bond probabilities of in (Al)(Ti)CrMo along and outside a b-displaced fault plane. Black values denote the probability outside the fault plane. Colored values denote the probability in the fault plane. The blue values denote an increase compared to the value outside the fault plane, and the red values denote a decrease.

	Al	Ti	Cr	Mo
Al	0 (0.125)	0.25 (0)	0.25 (0)	0 (0.25)
Ti	-	0 (0.125)	0 (0.25)	0.25 (0)
Cr	-	-	0 (0.125)	0.25 (0)
Mo	-	-	-	0 (0.125)

Table 4.5: Bond probabilities of in (AlMo)(CrTi) along and outside a b-displaced fault plane. Black values denote the probability outside the fault plane. Colored values denote the probability in the fault plane. The blue values denote an increase compared to the value outside the fault, and the red values denote a decrease.

contrast, the bond share of energetically unfavorable bonds is increased by $\frac{1}{8}$. Thus, the Broken Bond Model predicts a positive SAPBE. The presented model assumes a perfect mixture, which is expected for an infinitely large (or large enough) fault plane. However, if fault planes of finite-sized SQS or sub-parts of fault planes in the real crystal are considered, chemical fluctuations will influence the bond probabilities. Hence, the model is generalized to capture chemical fluctuations by introducing variable bond probabilities. The resulting equation yields

$$E_{\mathrm{B2}}^{\mathrm{SAPB}} = \frac{2\sqrt{2}}{a_0^2} \left[p_{\mathrm{AlAl}} W_{\mathrm{AlAl}} - p_{\mathrm{AlTi}} W_{\mathrm{AlTi}} + p_{\mathrm{ex}} W_{\mathrm{ex}} \right] . \tag{4.20}$$

In the next section, ground state energies from DFT-calculations of nb-displaced lattice structures are used to validate the presented model and to investigate the influence of partial B2-type order on the GSFE.

4.4.2.2 Influence of crystallographic ordering on GSFE from nb-displacements

This section presents stacking fault energies resulting from integer multiples of b displacements. Here, the Burgers vector b is defined as the shortest lattice invariance corresponding to the disordered lattice, i.e., $b = \frac{1}{2}\langle 111 \rangle$.

For the calculation, the ATAT toolkit[51] has generated three differently ordered SQS with atomic dimensions $8 \times 4 \times 8$. While one SQS represents the disordered AlCrMoTi, the second one represents the B2-type ordered (Al)(Ti)CrMo, and the third one represents the B2-type ordered (AlMo)(CrTi). The supercells have been oriented in a way that the x, y, and z-axes are parallel to the $\langle 111 \rangle$, $\langle 110 \rangle$, and $\langle 112 \rangle$-directions. During the calculation, the supercells are displaced in the x-direction by discrete displacements $d = 1b,\ 2b,\ \dots,\ 8b$. The displaced structures are relaxed with respect to atomic positions, with no restriction on the spatial degrees of freedom. The calculations have been performed for each supercell three times considering three different $\{110\}$-fault planes.

E1-E4 denote the planes corresponding to the three different faults since every fault can be unambiguously defined by a lower and upper border plane (e.g., E1-E2). The resulting total energies are then used to calculate GSFE by

$$\gamma(nb) = (E_0(0) - E_0(nb))/A, \tag{4.21}$$

with the area of the fault plane A.

In the following, in some cases, it will be differentiated between energies corresponding to even displacements ($n = 0, 2, 4, \dots$), which will be denoted by γ^{e} and energies corresponding to uneven displacements, which will be denoted by γ^{u}. Note that in the case of partially B2-type ordered structures, γ^{u} is equivalent to the shear antiphase boundary energy (SAPBE).

Figure 4.19 shows and compares the resulting $\gamma(nb)$ from disordered AlCrMoTi and partially B2-type ordered structures (Al)(Ti)CrMo and (AlMo)(CrTi). The data analysis reveals significant differences between the energy profiles of the three differently ordered structures. In the case of disordered AlCrMoTi, the energies corresponding to all three faults carry out random fluctuations, and no difference

between values from even or uneven displacements is visible. This observation is expected since disordered BCC structures have $1b$ as the shortest translation invariant. Hence, energy fluctuations are due to chemical fluctuations within the finite-size SQS, and there is no influence from the different displacement types.
The situation changes if a partial B2-type order is introduced into the SQS. The $\gamma(nb)$-values of faults E1-E2 and E2-E3 from (Al)(Ti)CrMo show a $2b$-periodicity. The $2b$-periodicity is consistent with the Broken Bond Model. However, the fact that mostly $\gamma^u < \gamma^e$ is counter-intuitive. The energy signature, which evolves from different displacements along the fault E3-E4, shows an entirely different signature from E1-E2 and E2-E3. Here, displacements $n = 0 - 3$ reveal the expected $2b$-periodicity with a positive γ^u, but further displacements $n > 3$ reveal $\gamma(n)$ with comparable small random fluctuations.
The GSFE signature calculated with the SQS representing partially ordered (AlMo)(CrTi) shows the expected $2b$-periodicity with $\gamma^u > \gamma^e$ for the faults E2-E3 and E3-E4. In contrast, the GSFE signature resulting from fault E1-E2 shows a $2b$-periodicity with $\gamma^u < \gamma^e$ for the first six displacements. A detailed analysis of the different $\gamma(nb)$-values reveals that γ^u-values from partially ordered structures are broader distributed compared to γ^e-values. The standard deviations of the γ-values are analyzed for quantitative analysis.
Figure 4.20 compares the standard deviations σ_γ, $\sigma_{\gamma^\mathrm{e}}$, $\sigma_{\gamma^\mathrm{u}}$ from disordered and both partially ordered SQS considering all displacements as well as only even and only uneven displacements. Inspection of this graph suggests that energies resulting from displacements of ordered structures have a standard deviation, which is sensitive to whether an even or uneven displacement has been applied. The observed sensitivity contrasts the insensitivity of standard deviations from energies calculated for the disordered structure. The data further reveal that $\sigma_{\gamma^\mathrm{u}}$ corresponding to ordered SQS is reduced compared to σ_γ corresponding to disordered SQS, while $\sigma_{\gamma^\mathrm{e}}$ is increased. The reduced $\sigma_{\gamma^\mathrm{u}}$ can be attributed to decreased chemical fluctuations between the displaced structures due to the decreased configuration space of ordered structures.
However, one might ask why the influence of chemical fluctuations on GSFE resulting from uneven displacements is increased for chemical-ordered structures. A possible explanation for this observation is that another more substantial effect

superimposes the effect of the decreased configuration space. A possible effect could be increased sensitivity of the otherwise ordered structure along the fault to chemical fluctuations.

In order to reveal further insights into the reasons for the different γ- and σ_γ-profiles of differently ordered AlCrMoTi, the following study analyses the distinct elemental concentrations of the fault planes. It discusses the influence of different elemental concentrations on the γ-profiles in the context of the Broken Bond Model.

Figure 4.21 presents the elemental concentration distributions of different fault planes of differently B2-type ordered SQS. The left bars denote superlattice SL1 containing all Al-atoms, and the right bars superlattice SL2 containing all Ti-atoms. The labels on the x-axis (E1, E2, ...) indicate the specific plane.

In the case of the used SQS representing the (Al)(Ti)-ordered structure, the data show an excess ($> 50\%$ per superlattice) of Al-atoms in all considered fault planes (E1-E4) and a depletion of Ti in fault planes E1-E3. The fault plane E4 has, in contrast to E1-E3, a pronounced excess of Ti-atoms (75% per superlattice). These observations, combined with the findings of Section 3.1.1 and the Broken Bond Model are consistent with the observations from the GSFE-calculations corresponding to the (Al)(Ti)-ordered SQS. The Broken Bond Model postulates that the energy differences between even and uneven displaced structures result from the change of direct neighbor bonds. In the case of (Al)(Ti)CrMo, the Al-Ti bond probability is transformed to Al-Al and Ti-Ti bond probabilities

$$p_{\text{Al-Ti}} \rightarrow p_{\text{Al-Al}} + p_{\text{Ti-Ti}}. \tag{4.22}$$

Section 3.1.1 already has indicated that Al-Ti and Al-Al bonds offer an energetical advantage compared to all other bond combinations. Hence, the observation of smaller SAPBE resulting from GSFE calculations involving the fault planes E1, E2, and E3 compared to the calculation involving E4 can be attributed to the following fact: In faults E1-E2 and E2-E3, the ratio between Al-Ti bonds in the even displaced structures and Al-Al bonds in the uneven displaced structures is lower than in the fault E3-E4. The observation of negative SAPBEs within the faults E1-E2 and E2-E3 further indicates $W_{\text{AlAl}} < W_{\text{AlTi}} < W_{\text{TiTi}}$. The negative

SAPBE could also explain the observation $\sigma_{\gamma^{\mathrm{u}}} > \sigma_{\gamma^{\mathrm{e}}}$, since with respect to p_{AlTi} a depletion of Al-atoms can be balanced by enrichment of Ti-atoms (and vice versa). However, with respect to p_{AlAl} and p_{TiTi}, a depletion of Al-atoms and an enrichment of Ti-atoms (or vice versa) leads to an imbalance between p_{AlAl} and p_{TiTi}. An imbalance between p_{AlAl} and p_{TiTi} causes situations where the SAPBE (see Equation (4.20)) is either reduced by the high content of Al-Al bonds or not. Consequently, the distribution width of SAPBE is broader than that of energies corresponding to supercells sheared by even multiples of b.

The results corresponding to (AlMo)(CrTi) did not reveal a similar connection between the γ-profils and the atom concentrations of the fault panes. The lacking connection is attributed to the fact that the bond probability changes from even to uneven displacements are more complex in this lattice configuration (see Tabular 4.5 vs. 4.4). Due to the high complexity, a detailed analysis of the exact bond shares and the corresponding GSFE values of the single displacement steps, e.g., a machine learning approach, could reveal further insights.

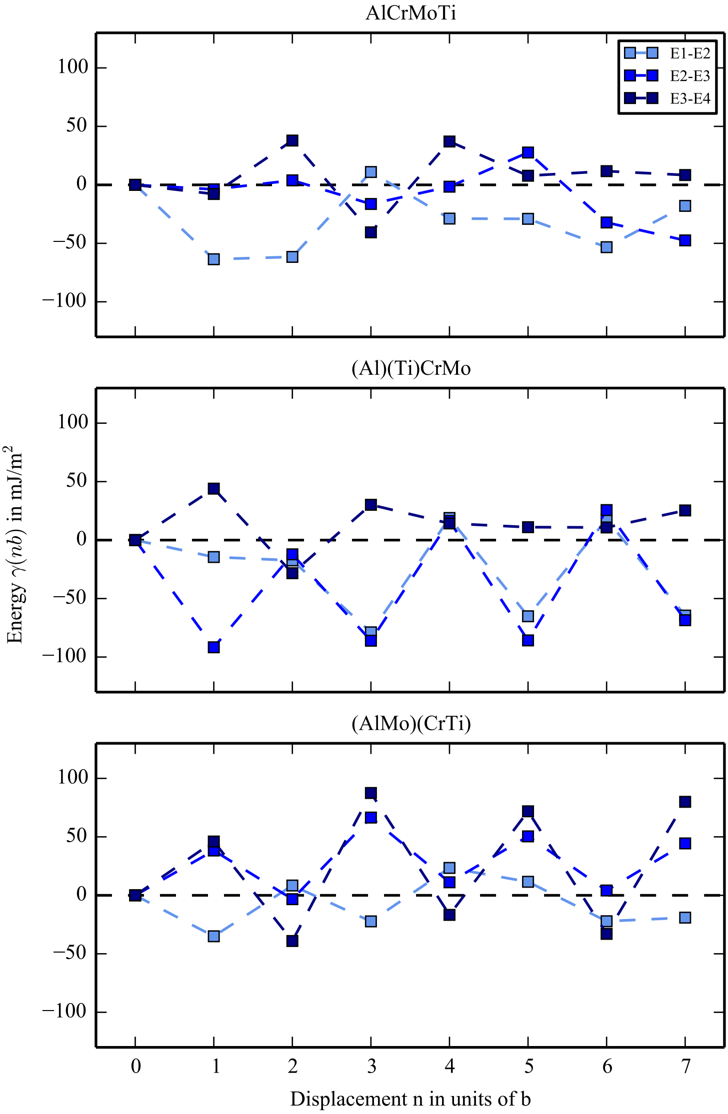

Figure 4.19: Stable stacking fault energies (SFE) of disordered, (Al)(Ti) and (AlMo) B2-type ordered AlCrMoTi. Different blue bars are due to different (110)-fault-planes. The black line denotes the average over all SFE, the red line denotes the average over all SFE at displacements of (nb) with $n = 1, 3, 5, 7$, and the green line denotes the average over all SFE with displacements (nb) with $n = 2, 4, 6$.

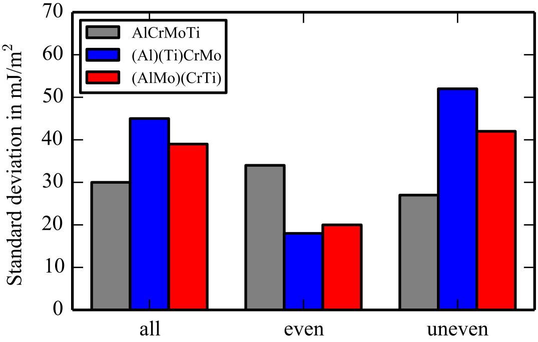

Figure 4.20: Standard deviations of $\gamma(n)$ values.

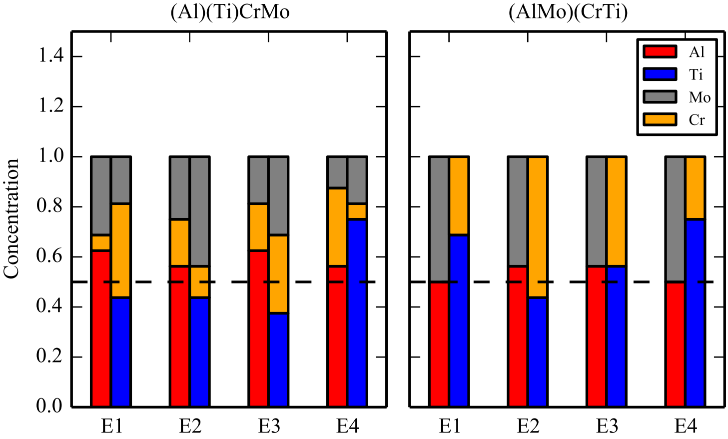

Figure 4.21: Elemental concentration distributions of superlattices SL1 (left bar) and SL2 (right bar) within upper and lower fault planes.

4.4.2.3 GSFE of partially ordered AlCrMoTi

This section investigates whether the method described in Section 2.5 can generate GSFE-functions, which can approximate the GSFE of partially ordered AlCrMoTi.

DFT-calculations have been used to determine the necessary parameters a, b, c to parametrize a sinusoidal GSFE-function of a $2b$-periodic structure according to Figure 4.22. Parameter a equals the unstable stacking fault energy γ_u. Parameter c is equivalent to the stable stacking fault energy γ_s, which is, in this case, equivalent to the shear antiphase boundary energy. For the DFT calculations in this section, the same setup as for the DFT calculations of previously presented GSFE results have been used. The calculated parameters are listed in Table 4.6 and the generated sinusoidal functions (defined in Section 2.5.2) are displayed and compared to the DFT-calculated discrete GSFE-values in Figures 4.24 and 4.23. Inspection reveals that the sinusoidal function well approximates the DFT data. The standard deviation indicated by the shaded area describes the influence of

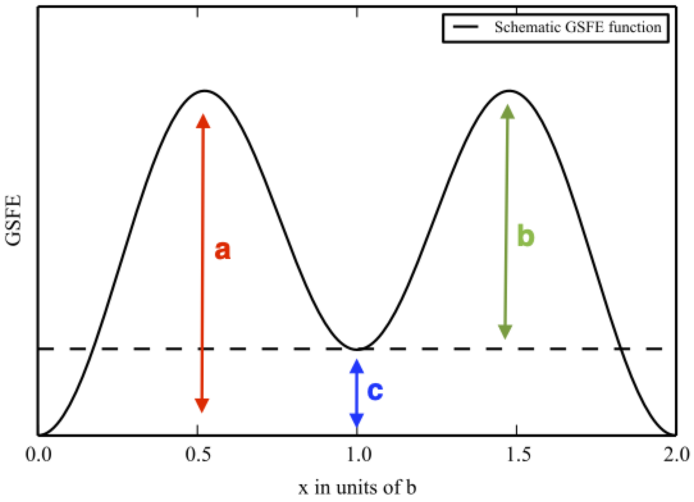

Figure 4.22: Schematic picture of $2b$ periodic GSFE-function.

]

spatial composition fluctuations changing the local chemical environment. From the observation that all parameters a,b, and c have standard deviations of comparable magnitudes, one can conclude that chemical fluctuations cause fluctuations of these parameters.

	a $[\mathrm{mJm}^{-2}]$		b $[\mathrm{mJm}^{-2}]$		c $[\mathrm{mJm}^{-2}]$	
	val	min/max	val	min/max	val	min/max
A2	717 ± 74	571/857	-	-	-	-
(Al)(Ti)	718 ± 45	637/786	759 ± 40	694/839	-42 ± 40	-111/72
(AlMo)	780 ± 52	662/856	740 ± 54	676/885	41 ± 53	-46/127

Table 4.6: DFT-calculated quantities for characterization of $2b$-periodic GSFE-function.

The results indicate a nonlinear relation between the degree of order and the APBE. The mean APBE decreases from 0 to -42 mJm^{-2} from the disordered- to the (Al)(Ti)-ordered lattice and increases from -42 to 41 mJm^{-2} from the (Al)(Ti)- to the (AlMo)-ordered lattice. The nonlinear relation seems to be, at first sight, contradicting the results of[78], which established a linear relationship between the degree of chemical short-range order in CoCrNi and its mean intrinsic stacking fault energy. The disruption of chemical favourable bonds along the fault plane rationalizes the linear relation between the degree of order and the mean intrinsic stacking fault energy, which is consistent with the basic assumption of the Broken Bond Model[78]. Hence, the previous section's findings can resolve the apparent contradiction, where it has been shown that the energetic advantage of Al-Al bonds causes the decreased mean APBE within the (Al)(Ti)CrMo-ordered structure.

The observation that the mean unstable stacking fault of the (AlMo)(CrTi)-ordered structure $\overline{\gamma}_u^{(\mathrm{AlMo})}$ is increased compared to the values from the disordered and (Al)(Ti)-ordered structure can be attributed to the increased mean stable stacking fault of (AlMo)(CrTi).

The standard deviation of the parameter a indicates an increased distribution of γ_u in disordered AlCrMoTi, which can be rationalized by the increased configuration space of the disordered lattice compared to a (partially) ordered lattice.

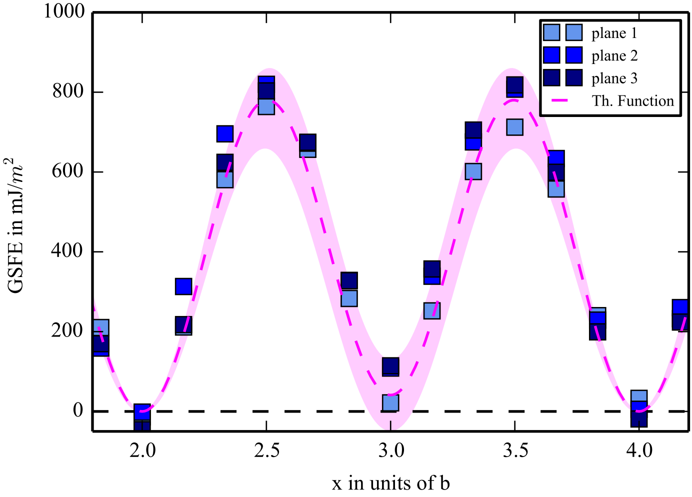

Figure 4.23: DFT GSFE-values of (AlMo)(CrTi) and theoretical fit function.

In summary, the order in the AlCrMoTi lattice influences the GSFE by changing periodicity from $1b$ to $2b$. Further, the order influences the unstable stacking fault energy's mean value and standard deviation. The influence of this changed GSFE on the deformation behavior will be discussed later in this work.

4.4.3 GSFE maximum slope of AlCrMoTi and HfNbTiZr

This section investigates the maximum slope F_{max}

$$\tau_{\text{id}}(x) = \frac{\partial\gamma(x)}{\partial x}, \tag{4.23}$$

and the ideal shear strength as the corresponding maximum value

$$\tau_{\text{max}} = \max\left(\tau_{\text{id}}(x)\right). \tag{4.24}$$

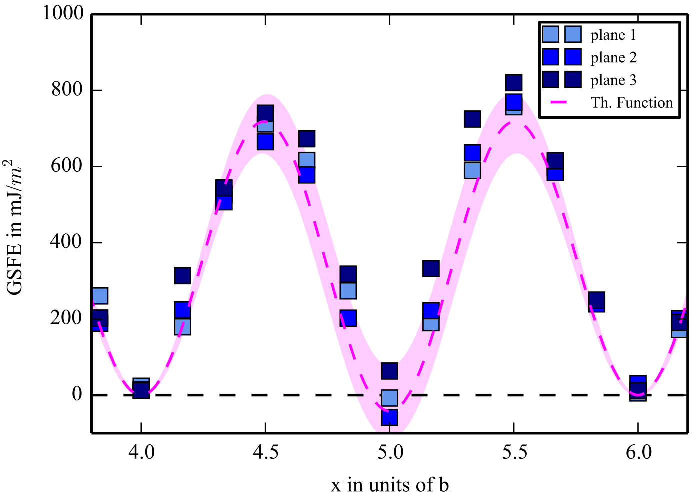

Figure 4.24: DFT GSFE-values of (Al)(Ti)CrMo and theoretical fit function.

of AlCrMoTi and HfNbTiZr. F_{max} is often used as a place-in for the Peierls stress, which denotes the stress necessary to move a dislocation[39]. A recent study showed that regions within the crystal matrix, which have increased F_{max}, serve as dislocation pinning points and can thus influence strength and ductility through decreased dislocation mobility[39]. F_{max} denotes a theoretical shear limit and is larger than the stress necessary to move a straight dislocation (Peierls Stress). In a monoatomic metal, τ_{max} only depends on the shear direction but is elsewhere a constant value[12].

In HEA, the situation is different since chemical fluctuations lead to fluctuations of the GSFE and, consequently, to fluctuations of the ideal shear strength (see Figure 4.23).

Figure 4.26 compares F_{max} of AlCrMoTi and HfNbTiZr with pure metals Nb, W. A comparison of the presented data with ideal shear strength corresponding to BCC metals from[77] reveals that the mean value of AlCrMoTi ($\tau_{\text{max}} = 7.3\text{GPa}$) is comparable to the one of Nb ($\tau_{\text{max}} = 7.5\text{GPa}$) and significantly lower as the one of W ($\tau_{\text{max}} = 20.1\text{GPa}$).

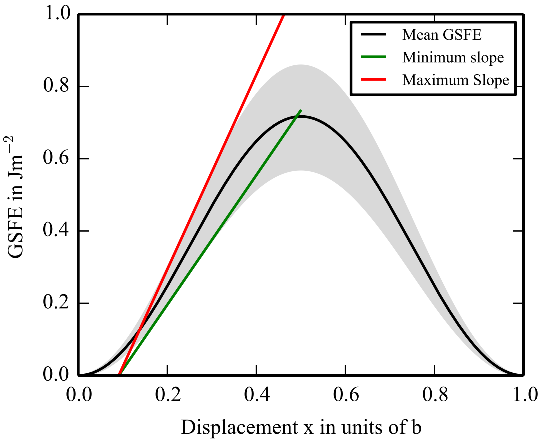

Figure 4.25: GSFE curve of HfNbTiZr and slope corresponding to the maximum shear stress.

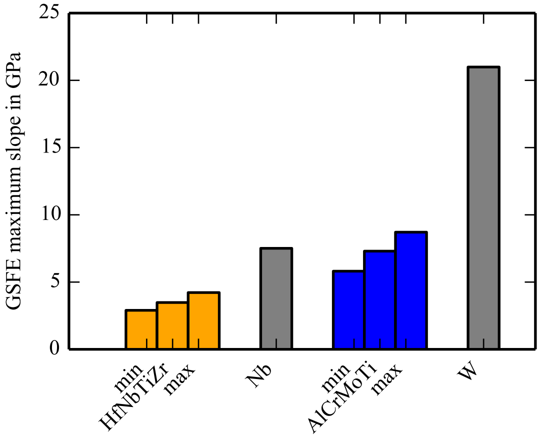

Figure 4.26: GSFE maximum slope of AlCrMoTi and HfNbTiZr compared to the one of Nb and W. Influence of chemical fluctuations taken into account by minimum and maximum values.

HfNbTiZr has a mean $F_{\max} = 3.48$ GPa, which is only half of the lowest values of pure BCC metals (Nb, V, and Ta posses $F_{\max} \approx 7$ GPa).

	$\tau_{\max1}$ [GPa]			$\tau_{\max2}$ [GPa]		
	val	min/max	Δ/val	val	min/max	Δ/val
A2	7.30	5.81/8.71	40%	-	-	-
(Al)(Ti)	7.36	6.37/8.16	24%	7.66	5.85/8.96	40%
(AlMo)	7.87	6.55/8.77	28%	7.57	5.63/9.1	46%

Table 4.7: GSFE maximum slope in GPa disordered and ordered of AlCrMoTi.

An evaluation of the minimum and maximum observed F_{max} indicates an increased influence of chemical fluctuations in AlCrMoTi compared to HfNbTiZr since the difference between the minimum and maximum values are 2.9 GPa (40% of F_{max}) for AlCrMoTi and 1.3 GPa (37% of F_{max}) for HfNbTiZr. Note that the presented trends follow the trends of the GSFE results since F_{max} are directly determined from the GSFE.

Table 4.7 and Figure 4.27 illustrate the influence of B2-type chemical order in AlCrMoTi on the ideal shear strength. The mean F_{max} increases only slightly with increasing degree of order, while the distribution width decreases with increasing degree of order. Note that this observation is consistent with the findings in[79]. Here, the dislocation core energy distribution width in MoNbTaW decreases with an increasing degree of chemical short-range order. At the same time, the mean values are insensitive to the degree of order.

We assume that the sample size in this study is too small to reveal exact values of the distribution width. GSFE calculations have been performed only on three different glide planes per lattice structure. Due to the nature of GSFE, the influence of chemical fluctuations is highest in values resulting from different glide planes. Hence, involving more glide planes and convergence studies would be necessary to reveal exact values corresponding to the distribution width. Hence, the analysis in this work is constrained to state qualitative trends between different HEA compositions instead of quantitative findings.

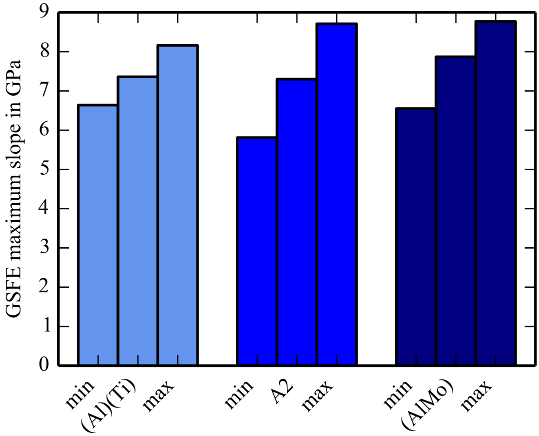

Figure 4.27: Comparison between ideal shear stress of ordered and disordered AlCrMoTi. Minimum and maximum values due to chemical fluctuations.

4.4.4 Conclusions

DFT-calculations revealed discrete GSFE-values from three fault planes, each of chemically disordered HfNbTiZr and AlCrMoTi as well as of partially B2-type ordered (Al)(Ti)CrMo and (AlMo)(CrTi). A detailed analysis of the calculated values led to the following conclusions:

- AlCrMoTi has an unstable stacking fault energy $\gamma_\mathrm{u} = 717\mathrm{mJ/m^2}$, which is in the same range as BCC elemental metals Nb, Ta, and V.
- HfNbTiZr has an unstable stacking fault energy $\gamma_\mathrm{u} = 396\mathrm{mJ/m^2}$, which is low compared to γ_u of AlCrMoTi and γ_u of elemental BCC metals.
- The unstable stacking fault energy γ_u has a higher standard deviation in AlCrMoTi as in HfNbTiZr ($74\mathrm{mJ/m^2}$ vs. $30\mathrm{mJ/m^2}$). The higher standard deviation in AlCrMoTi indicates an increased sensitivity of γ_u in AlCrMoTi on the specific atomic arrangement.

- B2-type order in AlCrMoTi changes the periodicity of the γ-function from $1b$ to $2b$. Within the investigated ordered structures, the shear antiphase boundary energies (SAPBE) show more fluctuations as energies resulting from supercells displaced by even multiples of b. The Broken Bond Model can explain this observation with the changed bond probabilities within the fault plane, which causes an increased sensitivity of the energy of the total system on chemical fluctuations along the fault plane.

5 Discussion on possible deformation mechanisms

This chapter evaluates different models describing dislocation mobility and deformation in BCC HEA. For this, it uses the DFT results from the previous chapter as input parameters for the different models.
The first section uses elastic constant results to evaluate the line tension model. It compares the dislocation line energy and tension of different BCC HEA and discusses its implications on the deformation mechanisms. The second section uses GSFE results to evaluate a recent energy landscape model[39]. The third section evaluates the kink pair nucleation model. Here the elastic line energies from the first section are used as input parameters. The chapter will show that the kink pair model's implications are inconsistent with experiments. However, the revealed single kink energies are necessary input parameters for solid solution strengthening theories, which are evaluated in the last section.

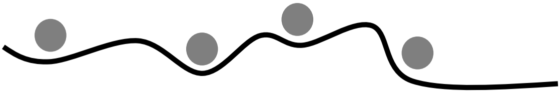

Figure 5.1: Schematic plot of a bowed dislocation line due to obstacles.

5.1 Line Tension Model

This section uses the material property results presented earlier in this work, i.e., the lattice constant and the elastic constants, to derive the elastic line energy and line tension. The elastic line energy and tension denote a dislocation energy per unit length. While the line energy neglects the distinct line morphology (straight or bowed), the dislocation line tension takes the case of a bowed dislocation into account.

The elastic line energy and tension will be interpreted within the line tension model, described in dislocation theory textbooks[12,13,20]. The basic idea of line tension is to describe situations where the dislocation line increases its energy due to an increase in length and a change of its orientation. For example, the dislocation line faces obstacles like precipitates or solutes (see Figure 5.1). The dislocation line has to bend itself around them to avoid the obstacles. This process leads, on the one hand, to an increase in line length and, on the other hand, to a location-dependent change in the line orientation. The local change of line orientation causes an overall change in the ratio between the screw and edge dislocation parts. An increase in line length increases the system energy, while the orientation change can increase or reduce the energy. The total energy increase causes a backstress, which reduces the dislocation mobility. The dislocation line tension, for example, can be used as input quantity for the Orowan mechanism, which describes the reduction of dislocation mobility through second phase particles[12,13,20]. In addition, a recently presented solid solution strengthening model is based on the idea of edge dislocations bowing around energetically unfavorable chemical environments[36].

Note that the line tension model can also describe situations where line length and orientation change without being influenced by other crystal defects. Within homogeneous nucleation, the line tension describes the energy contribution due to an increasing circular dislocation[13]. The Peierls Nabarro model uses the dislocation line energy to balance the energy contribution resulting from the Peierls potential[15,80]. Further, the dislocation line tension is an input parameter for a model, which describes the critical stress of Frank Read source activations[77].

The dislocation line energy and line tension are defined within the elastic continuum and explained in detail in dislocation theory books[20,12,13]. Nevertheless, the following briefly introduces the concept. Introducing an infinitely long straight dislocation in an otherwise perfect crystal leads to a distortion of the crystal lattice around the dislocation. The distortions lead to a strain and stress field of the dislocation. Integrating the stress field over volume leads to the isotropic elastic energy of a dislocation per unit length L

$$E_{\text{el}}(\theta) = \frac{Gb^2}{4\pi L}\left(\cos^2(\theta) + \frac{\sin^2(\theta)}{(1-\nu)}\right)\ln\frac{R}{r_0}, \tag{5.1}$$

with shear modulus G, Burgers vector b, Poisson ratio ν, and the angle between the dislocation line and Burgers vector[12,13,20]. The parameters R and r_0 denote the cutoff parameters of the elastic field. The inner cutoff r_0 is due to the incapability of linear elastic theory to describe the large distortions around the dislocation center. The area that can not be captured by linear elasticity is called the dislocation core area and must be treated separately with nonlinear theories[12,13,20]. The distinction between linear and nonlinear areas leads to a decomposition of the dislocation energy into an elastic, and a core term

$$E_{\text{disl}} = E_{\text{el}} + E_{\text{core}}. \tag{5.2}$$

Usually, the core part of the energy is incorporated into the logarithm by

$$E_{\text{disl}} = K(\theta)\ln\frac{\alpha R}{r_0}, \tag{5.3}$$

with core energy $E_{\text{core}} = \ln\alpha$ and the prelogarithmic factor $K(\theta)$[12,13,20].

Within the anisotropic elastic theory, the prelogarithmic factor is calculated with

the Stroh theory[81], which means solving a linear equation system involving the lattice constant and the elastic constants of the considered material.
The dislocation line tension is based on the dislocation line energy and can be imagined in the following way: Applying external stress leads to a bow out of the dislocation line, which increases the dislocation line length and, therefore, its line energy. The increase in energy leads to back stress against external stress. Consequently, the dislocation line has a line tension like a rubber band. Taking into account that bowing out the line leads not only to an increase in length but also to a change in θ, the line tension $T(\theta)$ is calculated including a curvature term $\left(\frac{\partial^2 K(\theta)}{\partial\theta^2}\right) \ln\frac{R}{r_0}$. Hence, the line tension is described by the equation

$$\begin{aligned} T(\theta) = E_{\text{el}} + \frac{\partial E_{\text{el}}}{\partial\theta} &= \left(K(\theta) + \frac{\partial^2 K(\theta)}{\partial\theta^2}\right) \ln\frac{R}{r_0} \\ &= B(\theta) \ln\frac{R}{r_0}, \end{aligned}$$

with the prelogarithmic factor of the dislocation line tension $B(\theta)$[12,13,20].
The following section presents and discusses the prelogarithmic K and B-factors.

5.1.1 Prelogarithmic factor K of dislocation line energy of BCC HEA

This section presents and discusses prelogarithmic factor K results corresponding to different BCC HEA. The results, including elastic anisotropy, have been generated using Stroh theory with lattice constants and elastic constants of different BCC HEA calculated by DFT calculations. The used input quantities have been presented and discussed earlier in this work. The presented values have been calculated for each case by isotropic and anisotropic theory.
Figure 5.2 compares the prelogarithmic factors corresponding to screw $K(0)$ and edge dislocations $K(\pi/2)$ of different BCC metals and HEA.
The presented data show that $K(0) < K(\pi/2)$. Within the isotropic theory, this relation can be attributed to the factor $1/(1-\nu)$ since it holds $\nu < 1$ for all tested

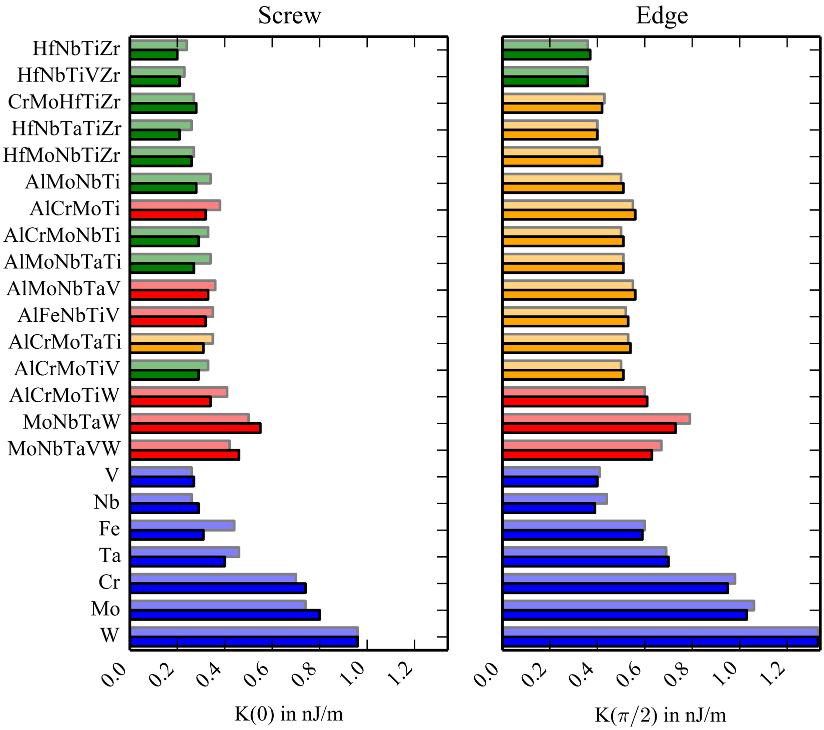

Figure 5.2: BCC elemental metals and HEA prelogarithmic factors of a screw (left graph) and edge (right graph) dislocation line energy. Green bars denote values below the one of Nb, orange bars denote values between Nb and Fe, and red bars denote values above the one of Fe. Brighter (more transparent) bars correspond to values from isotropic and non-transparent bars to values of anisotropic theory.

metals and alloys. Within the anisotropic theory, the mathematical expression of the relation between $K(0)$ and $K(\pi/2)$ is more complex than within the isotropic theory. However, in this work, a mathematical expression is not derived since the data reveal no influence on the general qualitative trend of the K-values by using an anisotropic theory instead of the isotropic one. Consequently, in the following, it will not be differentiated between values from isotropic and anisotropic elasticity.

The K-values corresponding to the tested BCC HEA are small compared to the K-values of BCC metals. The maximum value of $K(0)$ found for HEA is $0.55\mathrm{nJ/m}$ (MoNbTaW), while the one found for BCC metals is $0.96\mathrm{nJ/m}$ (W). Several HEA have $K(0)$-values below the one of Nb, with V the BCC metal with the lowest line energy. The rest of the investigated alloys show $K(0)$-values between Nb and Fe or slightly above the one of Fe.

Generally, the difference between the lowest and highest $K(0)$ of all investigated HEA is small (0.2-0.55 $\mathrm{nJ/m}$) compared to the difference between the lowest and highest $K(0)$ of elemental metals (0.27-0.96 $\mathrm{nJ/m}$).

The same trend holds for $K(\pi/2)$. Here the values corresponding to BCC metals vary between 0.4 and 1.33 $\mathrm{nJ/m}$, while the values corresponding to BCC HEA vary between 0.36 and 0.73 $\mathrm{nJ/m}$. Most values of BCC HEA lay between Nb and Fe. Only a few $K(\pi/2)$-values of HEA are below the one of Nb and above the one of Fe.

This observation is consistent with Vegard's law. Vegard's law is approximately valid for the lattice constant and the elastic constants (see Section 4.2.1). The results indicate that its validity is transferable to the line energy. Consequently, the resulting K-values of the considered BCC HEA are concentrated around a mean value resulting from the different values of the contributing elements. In order to design a BCC HEA with an exceptionally high K, one would have to leave the equimolar composition and create a material with a high content of, e.g., W atoms. On the other hand, to create a material with an exceptionally low K, one would have to design a material with high shares of, e.g., Nb or even better with high shares of non-BCC elements like Al or Hf showing comparable low shear moduli.

In order to discuss the presented dislocation line energies, one can formulate the working hypothesis that a low dislocation line energy enhances dislocation mobility due to the low energetical costs of dislocation generation and elongation. The hypothesis is consistent with experimental results in the case of BCC metals since V, Nb, Fe, and Ta are found to be room temperature ductile, while Cr, Mo, and W are room temperature brittle [82,83,84,85,86].

Based on the assumption that screw dislocations dominate the plastic deformation in BCC metals [20,12,14], the findings in [87] are consistent with the stated hypothesis. The study revealed a correlation between the K-factor and the Peierls potential, which describes the internal friction felt by the dislocation moving from one Peierls valley to the neighboring valley [87]. Hence, a low K factor reduces the potential energy barrier created by the crystal lattice felt by screw dislocations [87]. Comparing the K-factors corresponding to screw dislocations of different BCC HEA yields a consistent picture with experimental results. For example, Figure 5.2 shows that the K-values of HfNbTiZr and HfNbTaTiZr are extraordinarily low, which is interesting because experiments showed that HfNbTaTiZr and HfNbTiZr RT ductile [4,8]. On the other hand, the K-values of AlCrMoTi and AlCrMoNbTi are above the ones of HfNbTiZr and HfNbTatTiZr, and both alloys have shown to be RT brittle [5]. However, a comparison between the $K(0)$ of BCC metals and HEA reveals that the calculated values of all tested BCC HEA are comparable to the $K(0)$ of V, Nb, Fe, and Ta. Hence, good room temperature ductility of all tested BCC HEA would be expected. However, this is different from experimental results since, besides the BCC HEA from the Al-CrMo-Nb-Ta-Ti system, MoNbaTaVW already showed RT brittleness [69].

Generally, the low differences between the K-factors of the considered HEA and the different experimentally observed room temperature ductility are inconsistent with the assumption of a correlation between the dislocation mobility and the K-factor.

Figure 5.2 shows that $K(0)$ and $K(\pi/2)$ share the same trends. Hence, the $K(\pi/2)$ are not discussed separately. Moreover, edge dislocations are considered not to influence the RT ductility through their enhanced mobility in BCC metals. The limited ductility in BCC metals is associated with the reduced mobility of screw dislocations [12]. However, recent studies showed that in the particular case of random alloys, edge dislocations could play an important role in plastic deformation[36,33,34].

Recently, a solid solution strengthening model was proposed, where edge dislocations control plasticity in random BCC alloys[36]. In this model, the edge dislocation line tension $\sim B(\pi/2)$ plays an important role. This model will be discussed later in this work.

Considering the K-factor or the dislocation line energy alone is problematic. Although the K- and B-factors are input parameters for several dislocation mobility models, they are usually accompanied by other input parameters like the dislocation solute interaction energy. The dislocation solute interaction energy describes the interaction between the dislocation line and the random crystal matrix[36,35,48]. Models considering only the dislocation line energy completely neglect effects evolving from chemical fluctuations.

Thus, this work will initially assess the line tension of dislocations followed by a detailed analysis of advanced solid-solution strengthening models of HEA in the context of the AlCrMoTi and HfNbTiZr HEA.

5.1.2 Prelogarithmic factor B of dislocation line tension of BCC HEA

This section presents and discusses the prelogarithmic factor of dislocation line tension $B(\theta)$ corresponding to different BCC HEA. The results have been generated using Stroh theory[81] with lattice constants and elastic constants of different BCC HEA calculated by DFT calculations (see Section 4.2). The presented values have been calculated by isotropic and anisotropic theory.

Figure 5.3 compares the prelogarithmic factor $B(\theta)$ of different BCC HEA with elemental BCC metals.

In contrast to the K-factor one can observe for the B-factor the relationship $B(0) > B(\pi/2)$. In the line tension model $B(0) > B(\pi/2)$ can be attributed to the curvature term $\left(\frac{\partial^2 K(\theta)}{\partial\theta^2}\right) \ln \frac{R}{r_0}$, which positive for $\theta = 0$ and negative for $\theta = \pi/2$.

The elastic anisotropy affects $B(0)$ more as $B(\theta/2)$, $K(0)$ and $K(\theta/2)$, which

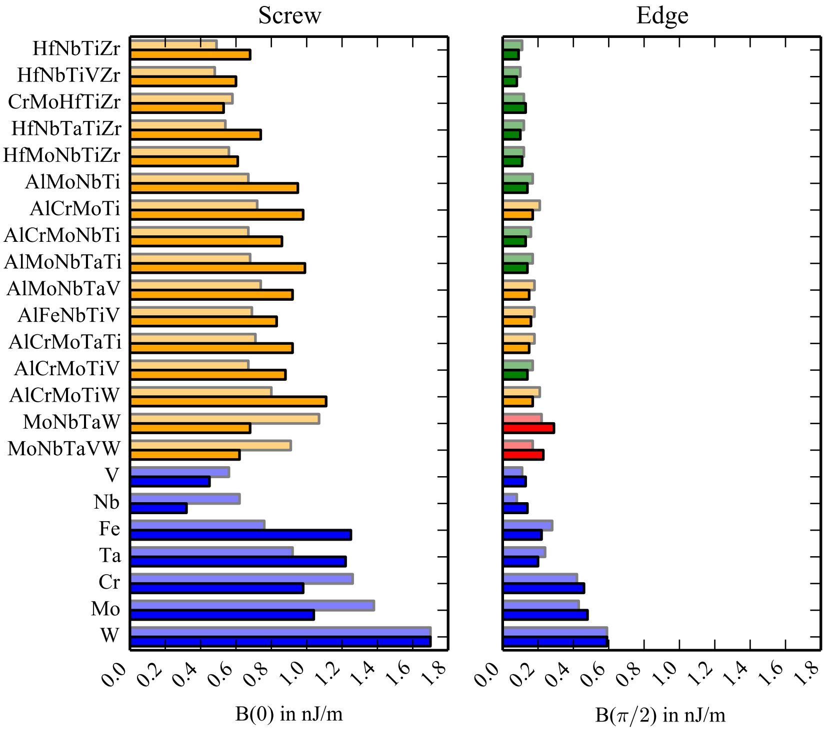

Figure 5.3: BCC elemental metals and HEA prelogarithmic factors of a screw (left graph) and edge (right graph) dislocation line tension. Green bars denote values below Nb, orange bars denote values between Nb and Fe, and red bars denote values above the one of Fe. Brighter (more transparent) bars correspond to values from isotropic and darker (non-transparent) bars to values of anisotropic theory.

can be attributed to the curvature term since the curvature around $\theta = 0$ is more sensitive than the one for $\theta > 0$. This analysis suggests the need to include elastic anisotropy for calculating screw dislocation properties like $B(0)$, which has been done in the following analysis.

Figure 5.3 demonstrates that for edge dislocations with $\theta = 0$, all tested HEA have values between Nb and Fe between 0.6$\mathrm{nJ/m}$ (HfNbTiVZr) and 1.11$\mathrm{nJ/m}$ (AlCrMoTiW). The values corresponding to BCC metals are broader distributed, with the lowest value 0.45$\mathrm{nJ/m}$ (Nb) and the highest value 1.7 $\mathrm{nJ/m}$ (W).

For screw dislocations with $\theta = \pi/2$, the tested BCC HEA have B-factors between 0.08$\mathrm{nJ/m}$ (HfNbTiVZr) and 0.29$\mathrm{nJ/m}$. The values corresponding to BCC metals are generally higher and broader, distributed between 0.13 and 0.59 $\mathrm{nJ/m}$. Thus, BCC HEA show no extraordinary low or high line tension values compared to BCC metals. Experiments revealed RT ductility for HfNbTiZr[8] and RT brittleness for MoNbTaW[69]. However, this work predicts similar $B(0)$ values for both alloys. Hence, this work reveals no direct correlation between RT ductility and $B(0)$.

In the case of edge dislocations ($\theta = \pi/2$), the data reveal extraordinarily low B-values for a group of Hf containing HEA, medium B-values for Al-containing alloys and comparable high B-values for MoNbTaW and MoNbTaWV. Hence, a correlation exists between $B(\theta/2)$ and the RT ductility for edge dislocations. Alloys with low $B(\theta/2)$ (HfNbTiZr, HfNbTiVZr, and HfNbTaTiZr) have shown to be RT ductile[68,8,4]. Alloys with higher $B(\theta/2)$(AlCrMoTi,MoNbTaW and MoNbTaW), have shown to be RT brittle[9,10,69].

This correlation is consistent with the edge dislocation solid solution strengthening model, where edge dislocations are more dominant than screw dislocations in controlling the plastic behavior in BCC HEA[36]. In this theory, edge dislocations interact with the crystal matrix, occupied randomly by different atoms. The dislocation line adopts a wavy structure to avoid energetically unfavorable environments. Low line tension enhances the ability to generate this wavy structure. However, the edge dislocation line tension is one of many vital parameters within the edge dislocation solid solution strengthening model. Thus, the model is discussed later by taking other results from this work into account (see Section 5.4.1).

The following section investigates the effect of the proposed ordering on the prelogarithmic factor of dislocation line energy and tension.

5.1.3 Influence of B2-type ordering on elastic line energy and tension in AlCrMoTi

This section treats the influence of B2-type ordering on the elastic line energy and tension. The results have been generated using Stroh theory[81] with lattice constants and elastic constants of different BCC HEA calculated by DFT calculations. The quantities used were presented and discussed earlier in Section 4.2.1. Figure 5.4 shows that B2-type ordering influences the elastic line energy and tension. The graph shows that the most decisive impact is on the screw dislocation line tension, which is increased in the ordered lattice structures. The increased line tension of screw dislocations in ordered AlCrMoTi is attributed to the increased elastic anisotropy of the ordered structures (see Section 4.2.2), which leads to an orientation-dependent line energy at $\theta = 0$. Introducing a B2-type ordering decreases the elastic dislocation line energy and edge dislocation line tension, but the ordering affects the screw dislocation line tension less.

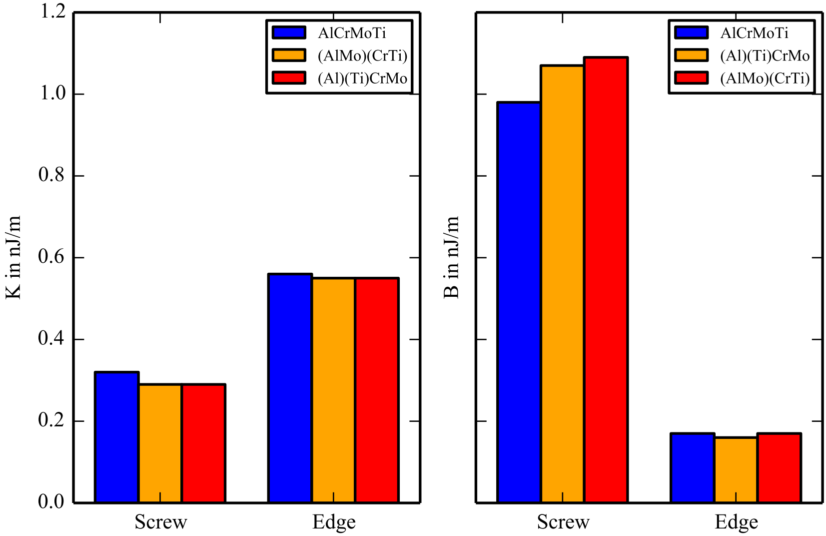

Figure 5.4: Left: Elastic line energy of AlCrMoTi, (Al)(Ti)CrMo and (AlMo)(CrTi). Right: Elastic line tension of AlCrMoTi, (Al)(Ti)CrMo and (AlMo)(CrTi).

In summary, the data show that crystallographic ordering influences the line energy and tension less than the chemical composition. Hence, crystallographic ordering has a minor influence on the elastic contributions of the dislocation energy. However, one should be careful to conclude that chemical order does not influence mechanical properties.
Structural approaches like GSFE revealed more pronounced differences between chemically ordered and disordered AlCrMoTi (Section 2.5). These results can be interpreted within an energy landscape approach (Section 5.2).

5.1.4 Conclusions

This section investigated and discussed the prelogarithmic factor of the dislocation line energy and tension.

- All tested HEA have prelogarithmic factors of dislocation line energy and line tension with values comparable to the ones of V, Nb, Fe, and Ta. V, Nb, Fe, and Ta are among BCC metals, the ones with comparable low values.
- The differences between the K- and B-values corresponding to the different tested BCC HEA are small compared to the differences corresponding to different BCC metals. This observation can be attributed to the rule of mixtures, which is valid for the lattice constant and the elastic constants (Section 4.2.1). Thus, the calculated prelogarithmic factors are close to the theoretical average values corresponding to the different contributing elements of the individual alloys.
- The comparable low K- and B-factors do not correlate with the different RT ductility, which has been experimentally found in different BCC HEA.
- The influence of crystallographic ordering is low compared to the influence of the chemical composition.

5.2 Dislocation motion through complex energy landscape

This section considers the discrete lattice structure of crystals by introducing the Peierls potential, which models the effect of the lattice periodicity. Considering the discrete lattice structure contrasts the elastic dislocation field approach in the previous Section 5.1. The Peierls potential describes the energy barrier felt by dislocations between equilibrium positions generated by the discrete lattice [15,80]. The Peierls-Nabarro Model describes the displacement potential of a dislocation, which involves the linear elastic line energy and the nonlinear core contribution. For the nonlinear contribution, analytical functions can be used, which can be generated either by involving the elastic shear modulus or by fitting the periodic function on results from atomistic simulations, e.g., the gamma surface.

Although the Peierls-Nabarro model gives an elegant description of the dislocation core, it cannot describe the nonplanar cores of screw dislocations in BCC crystals [12,20,13]. Previous investigations have revealed that the nonplanar core plays a crucial role in the deformation behavior of BCC metals since it leads to temperature-dependent plasticity at low temperatures controlled by kink pair nucleation [20,14].

Due to the crucial role of the dislocation core properties and the strongly connected Peierls potential, this section discusses generalized stacking fault energies (GSFE) of the BCC HEA AlCrMoTi, and HfNbTiZr revealed by DFT-calculations as an approximation for the Peierls-Energy.

A combined experimental and MD-simulation study already performed a similar analysis, which showed that in FCC CoCrNi, chemical fluctuations lead to fluctuations in the GSFE [39]. These fluctuations influence dislocation mobility by pinning the dislocation line at regions with high stacking fault energy. Consequently, dislocation mobility correlates with the density and magnitude of pinning points [39]. The combined experimental and MD-simulation study further revealed that dislocation mobility in CoCrNi is independent of the degree of chemical short-range order (CSRO).

The independence of dislocation mobility and chemical short-range order contradicts MD simulations where increasing the degree of CSRO decreases the dislocation mobility[88]. The decreased dislocation mobility is speculated to be attributed to the need to break energetically favorable bonds during glide and to increased anti-phase boundary energy.

Note that an increased degree of CSRO increases the density of pinning points due to increased fluctuations of the GSFE. It also decreases the fluctuations of misfit volumes within the crystal matrix[76]. Decreasing fluctuations of misfit volumes enhance dislocation mobility according to solid solution strengthening theories[48].

All these findings from different studies illustrate the necessity of considering crystallographic ordering since it can influence the GSFE and other material and dislocation properties. The possibility of controlling the stable stacking fault energy (SFE) in FCC CrCoNi by the degree of CSRO has already been shown[78]. In CrCoNi, SFE values range from negative to positive depending on the degree of CSRO[78]. The appearance of negative SFEs is often connected to desirable material properties like high strength and ductility[89]. However, while there are for FCC HEA, several studies investigating the GSFE and its cross connections to CRSO and dislocation mobility[39,76,78,88,89,90], for BCC HEA, such studies are rare.

However, unstable stacking fault energies (USFE) have been used as input parameters for the Rice model[91,92,93] to predict the ductility of several BCC HEA. Within the Rice model, low USFEs increase the material ductility via dislocation nucleation enhancement at the crack tip[91,92,93].

Further, DFT calculations have been used to investigate the influence of CSRO on the core energies of BCC HEA MoNbTaW[79]. However, a detailed study of the implications of GSFE on dislocation mobility and the influence of crystallographic ordering needs to be included. Consequently, this section considers the GSFE results from Section 4.4 as an approximation for a variable Peierls potential and discusses the implications on the deformation behavior.

5.2.1 Energy landscape of chemically disordered AlCrMoTi and HfNbTiZr

This section interprets the generalized stacking fault energy (GSFE) results corresponding to AlCrMoTi and HfNbTiZr from Section 4.4 in the context of an energy landscape, which is experienced by a dislocation.

This work has already shown that due to the rule of mixtures, most BCC HEA have low to average shear moduli compared to BCC metals. The dislocation line energy and line tension depend linearly on the shear modulus. The dislocation line energy, the Peierls potential height, and the single kink energy appear to be linearly correlated [87]. Since low Peierls potential barriers and single kink energies are supposed to enhance dislocation mobility, the question arises about the origin of the exceptional high strengths, which have been experimentally measured for these materials [5,4,8]. Furthermore, since chemical fluctuations are one of the critical differences between HEA and metals, the reduction of dislocation mobility through fluctuations in the energy landscape caused by chemical fluctuations could be a possible explanation.

In CrCoNi, a combined experimental and MD investigation observed dislocation pinning at points with increased γ_{usf} [39]. The study further showed that the material strength increases with such pinning points' increased density and strength. Section 2.5 showed and discussed fluctuations in GSFE (and their slope) for HfNbTiZr and AlCrMoTi. Their comparable high yield strengths are thus consistent with CoCrTi observations [39] that fluctuations of the GSFE can reduce dislocation mobility. Quantitative analysis and comparison between both alloys are not possible by considering the GSFE alone. Therefore, one has to derive a mechanism-based model, including GSFE. However, since increasing strength and density of pinning points decrease dislocation mobility [39], the RT ductility of HfNbTiZr [8] and the RT brittleness of AlCrMoTi [5] might be connected to their specific GSFE features. γ_{usf} and $\sigma_{\gamma_{\mathrm{usf}}}$ are both higher in AlCrMoTi as in HfNbTiZr. Further, the observed γ_{usf} of HfNbTiZr is not only low compared to AlCrMoTi, but it is also low compared to BCC metals (see Section 2.5).

The alternative idea is that the excellent ductility of HfNbTiZr [8] is connected to an increased ability to nucleate dislocations at the crack tip. The Rice model [91,92] predicts an increased ability to nucleate dislocations at the crack tip for decreased unstable stacking fault energies. The connection between unstable stacking fault energies γ_{usf} and ductility has already been discussed for several BCC HEA[93]. However, it is still being determined if the crack tip response can be extrapolated to the plastic behavior of bulk samples.

In summary, random GSFE fluctuations are a signature property of random alloys like HEA since they result from the random crystal matrix of such alloys. Hence, they are likely connected to their signature properties like high yield strength. However, there exist other material parameters resulting from the random crystal matrix, which might be correlated with the GSFE fluctuations. The exact correlations with each other and the implications on the mechanical properties are still to be determined. For example, in solid solution strengthening theories describing dislocation mobility of screw- and edge dislocations in BCC HEA[35,36], the dislocation energy landscape plays a key role. However, the crucial parameter in these theories is not the fluctuation of GSFE, but the fluctuation of dislocation matrix interactions. MD simulations indicated that dislocation matrix interactions and GSFE correlate[37].

This work will also discuss recent solid solution strengthening theories with DFT input parameter (from this work) in Section 5.4.

5.2.2 Energy landscape of crystallographic ordered AlCrMoTi

This section discusses the influence of crystallographic ordering on the energy landscape of AlCrMoTi and its implications on the deformation behavior. Following[39], the GSFE approximate the energy landscape a dislocation core samples by gliding through the crystal. The considered GSFE results have been presented and discussed in Section 2.5.

The GSFE results presented in this work revealed that the distribution width of unstable stacking fault energies is more sensitive to chemical ordering than the corresponding mean values. As discussed in the previous paragraph, instead of the absolute γ_{usf} values, the fluctuations of γ_{usf} are the signature property of random alloys and thus a strong candidate to explain their high strengths compared to BCC metals. The decreasing distribution width of γ_{usf} with increasing degree of chemical ordering in AlCrMoTi thus suggests that the appearance of chemical ordering reduces the dislocation pinning probability and hence improves dislocation mobility.

However, introducing a chemical (partial) order does not only influence the unstable stacking fault energy. It influences the stable stacking fault energies at multiples of b (Section 4.4.2). Consequently, it is crucial to consider stable stacking fault energies for partially ordered HEA like AlCrMoTi.

The results presented in Section 4.4.2 revealed a broad spectrum of stable stacking fault energies γ_{s}-values, reaching from negative to positive values in chemically ordered (Al)(Ti)CrMo and (AlMo)(CrTi). In order to get some insights into the implications of stable stacking fault energies on macroscopic mechanical properties, the results are now discussed in the context of the experimental findings[94].

The influence of chemical order on the temperature and strain-dependent flow stress in B2-ordered FeCo has been investigated by different degrees of order in FeCo ranging from completely chemically disordered to completely chemically ordered. They found cross slip as the dominating deformation mechanism for the disordered sample and a temperature dependent flow stress[94].

Several mechanisms can explain their observations: Kink-pair nucleation[21] or mechanisms from solid solution strengthening models[35] predict a temperature-sensitive yield strength for BCC crystals. However, kink pair nucleation theory is in contrast to the solid solution strengthening theory, not able to involve apriori chemical fluctuations of the crystal matrix.

B2-ordered FeCo samples showed three deformation mechanisms dependent on strain[94]. At minimal strains, the stress and temperature dependency are reduced compared to the stress in disordered samples.

The stress reduction can be connected to a reduced dislocation pinning through the crystal matrix. This explanation is consistent with the findings in Section 4.4.2.3, which predict decreasing fluctuations of the unstable stacking fault energy with increasing chemical ordering.

Moreover, the reduced yield stress in ordered BCC alloys increases ductility. However, in the case of B2-ordered FeCo, the opposite is observed[94] due to rapid strain hardening at larger strains within ordered samples. Furthermore, strain hardening is attributed to a reduced ability of screw dislocations to perform cross slip because cross slip corresponds to a displacement of b and is only possible by the cost of creating an APB[94]. Moreover, the conservative movement of jogs along the dislocation line is hindered within ordered alloys since this is only possible by creating additional APB[94]. Since the costs of creating an APB cannot be accommodated by thermal energy, the deformation in this stage is not temperature dependent[94].

In partially ordered alloys, an additional stress contribution could evolve from the hindered cross-slip ability that forces the dislocation to sample energetically unfavorable chemical environments, increasing dislocation pinning.

In summary, the discussed additional stress contributions could explain the room temperature brittleness of partially ordered alloys, like AlCrMoTi, by hypothesizing that the additional stress contributions lead to stress concentrations, which eventually cause a brittle fracture. Thus, the room temperature brittleness of AlCrMoTi could be rationalized by a positive mean APBE.

However, the above discussion is only valid for positive APBE, but the GSFE results indicate negative APBE in (Al)(Ti)-ordered AlCrMoTi (Section 4.4.2). Negative stacking fault energies implicate that leading dislocations produce APB consisting of energetically favorable bonds. Dislocations need to break these bonds during glide and thus overcome a back-stress. Hence, the APB serve as dislocation pinning points.

Furthermore, negative APB are stable and have bond distributions different from the remaining crystal matrix. The evolving differences in atomic mean distances and differences in elastic properties introduce stress fields, which interact with dislocations and hence introduce further stress contributions.

In summary, the appearance of non-zero APBE created by crystallographic ordering can change the controlling deformation mechanisms compared to completely disordered alloys. As a result, non-zero APBE can reduce dislocation mobility. The reduced dislocation mobility is consistent with the observed RT brittleness of partially ordered AlCrMoTi[5,9].

In the case of AlCrMoTi, ductility increases by reducing the Al-content[10]. Since an order-disorder transition appears at a certain Al-concentration, the increased ductility can be attributed to the suppression of the ordered phase[10]. However, the ductility of disordered and Al-reduced AlCrMoTi was enhanced but still poor[10]. The existence of energetically favorable bonds in AlCrMoTi can explain the poor RT ductility since energetically favorable bonds can serve as strong pinning points to the dislocation line and could rationalize reduced dislocation mobility.

Section 3.1 already showed that energetically favorable Al-Al and Al-Ti bonds cause crystallographic ordering in AlCrMoTi. Al-Al and Al-Ti bonds exist in ordered and disordered AlCrMoTi, albeit in different concentrations. Hence, chemical ordering may be only a side effect, not the reason for room temperature brittleness. In other words, the reduced dislocation mobility through the strong pinning points affects the mobility and therefore induces quasi-brittle deformation. This perspective suggests that the reduction of the Al-concentration causes an order-disorder phase transition and a reduction of energetically favorable Al-Al and Al-Ti bonds in AlCrMoTi (and chemically similar alloys, e.g., AlCrMoNbTi). Both effects can enhance dislocation mobility. Consequently, the GSFE results (Section 2.5) and the free energy results (Section 3.1) are consistent with experimental findings for AlCrMoTi alloys.

5.2.3 Conclusions

This section discussed the GSFE results of BCC HEA HfNbTiZr, and AlCrMoTi presented in Section 2.5 in the context of an energy landscape model[39].

- The energy landscape model, combined with the observed GSFE fluctuations in AlCrMoTi and HfNbTiZr, predicts reduced dislocation mobility through dislocation pinning. The reduced dislocation mobility is consistent with the experimentally observed high yield strength of these alloys[5,8].

- The observed stable stacking fault energies in partially ordered configurations of AlCrMoTi could explain its high yield strength and room temperature brittleness through a decreased dislocation mobility caused by the creation of ABP.

- Experiments showed that ductility in Al$_x$CrMoTi is enhanced after Al-reduction reduces crystallographic order. Pinning points through energetically favorable Al-Al and Al-Ti bonds can explain the poor ductility of disordered Al$_x$CrMoTi.

5.3 Thermally activated plasticity of BCC HEA

This section discusses the thermally activated plasticity of BCC HEA. In BCC metals and conventional BCC alloys, thermally activated plasticity is based on the fact that screw dislocations in BCC metals and alloys have a nonplanar core configuration[12,13,14,20]. The nonplanar core configuration introduces an energy barrier against dislocation glide, i.e., the Peierls potential[15].

Kink pair nucleation theory predicts that the activation barrier for dislocation glide can be reduced by kink pair nucleation. Consequently, the flow stress σ can be decomposed into an effective flow stress σ^* needed to maintain the required rate of kink pair nucleation and an athermal flow stress σ_{ath}[22]

$$\sigma = \sigma^* + \sigma_{\mathrm{ath}}. \tag{5.4}$$

The effective flow stress depends on temperature and strain rate, while the athermal flow stress is independent of the strain rate and only weakly dependent on temperature[22].

There are two models to calculate the kink pair formation energy. The line tension model is used for high stresses and low temperatures, where the separation q of the two kinks is small, and the self-interaction of a curved dislocation dominates the kink-kink interaction[22]. The elastic interaction model is used for smaller stresses and higher temperatures, where the separation q of the two kinks is large, and the kink-kink interaction is dominated by the long-range elastic interaction $-a^2B/2q$[22]. The elastic interaction can be used to calculate the enthalpy in saddle point configuration, which denotes the activation energy for kink pair nucleation

$$H_k^{\mathrm{EI}}(\sigma^*) = 2E_k - 2\alpha\sigma^{*1/2}, \tag{5.5}$$

with the energy of an isolated single kink E_k and $\alpha = (a^3bB/2)^{1/2}$[22]. Using the general equation for thermally activated processes[13,12]

$$H = k_BT \ln \frac{\dot{\epsilon}_0}{\dot{\epsilon}} \tag{5.6}$$

with Boltzmann constant k_B, the activation energy H_k can be connected with macroscopic quantities temperature T and effective flow stress σ^* by[22]

$$\dot{\epsilon} = \dot{\epsilon}_0 \exp\left(\frac{H_k^{\mathrm{EI}}}{k_B T}\right). \tag{5.7}$$

The transition temperature between the kink pair nucleation regime and the athermal regime is reached when there is enough thermal energy to generate a double kink without further stress contribution $H_k^{\mathrm{EI}}(\sigma^* = 0)$. The transition temperature is called knee temperature T_K and can be calculated combining Equation 5.5 and Equation 5.7

$$T_K = \frac{2E_k}{k_B \ln(\dot{\epsilon}_0/\dot{\epsilon})} \tag{5.8}$$

Experimental flow stress measurements show that thermally activated plasticity in pure BCC metals is consistent with predictions from kink pair nucleation (see[22] for Nb,[23] for Fe,[26] for Ta,[25] for Mo and[24] for W).

At this point, the question arises whether BCC metals and BCC HEA show the same temperature-dependent deformation mechanisms. Various experiments show similarities between BCC metals and several BCC HEA. For example, TEM investigations observed long straight screw dislocations after plastic deformation in HfNbTaTiZr. The measured activation volumes in HfNbTaTiZr are of the same magnitude as observed for BCC metals[6,7,27]. Further, temperature-dependent flow stress measurements and nano indentation experiments indicate that the flow stress-temperature trend in several BCC HEA is similar to conventional BCC metals and alloys[5,10,32,95].

Figure 5.5 compares the flow stress for different temperatures of BCC Nb and BCC CrMoTaTi. The flow stresses of Nb and CrMoTaTi are both strongly temperature dependent at low temperatures and have a thermal-athermal transition at higher temperature.

However, the same experiments found larger thermal and athermal yield stress components in BCC HEA compared to pure BCC metals and conventional BCC alloys[32]. Moreover, experiments indicate that edge dislocations are decisive in plastic deformation for at least some BCC HEA[33,34]. These findings led

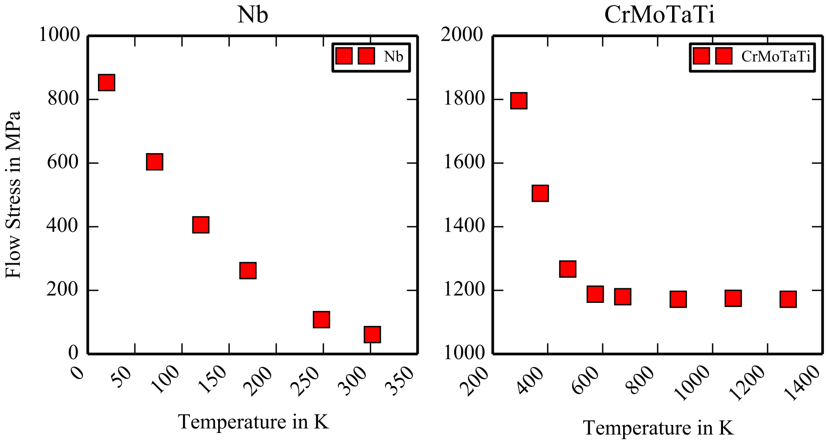

Figure 5.5: Experimentally flow stress of BCC Nb and BCC CrMoTaTi measured by compression tests [32].

to new solid solution-strengthening (SSS) theories, specifically for BCC HEA, concentrating on screw dislocations [37,35,32] or edge dislocations [36].

Within the Maresca-Curtin (MC-I) model [35] (discussed in Section 5.4.2), the appearance of kinks and their interaction with the random crystal matrix play a decisive role, and the single kink energy E_k is a crucial input parameter. However, the calculation of E_k is challenging. In [35], Molecular Dynamics (MD) simulations with interatomic potentials from the embedded atom method (EAM) are used. This work presents an alternative method to calculate E_k of BCC HEA using DFT calculations combined with Small Set of Ordered Structures (SSOS). The presented method combines the excellent chemical accuracy of DFT calculations and the efficiency of the SSOS method.

The DFT calculated E_k serve as input parameters for the MC-I solid solution strengthening model in Section 5.4.2.

5.3.1 Effective prediction of single kink energies

This section uses material properties, calculated within this work, to effectively predict the single kink energy E_k of BCC materials. The presented model uses material quantities like elastic constants and lattice constants, which are accessible within the framework of this work. Furthermore, the model moves and unifies uncertainties like the dislocation core energy into one linear factor. The introduction of this linear factor opens the possibility of fitting experimental single kink energies of BCC metals on the applied model to derive the unknown factor.

The single kink energy denotes the stress-independent activation energy, which is necessary to form a kink pair ($H_{\mathrm{KP}}(\sigma^* = 0) = 2E_k$). In pure BCC metals, E_k is directly connected to the transition temperature between thermally activated and athermal plasticity via Equation 5.22.

Experimentally E_k can be determined by measuring the thermal-athermal transition temperature (i.e., the knee temperature T_K) to

$$\ln(\epsilon) = \ln \epsilon_0 - \frac{1}{T_{\mathrm{K}}} \cdot 2E_k. \tag{5.9}$$

Alternatively, one can directly calculate E_k with simulations by introducing a kink in an otherwise perfect crystal lattice and calculating the energy difference. However, such calculations are computationally expensive. Alternatively, one can use analytical approaches, which model E_k with fundamental material properties like elastic constants and the lattice constant. The line-on-substrate and elastic segment-wise models are analytical approaches.

The Eshelby model (or line-on-substrate model) describes a dislocation as a heavy line with a line tension, which creates a back force against bowing out[96]. In equilibrium, the line tension is balanced by the Peierls potential $E_p(y)$, a periodic function with maximum ΔE. The single kink energy is calculated by subtracting the energy of a straight dislocation line from that of a straight line containing one kink. Evaluating the integral along the path $y(x)$, which is determined by the equilibrium condition yields[14]

$$E_k = C_{\mathrm{p}} a_{hkl} \cdot \sqrt{B \Delta E}. \tag{5.10}$$

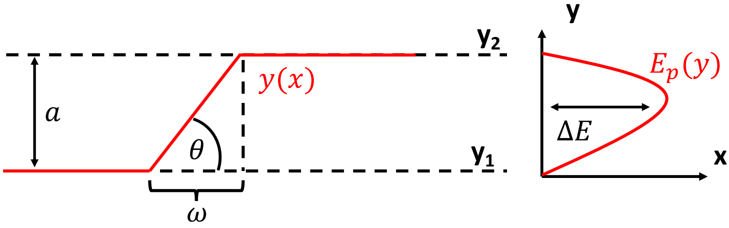

Figure 5.6: Schematic single kink configuration.

The factor C_p depends on the choice of the Peierls potential (e.g., sinusoidal, Eshelby, anti-parabolic) and varies between 0.90 and 1.11. Finally, the factor a_{hkl} defines the kink height, which depends on the chosen glide system. The dislocations are expected to glide in $\{110\}$ or $\{112\}$ glide planes in BCC materials. The corresponding kink heights are $a_{110} = \sqrt{2/3}a_0$ and $a_{112} = \sqrt{2}a_0$.
For the line tension, literature proposes to use the line energy $B \approx E_\mathrm{el} = K \cdot \ln\frac{R}{r_0}$ [14] or to include a curvature term $B = (K + \frac{d^2K}{d\theta^2})\ln\frac{R}{r_0}$ [21].
One can approximate the Peierls potential height ΔE as the maximum slope of the γ-surface (Section 4.4.3). Alternatively, one can directly calculate ΔE by inserting a dislocation in an otherwise perfect lattice, moving it from one Peierls Valley to the neighboring one, and measuring the energy[87]. DFT calculations yielded that the Peierls potential has a sinusoidal shape for BCC metals, with the height scaling with the prelogarithmic factor of the corresponding dislocation line energy[87].
Based on these findings, one can rewrite Equation (5.10) into

$$E_k = C_\mathrm{p} \cdot \sqrt{c_\mathrm{cor} \ln\frac{R}{r_0} a_{hkl} K}. \tag{5.11}$$

R and r_0 are the inner and outer cutoff radii of the single kink elastic field. Here, R is equal the kink width ω and propose values for $\ln\frac{R}{r_0}$ between 2.5 and 3.0[22]. Alternatively, literature proposes that R is either the kink width or the critical separation distance of two kinks, which denotes the transition from the line tension to the elastic interaction regime[14].

The critical distance between two single kinks, which separates the line tension from the elastic interaction regime, can be calculated by

$$\Delta x_c = \sqrt{\frac{aK}{2b\sigma^c}}, \tag{5.12}$$

where σ^c is the transition stress from line tension (LT) and elastic interaction (EI) regime[22]. Using experimental σ^c values provided by[22], one finds $\Delta x_c = 4-9b$ for BCC metals. Using an effective $r_0 = r_{\text{eff}} = 1b$, this yields $\ln\frac{R}{r_0} = 1.6 - 2.2$, which is slightly below the values proposed by[22].
Figure 5.7 compares the calculated E_k from Equation (5.10) for $a_{hkl} = a_{\{110\}}$ and $\ln\frac{R}{r_0} = 1.6$ with experimentally determined values (from Table 5.1). For the

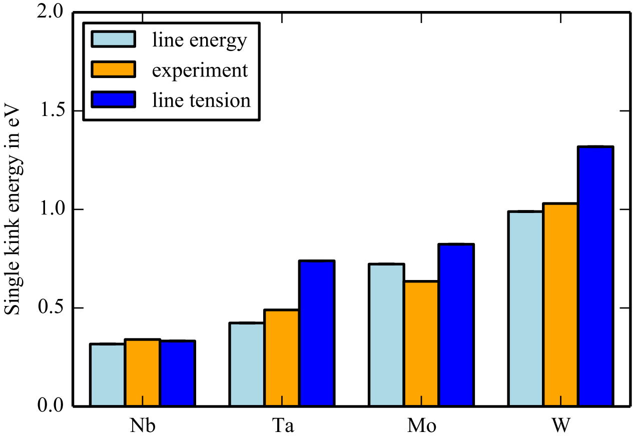

Figure 5.7: Single kink energy from theory calculated with dislocation line energy (light blue bars) and dislocation line tension (blue bars) compared to experimental singe kink energies[22,24,25,26,97] (orange bars).

Peierls potential height, the values from[87] have been used. The prelogarithmic factor B has been calculated one time as the anisotropic prelogarithmic factor of the screw dislocation line energy and another time as the prelogarithmic factor of the dislocation line tension. Figure 5.7 shows that both models capture the experimental trend qualitatively. One can see that the model predicts values more closely to the experiment if the line energy instead of the line tension is used as an input parameter. If one uses the line tension, the theoretical values overestimate the experimental values for Ta, Mo, and W.

Note that both approaches are approximations that stem from two opposing limits. Using the line energy means that the line tension contribution to the energy is modeled only by the increase in length of a pure screw dislocation. In contrast, in the real crystal, the line direction will vary between the pure screw and the pure edge direction.

Using the line tension, one considers the dislocation line a completely bowed-out line without any straight parts. This consideration leads to an overestimation of E_k, especially in the case of Ta. For Ta, the anisotropy factor is ≥ 1, which leads to a high curvature contribution $\frac{\partial^2 K}{\partial \theta^2}$.

Figure 5.8 allows a more detailed analysis of both approaches. The high correlation coefficients ($q \geq 0.97$) confirm that the predicted E_k are consistent with the experimentally measured values. The least-square fit yields a linear scaling factor of $c = 0.99$ for the approach using the line energy, which means no scaling is necessary.

For the line tension approach, the least-square fit yields a scaling factor of $c = 1.29$. Thus, the predicted values are overestimated, and an additional scaling factor of $1/1.29$ would be necessary to generate theoretical results consistent with the experimental values.

In literature exists another approach besides Equation (5.10) to calculate E_k [12].

Ref.	Material	$2H_\mathrm{k}$ [eV]	$\dot{\epsilon_0}$ [10^8 s $^{-1}$]
[22]	Nb	0.68	≈ 1.1
[97]	Fe	0.93	≈ 150
[26]	Ta	0.98	≈ 0.5
[25]	Mo	1.27	≈ 55
[24]	W	2.1	≈ 430

Table 5.1: Results from single kink energy measurements of different bcc metals.

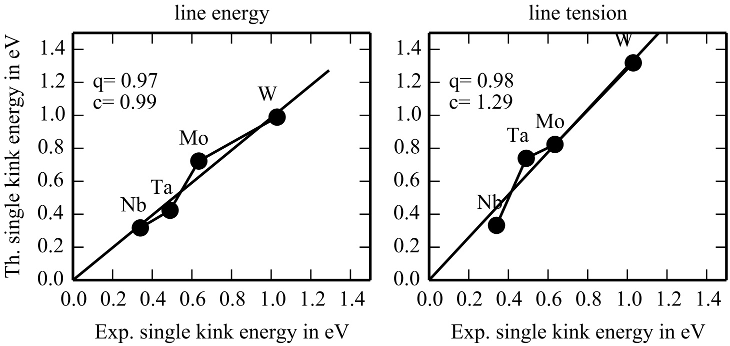

Figure 5.8: Linear correlation between experimentally measured and theoretically predicted single kink energies. The left graph shows theoretical results from the line energy, and the right graph shows theoretical results from the line tension approach.

The double kink energy is assumed to be a superposition of the self energies and the interaction energies of the individual segments (see Figure 5.9)

$$E_{\text{KP}} = \underbrace{2E_s(D) + 2E_{\text{int}}(C, A) - 2E_{\text{int}}(C', A)}_{2E_k} + \underbrace{E_{\text{int}}(D, E)}_{E_{\text{int}}} . \qquad (5.13)$$

The energies of the single segments and their interaction terms are modeled by

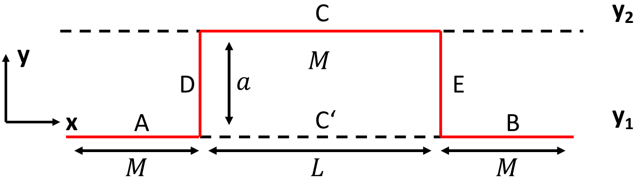

Figure 5.9: Double kink energy as the sum over single segments A, B, C, D, E minus straight configuration (A, B, C', D). Burgers vector and dislocation line direction point both in x-direction.

linear elasticity. The summation yields

$$E_{\mathrm{KP}} = \underbrace{2aK_e^{\mathrm{is}}\left(\ln\frac{a}{e\rho} - (1-\nu)\right)}_{2E_k} - \underbrace{\frac{a^2}{2L}B_s^{\mathrm{is}}}_{E_{\mathrm{int}}}, \tag{5.14}$$

with a self energy term $2E_k$ and an interaction term E_{int}. In this equation, a denotes the kink height, K_e^{is} the prelogarithmic factor of the edge dislocation line energy, e the Euler number, ρ a factor to model the cutoff corresponding to the elastic field, ν the Poisson ratio, distance L between two single kinks and B_s^{is} the prelogarithmic factor of the screw dislocation line tension. Note that the term for the interaction energy is valid for distances L large enough.

Consequently, Equation (5.14) describes the kink pair formation energy in the elastic interaction regime. One can extract the single kink energy from Equation (5.14) and write it in terms of prelogarithmic K-factors of screw and edge dislocations

$$E_k = a\left[K_e \ln\left(\frac{R}{r}\right) - K_s\right]. \tag{5.15}$$

In order to evaluate this equation, the same arguments hold for R/r as discussed in the previous section and $\ln(R/r) = 1.6$.

Figure 5.10 shows the resulting single kink energies compared to experimental values. The theoretical values have been calculated using isotropic and anisotropic K-factors. The data show that the model can reproduce the trend of the experimental values but strongly overestimates the single kink energies.

The linear correlation plot (Figure 5.11) shows that the theory overestimates the single kink energies by a factor ≈ 2.

A possible explanation for the overestimation is that the model assumes the kink is pure edge type. In contrast, the kink is expected to reduce its energy in the real crystal by adopting its shape to a minimum energy configuration. Another explanation for the overestimated energy is argued to be related to the abrupt change of the line direction leading to separation distances below b near the corner[12]. Consequently, the interaction is not elastic anymore. A smooth transition of the line direction is expected in a real crystal, and consequently, the *corner effect* has to

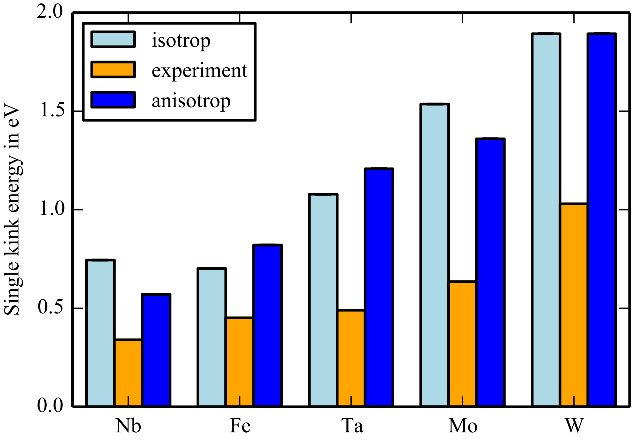

Figure 5.10: Theoretically predicted single kink energies E_k from line energy approach using prelogarithmic factors from isotropic and anisotropic elasticity compared to experimentally determined E_k [22,24,25,26,97].

be corrected by an additional term. According to [12], this correction term is of the order $\frac{\mu b^3}{4\pi}$, which is consistent with the observed overestimation by a factor ≈ 2. The transition between activation energy from $2E_k$ to E_k, found by analyzing populations of kinks on dislocation [84,98], could be an alternative explanation for the overestimation by factor 2. The transition from $2E_k$ to E_k happens when the length of a gliding dislocation segment exceeds a temperature-dependent critical length [84,98].

At this point, one can conclude that the single kink energies calculated by the elastic segment model correlate well with the experimentally measured values. The overestimation by factor two is consistent with the expected corner effect [12] and with recent dislocation mobility simulations [84,98]. The exact nature of the correction term and the logarithmic factor $\ln(R/r)$ introduce uncertainties in the

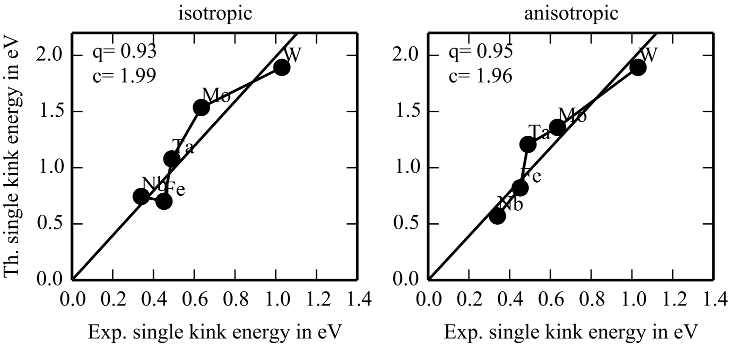

Figure 5.11: Linear correlation between experimentally measured and theoretically predicted single kink energies. The left graph shows theoretical results from the isotropic, and the right graph shows theoretical results from the anisotropic line energy approach.

model. However, one can define an effective model by adding the correction factor $\approx 1/2$, which yields

$$E_k = \frac{a}{2.9}\left[K_e \ln\left(\frac{R}{r}\right) - K_s\right]. \tag{5.16}$$

5.3.2 Effective scaling law for BCC single kink energies

This section introduces an approach for effectively predicting BCC single kink energies and compares it to previously presented models. The approach is based on the assumption that E_k can be decomposed into a line energy term and a correction term which summarizes the uncertainties like the exact shape of the single kink, core energy, energy corrections due to core transformations, and self-interaction of the dislocation line

$$E_k^{\text{sc}} = a_{hkl}\left[K \ln(R/r) + E_{\text{cor}}\right]. \tag{5.17}$$

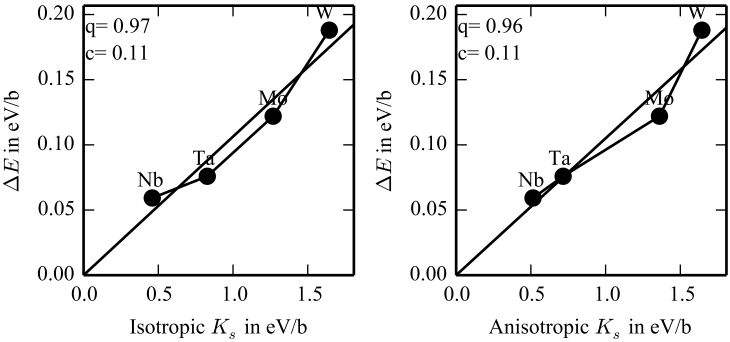

Figure 5.12: Correlation between K_s^{anis} and ΔE. The corresponding linear fit function yields $c_{\text{corr}} = 0.11$.

The approach assumes that the correction term scales with the prelogarithmic factor K, which allows summarising uncertainties, including the choice of the glide system in one factor

$$E_k = a_{hkl} K \left[\ln(R/r) + c_{\text{cor}}\right] \equiv C_{\text{sc}} \cdot K. \tag{5.18}$$

Equation (5.18) will be called scaling law in the following because it assumes that E_k linearly scales with the prelogarithmic factor K of the dislocation line energy of the considered material. Since the model is initially not restricted to a particular orientation of the dislocation line, the prelogarithmic K factor is not further specified at this point.

The presented scaling law can be motivated by the finding that the Peierls potential height scales with the prelogarithmic factor of the screw dislocation line energy $\Delta E = c_{\text{cor}} K_s$[87]. Since in the line on substrate model, the Peierls potential height scales by $\sqrt{\Delta E}$ with the single kink energy, the relationship can be used to rewrite Equation (5.10).

Figure 5.12 shows that the linear correlation is high ($q \geq 0.96$) for the isotropic and anisotropic K_s. Inserting this finding into Equation (5.10) reveals the same form as Equation (5.18) with K representing the prelogarithmic factor of the screw dislocation line energy.

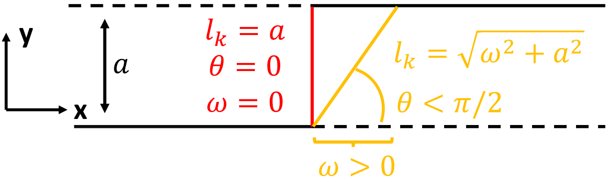

Figure 5.13: θ dependency of the increase of the dislocation line length by introducing a single kink. The increase of the total dislocation length is modeled by the difference between the kink length l_k and the corresponding kink width ω.

A detailed observation of the elastic segment model reveals that Equation (5.15) can also be rewritten as the scaling law by eliminating the K_s term. Consequently, the elastic segment model predicts a linear correlation of E_k and aK_e.
The question arises at this point whether $c_\mathrm{sc}aK_s$ or $c_\mathrm{sc}aK_e$ are more suitable descriptors for the single kink energies of BCC materials. For this discussion, one has to consider two aspects: First, the dislocation line is expected to increase its total length to minimize the elastic energy contribution. Therefore, the increase of the total line length ΔL (see Figure 5.13) can be calculated as the difference of the dislocation line length containing one kink $L + \Delta l_k$ and the length of the corresponding straight dislocation L:

$$\begin{aligned} \Delta L &= L + \Delta l_k - L \\ \Delta L &= l_k - \omega(\theta) \\ \Delta L &= \sqrt{a^2 + \omega(\theta)^2} - \omega(\theta), \end{aligned} \tag{5.19}$$

with the kink length l_k, the kink height a and the kink width ω. The angle θ can be introduced by the relation $\omega = \arctan\left(\frac{a}{\omega}\right)$. The equation shows that the total dislocation line length increase has a maximum for the pure edge case and decreases to zero with $\theta \to 0$. Naturally, small $\theta \approx 0$ should be preferable to reduce the increase of the elastic energy.

This effect is even more prominent, taking the screw-edge anisotropy into account. K has a maximum for $\theta = \pi/2$ and a minimum for $\theta = 0$. Note that the directional dependency is approximately introduced through the curvature term by using the line tension instead of the line energy to describe the elastic energy of a kink. Hence, kink structures with very small θ are energetically preferred to reduce the elastic energy.

However, the elastic energy is counterbalanced by the core energy. The increase of the core energy by introducing the kink in the otherwise straight dislocation is expected to scale with the kink length l_k since this part of the line has an increased core energy due to the Peierls potential. Consequently the increase in core energy should be minimal for $\theta = \pi/2$ (and $l_k = a$) and increase with decreasing θ (and $l_k = \sqrt{a^2 + \omega^2}$). To calculate E_k, the minimum energy path $y(x)$ needs to minimize the elastic line and core energy.

The two counteracting effects will lead to a x-depending θ varying between 0 and $\pi/2$. Since our approach assumes constant (average) θ, the question remains, which reference angle θ can accurately model the kink energy within the constant line energy/tension approach?

Figure 5.14 compares the linear correlation of different scaling law approaches using the isotropic and anisotropic prelogarithmic factors of the screw- and edge-dislocation line energy together with the prelogarithmic factor of the screw dislocation line tension.

Within isotropic elasticity, all investigated scaling laws are approximately equal good descriptors for E_k with high linear correlation $q \geq 0.95$. This observation is reasonable since the screw-edge anisotropy is reduced by the factor $1/(1-\nu)$, which varies for the considered BCC materials between 1.4 and 1.7. Hence, the factor $1/(1-\nu)$ can be approximated as a constant, and the scaling law can be reduced to $E_k = c_{\mathrm{sc}} a b^2 \mu$.

The high linear correlation of the isotropic approaches suggests that the neglection of elastic anisotropy is more an advantage than a disadvantage since it averages over the uncertainties connected with the unknown shape of the kink structures.

Considering elastic anisotropy improves the linear correlation of the scaling law from $q = 0.92$ to $q = 0.96$. This observation suggests that the scaling law predicts that kinks in BCC materials are more of an edge than of screw type. However, the

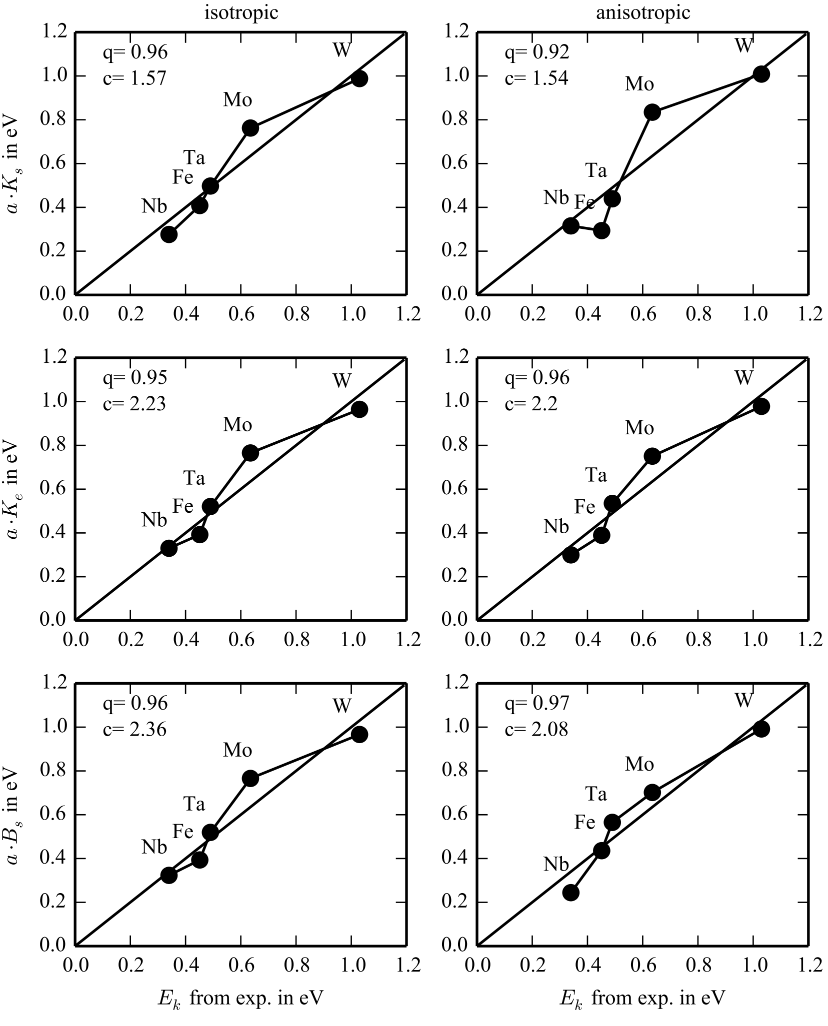

Figure 5.14: Correlation matrix between different models and single kink energies of BCC metals.

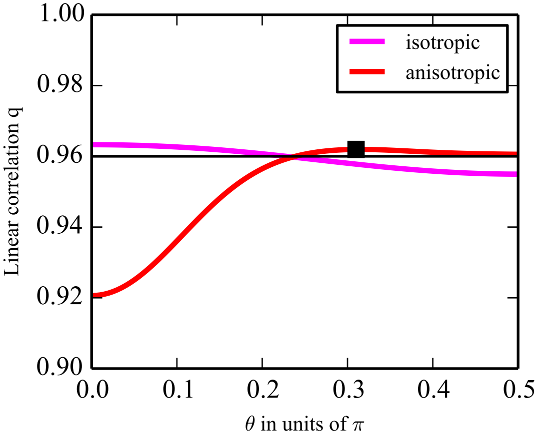

Figure 5.15: Correlation coefficient q describing the linear correlation between experimentally measured single kink energies (of the BCC metals Nb, Fe, Ta, Mo, W) and the product of the kink height and the prelogarithmic factor K_θ depending on the angle θ.

discussion above revealed that the pure edge dislocation should be energetically unfavorable due to its high elongation of the dislocation line length (see Figure 5.13). In order to resolve this apparent contradiction, Figure 5.15 investigates the θ-dependency of the linear correlation.

It shows the correlation coefficient between $aK^{\text{anis}}(\theta)$ and E_k^{exp} increases strongly with increasing θ until a plateau value of $q \approx 0.96$ is reached for $\theta \approx 0.23\pi(41^\circ)$. From this point on, q increases slowly until it reaches the maximum at $\theta = 0.31\pi(56^\circ)$, slightly above 0.96. After exceeding the maximum, q decreases slightly until $\theta = 0.5$.

Thus the data reveal that aK^{anis} correlates best with the experimental E_k for $\theta \gtrsim 40^\circ$ and the differences of q between 40° and 90° are negligibly small. This observation can be rationalized by the subsequent investigation of the $K^{\text{anis}}(\theta)$ of the different BCC materials.

Figure 5.16 shows that the differences between the single $K^{\text{anis}}(\theta)$ of the different materials vary stronger for smaller angles while for $\theta > 0.23\pi$ the differences remain almost constant. For instance, Fe and Nb have almost the same $K^{\text{anis}}(0)$,

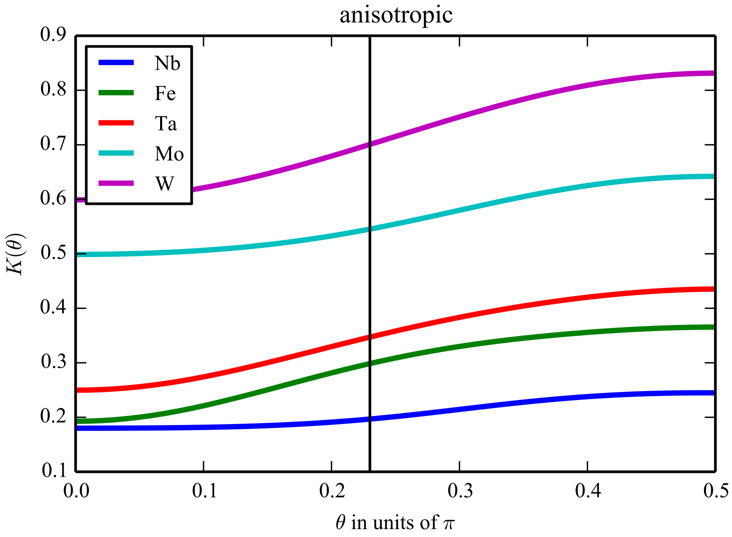

Figure 5.16: $K^{\mathrm{anis}}(\theta)$ of different BCC materials.

but due to the higher curvature of Fe around $\theta = 0$, the difference increases strongly for $0 < \theta < 0.23\pi$.

The comparison between Fe and Nb shows that materials that differ strongly in the elastic anisotropy factor A, like Fe and Nb (2.5 vs. 0.5), have different curvatures of $K(\theta)$ around $\theta = 0$. The different curvatures around the screw energy lead to different predictions of $aK^{\mathrm{anis}}(0)$ and $K^{\mathrm{anis}}(\theta \gg 0)$.

The data reveal the best correlations between E_k and $aK^{\mathrm{anis}}(\theta)$ with $\theta > 0.23\pi$, which is consistent with the assumption of kinks having an average orientation between a pure screw and edge configuration.

The following section uses the scaling law containing K_e^{anis} to predict E_k of different BCC HEA.

Ref.	Material	E_k [eV]	$\dot{\epsilon}_0$ [10^8 s $^{-1}$]
[22]	Nb	0.34	≈ 1.1
[97]	Fe	0.4515	≈ 150
[26]	Ta	0.554	≈ 0.5
[25]	Mo	0.635	≈ 55
[24]	W	1.05	≈ 430
this work	MoNbTaW	0.55	-
this work	MoNbTaVW	0.47	-
this work	MoNbTi	0.39	-
this work	AlCrMoTi	0.40	-
this work	AlMoNbTi	0.38	-
this work	AlCrMoNbTi	0.37	-
this work	HfNbTaTiZr	0.32	-
this work	HfNbTiZr	0.29	-
this work	HfNbTiVZr	0.28	-

Table 5.2: Experimental results from single kink energy measurements of different BCC metals and theoretical E_k-results of different BCC HEA from this work.

5.3.3 Thermal-athermal transition in BCC HEA

This section uses the scaling law from Section 5.3.2

$$E_k^{\mathrm{sc}} = \frac{a}{2.2} \cdot K_{\mathrm{e}}^{\mathrm{anis}}, \tag{5.20}$$

with kink height a and the prelogarithmic factor of the isotropic screw dislocation line energy to predict the single kink energies E_k of different BCC HEA. Table 5.2 lists the corresponding E_k results.

Figure 5.17 compares E_k^{sc} of different BCC HEA calculated by the scaling law with experimental E_k-values of Fe and Nb[97,22]. The graph suggests dividing E_k^{sc} values into three categories. There are alloys with E_k^{sc} close to Fe, alloys with E_k^{sc} close to Nb, and alloys with E_k^{sc} below Nb. The HEA with the lowest E_k^{sc} are the alloys containing Hf, Nb, Ti, and Zr. The observation of comparable low

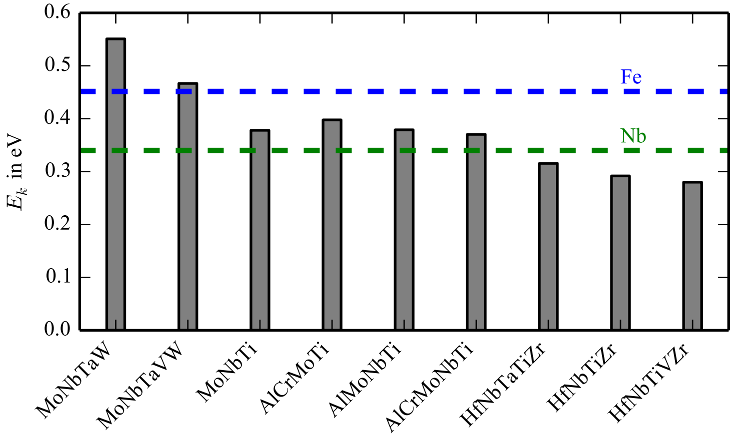

Figure 5.17: Single kink energy predictions for different BCC HEA from scaling law compared to experimental values of Fe and Nb (broken lines).

E_k^{sc} values can be explained by Figure 5.2 showing that the K_e^{anis} follows the rule of mixture. Hence, K_e^{anis} of BCC HEA equals roughly the average K_e^{anis} of the single HEA elements yielding average E_k^{sc}. The experimental E_k of Nb and Fe have been determined by measuring the thermal-athermal transition temperature (i.e., the knee temperature T_K) and fitting T_K to[22]

$$\ln(\dot{\epsilon}) = \ln \dot{\epsilon}_0 - \frac{1}{T_{\mathrm{K}}} \cdot 2E_k. \tag{5.21}$$

The knowledge of E_k allows us to calculate the knee temperatures corresponding to the scaling law predicted BCC HEA E_k by

$$T_K^{\mathrm{sc}} = \frac{2E_k}{k_B \ln(\dot{\epsilon}_0/\dot{\epsilon})}. \tag{5.22}$$

In conventional BCC metals and alloys, T_K denotes the temperature, which delivers enough thermal energy to create a double kink without external stress.

The quantity $\dot{\epsilon}_0$ is not material-specific since it depends mainly on the current

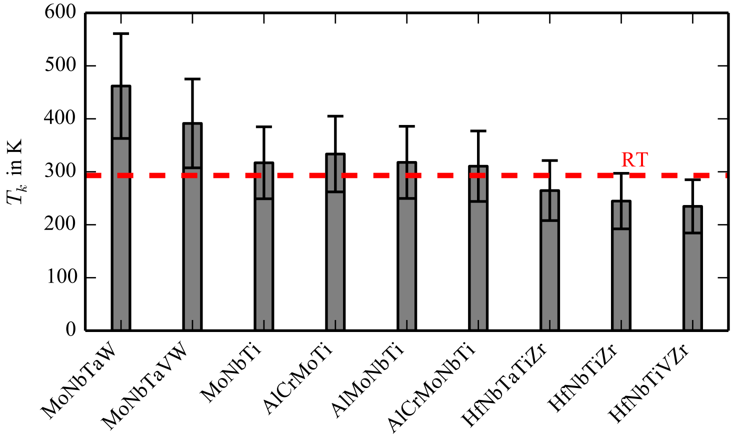

Figure 5.18: Knee temperature predictions for different BCC HEA from scaling law using the line-energy approach.

dislocation density. Analyzing experimentally measured $\dot{\epsilon}_0$ values from Tabular 5.1 reveals that a reasonable estimate for $\frac{1}{\ln(\dot{\epsilon}_0/\dot{\epsilon})}$ is in the range of 25-31 for a strain rate of $\dot{\epsilon} = 10^{-3}\ \mathrm{s}^{-1}$.

Figure 5.18 shows the T_K^{sc} of different BCC HEA corresponding to E_k calculated by the scaling law. The error bars denote the lower and upper values of T_K^{sc} corresponding to the estimated range of $\frac{1}{\ln(\dot{\epsilon}_0/\dot{\epsilon})} = 31$ and $\frac{1}{\ln(\dot{\epsilon}_0/\dot{\epsilon})} = 25$. It illustrates that the scaling law predicts for the first-generation Senkov alloys MoNbTaVW and MoNbTaVW a T_K^{sc} above RT. For the second-generation Senkov alloy HfNbTaTiZr (and its relatives), a T_K^{sc} below RT is predicted. Furthermore, scaling law predicts T_K^{sc} around room temperature (RT) for Al-Cr-Mo-Nb-Ti alloys and MoNbTi T_K^{sc}. The predicted T_K^{sc} are now compared to flow stress measurements from[32,5]. In order to reveal the thermal-athermal transition temperatures corresponding to the $\sigma - T$ curves from[32] and the hardness-temperatures curves from[5], the following fit function is used:

$$\sigma = (A(T_K^{\mathrm{fit}} - T))^2 + \sigma_{\mathrm{ath}}. \tag{5.23}$$

Note that the Equation (5.23) has the same form as the elastic interaction model from Seeger's kink pair nucleation theory[22].

Figures A.4-A.8 show that Equation (5.23) can reproduce the measured stress-temperature and hardness-temperature curves well. However, the excellent fit does not necessarily mean kink pair nucleation is the dominating deformation mechanism in the tested alloys since polynomial fit functions in the form of Equation (5.23) are generally used to model $\sigma - T$ curves[20,32]. The T_K^{fit} resulting from the fit are listed in Table 5.3. Uncertainties of the determined T_K through the fitting procedure have been estimated to ± 50K.

Comparing the knee temperatures listed in Table 5.3 reveals that the scaling law T_K^{sc} are lower than the T_K^{fit} estimated from flow stress measurements. The scaling law predicted T_K^{sc} reach from 235K to 462K. However, T_K^{fit} values reach from 605K to 1061K. Comparing the experimental data further reveals generally higher T_K^{fit} of BCC HEA (605K - 1061K) compared to directly measured T_K^{exp} of BCC metals (315K - 772K).

For the following discussion, we want to sum up two observations from above:

1. The scaling law predicted BCC HEA E_k and experimentally measured BCC metal E_k are of comparable magnitude (see Figure 5.17).
2. BCC HEA T_K^{fit} are higher than BCC metal T_K^{exp} (see Table 5.3).

The combination of observations 1 and 2 from above indicates that different mechanisms control plastic deformation in BCC metals and BCC HEA (in the considered temperature regime from RT - 1000K). Different dominating mechanisms in BCC metals and HEA are consistent with the screw dislocation Maresca-Curtin (MC-I) theory[35].

The MC-I theory argues that energetically favorable and unfavorable environments within the crystal matrix interact with dislocations (and kinks) and reduce dislocation (and kink) mobility[35]. The MC-I theory predicts that thermal energy can support dislocations and kinks to overcome barriers caused by the random crystal matrix. Hence, the MC-I theory predicts BCC HEA temperature-dependent flow stress at temperatures above the Seeger knee temperature $T_K^S \equiv \frac{2E_k}{k_B \ln(\dot{\epsilon}_0/\dot{\epsilon})}$. The observed transition temperatures ($\equiv T_K^{\text{HEA}}$) in[32] correspond to transitions

Ref.	Material	T_K[K]	$\dot{\epsilon}$ [10^{-3} s $^{-1}$]	$\dot{\epsilon_0}$ [10^{8} s $^{-1}$]
[22]	Nb	315	1.5	≈ 1.1
[97]	Fe	342	0.85	≈ 150
[26]	Ta	473	2	≈ 0.5
[25]	Mo	502	1	≈ 55
[24]	W	772	0.85	≈ 430
[32]	NbTaTiMo	1061 ± 50	1	-
[32]	NbTaTiW	995 ± 50	1	-
[32]	NbTaTi	917 ± 50	1	-
[32]	CrMoTaTi	605 ± 50	1	-
[5]	AlCrMoNbTi	752 ± 50	0.1	-
[5]	AlMoNbTi	660 ± 50	0.1	-
[5]	AlCrMoTi	657 ± 50	0.1	-
this work	MoNbTaW	462 ± 99	1	-
this work	MoNbTaVW	391 ± 84	1	-
this work	MoNbTi	317 ± 68	1	-
this work	AlCrMoTi	334 ± 71	1	-
this work	AlMoNbTi	318 ± 68	1	-
this work	AlCrMoNbTi	310 ± 67	1	-
this work	HfNbTaTiZr	265 ± 57	1	-
this work	HfNbTiZr	245 ± 52	1	-
this work	HfNbTiVZr	235 ± 50	1	-

Table 5.3: Experimental results from single kink energy measurements of different BCC metals and theoretical E_k-results of different BCC HEA from this work.

between deformation mechanisms specific to BCC HEA, which is consistent with the MC-I theory. The MC-I theory predicts different dominant deformation mechanisms for different temperature regimes (see Section 5.4.2).

The MC-I theory assumes that energetic favorable and unfavorable environments within the crystal matrix drive dislocations to create kinks to reduce the system's energy without any temperature contribution[35]. Hence, no external stress contribution would be necessary to provide enough kinks to avoid the Peierls barrier of conventional BCC metals and alloys. The low E_k of BCC HEA predicted from scaling law allows an alternative interpretation:

The low E_k and the corresponding T_K (see Figure 5.18) cause that for many BCC HEA, a sufficient number of kinks is provided already at $T \approx$ RT that the Peierls barrier no longer hinders dislocation mobility. However, in contrast to BCC metals, the random crystal matrix of BCC HEA still provides obstacles for dislocation and kink mobility. The obstacles due to the random crystal matrix lead to dependent flow stress at $T > T_K$. Since the single kink energy is an essential input parameter for the MC-I theory, the scaling law will be used later in this work (Section 5.4.2) to inform the MC-I theory to predict and discuss $\sigma - T$-curves for different BCC HEA.

The edge dislocation Maresca-Curtin (MC-II) theory[36] allows an alternative and completely different interpretation of observations 1 and 2. The MC-II theory assumes that the interaction between the distorted lattice of BCC HEA and edge dislocations reduces edge dislocation mobility. The reduction of the edge dislocation mobility is substantial enough that kink pair nucleation can no longer support plastic deformation since the mobility of the (edge-) kink is comparable low to the mobility of screw dislocations[36]. Consequently, the single kink energy does not play a role in the MC-II theory. The decisive parameters are the line tension and the solute misfit volumes resulting from different atomic radii of different elements[36].

The observation that the flow stress in a group of Al-Cr-Mo-Nb-Ta-Ti alloys scales with the atomic size difference (ASD)[5] is consistent with the MC-II theory since the ASD correlates with the MC-II misfit parameter[33,36,48]. The correlation between ASD and strength indicates reduced dislocation mobility through an interaction between dislocations and the distorted crystal matrix controls the strength.

The assumption of comparable mobility of screw and edge dislocations in BCC HEA is further supported by TEM investigations showing curved dislocations after deformation in MoNbTi[34] and in CrMoNbV and NbTaTiV[33]. According to[33,34,36], in at least some BCC HEA, edge dislocation strengthening determines the material's strength. This work will use the dislocation line tension and a misfit parameter calculated by DFT calculations to inform and discuss the MC-II theory for different Al-Cr-Mo-Nb-Ti alloys and Hf-Nb-Ta-Ti-Zr alloys in Section 5.4.1
A combination of the theoretical results from this work and the experimental observations[5,34,33] allow the interpretation that in AlCrMoTi, AlMoNbTi, AlCrMoNbTi, and MoNbTi comparable low E_k (corresponding to T_K slightly above RT) increase the mobility of screw dislocations by enabling kink pair nucleation with low energetic costs at RT. Hence, screw and edge dislocations are both mobile at RT. Within this interpretation, the measured T_K of[5] belong to thermally activated processes originating from interactions between edge-dislocations matrix interactions caused by spatial chemical fluctuations. Such thermally activated processes are consistent with a recently proposed solid solution strengthening theory[36], which will be discussed in Section 5.4.1.

5.3.4 Conclusions

This section presented a scaling law for effectively predicting single kink energies. Experimental single kink energies from BCC metals have been used for calibration. The presented scaling law has been used to predict single kink energies E_k and the corresponding knee temperatures T_K^{sc} of different BCC HEA. The results have been discussed in the context of Seeger's kink pair nucleation theory and compared to experimental flow stress measurements and RT deformation mechanism investigations.

- The formulated scaling law correlated well with experimental single kink energies of BCC metals and is thus consistent with experimental results.
- The scaling law predicts that BCC HEA have single kink energies E_k with values around the single kink energies of Nb and Fe.

- A comparison between BCC HEA knee temperatures from scaling law T_K^{sc} and knee temperatures from fitting experimentally measured stress-temperature and fitting the nano-hardness results indicate that kink pair nucleation is not the dominating mechanism in BCC HEA alloys from low to high temperatures.
- Solid solution strengthening specifically for BCC HEA can rationalize the observed $T_K^{\mathrm{fit}} >> T_k^{\mathrm{sc}}$.

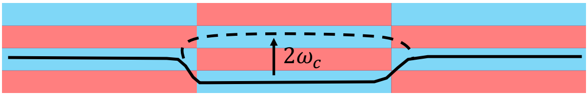

Figure 5.19: Edge dislocation glide postulated by edge strengthening model[36]. Dislocation glide operates by advancing the line segment-wise from energetically favorable positions over energetically unfavorable positions into the adjacent favorable position.

5.4 Solid solution strengthening

5.4.1 Edge dislocation strengthening

This section uses DFT material parameters, which have been calculated and presented within this work, to predict the temperature-dependent strength of BCC HEA by applying the MC-II model of Maresca and Curtin[36]. Their model is based on the work of Varvenne et al.[48].

Although Varvenne's model describes the strength of FCC HEA and Maresca's model the strength of BCC HEA, the basic assumptions are equal. Both theories postulate that the random distribution of solutes leads to local solute concentration fluctuations in the crystal matrix. Consequently, the dislocation line is attracted to fluctuations, which lower the system's energy, and is repelled by the ones that increase the system's energy.

The negative curvature term $\frac{\partial^2 K(\theta)}{\partial \theta^2}$ of the edge-dislocation line tension leads to the increased flexibility of edge dislocations compared to screw dislocations. Thus, they can minimize their energy by adapting a wavy structure to find a minimum energy path through the matrix. The resulting equilibrium structure depends on the dislocation line tension T and chemical fluctuations' characteristic potential energy contribution. The wavy dislocation line is parameterized within the model by wavelength ζ and an amplitude ω.

Dislocation glide operates without increasing the dislocation line length by advancing the line segment-wise from energetically favorable positions over energetically unfavorable positions into the adjacent favorable positions (see Figure 5.19).

The typical energy barrier, felt by advancing dislocation line segments, results from the energy difference between energetically favorable and unfavorable environments[36]

$$\Delta E_b = 1.11 \left(\frac{\omega T \Delta \tilde{E}_p^2}{b} \right)^{\frac{1}{3}} . \tag{5.24}$$

Applying an external stress $-\tau b \zeta x$ (with glide distance x) reduces the energy barrier. Assuming a sinusoidal energy landscape reveals a stress-dependent energy barrier

$$\Delta E(\tau) = \Delta E_b \left(1 - \frac{\tau}{\tau_{y0}} \right)^{3/2} , \tag{5.25}$$

with the zero temperature flow stress

$$\tau_{y0} = 1.01 \left(\frac{\Delta \tilde{E}_p^4}{T b^5 \omega^5} \right)^{1/3} . \tag{5.26}$$

With this, a thermally activated Arrhenius model can be derived, which describes the temperature and strain rate-dependent flow stress[36]

$$\tau_y(T, \dot{\epsilon}) = \tau_{y0} \exp \left[-\frac{1}{0.55} \left(\frac{k_B T}{\Delta E_b} \ln \frac{\dot{\epsilon}_0}{\dot{\epsilon}} \right)^{0.91} \right] . \tag{5.27}$$

A potential impediment for the usage of the presented model is the interaction energy parameter $\Delta \tilde{E}_p$, which is not easy to compute or to measure[48]. To address this problem, the Cottrell-Bilby formula

$$E_I = -\frac{\mu}{3\pi} \frac{(1+\nu)}{1-\nu} \underbrace{\frac{y}{(x^2+y^2)}}_{\equiv f(x,y)} \Delta V_{\text{mis}}, \tag{5.28}$$

can be used to reduce the solute/dislocation interaction energy to the elastic contribution[13,36,48]. Here, x and y are the spatial coordinates of the solute relative to the edge dislocation, which resides along the z-axis and has a Burgers vector parallel to the x-axis. Based on the Cottrell-Bilby formula, one can use a reduced interaction energy parameter as a place-in for $\Delta\tilde{E}_b$[36]:

$$\Delta\tilde{E}_b(\omega) \approx \frac{\mu}{3\pi}\frac{(1+\nu)}{(1-\nu)}\left[\sum_{i,j}\Delta f_{ij}^2(\omega)\right]^{1/2}\cdot\left[\sum_n c_n\Delta V_n\right]^{1/2}, \qquad (5.29)$$

with the key misfit volume quantity $\Delta V_n = \Delta\bar{V}_n^2 + \sigma_{\Delta V_n}^2$.

Here, $\Delta\bar{V}_n$ is the average misfit volume corresponding to element n and $\sigma_{\Delta V_n}$ is its standard deviation due to the specific atomic environments (see Section 4.3 for a detailed discussion).

Combination of the Equations (5.24), (5.29) and (5.27) yield the key equations for the reduced model:

$$\tau_{y,0} = \frac{f^{\tau_{y,0}}}{2}\left(\frac{b^2\mu^4}{T}\right)^{\frac{1}{3}}\left[\frac{(1+\nu)}{(1-\nu)}\right]^{\frac{4}{3}}\left[\frac{\sum_n c_n\Delta V}{b^6}\right]^{\frac{2}{3}} \qquad (5.30)$$

$$\Delta E_b = \frac{f^{\Delta E_b}}{2}\left(T\mu^2b^7\right)^{\frac{1}{3}}\left[\frac{(1+\nu)}{(1-\nu)}\right]^{\frac{2}{3}}\left[\frac{\sum_n c_n\Delta V}{b^6}\right]^{\frac{1}{3}}, \qquad (5.31)$$

with $f^{\tau_{y,0}} = \left[\sum_{i,j}\Delta f_{i,j}(\omega)\right]^{\frac{2}{3}}$ and $f^{\Delta E_b} = \left[\sum_{i,j}\Delta f_{i,j}(\omega)\right]^{\frac{1}{3}}$[36].

Note, that the prefactors $1/2$ are calculated due to an estimated $\omega/b \approx 3.1$[36]. The equations show that both quantities depend only weakly on the line tension, which justifies considering the logarithmic factor in $T = B\cdot\ln(R/r_0)$ as a constant.

The crucial point of the reduced MC-II theory is the factors containing $f_{i,j}(\omega) = f(x_i-\omega, y_j) - f(x_i, y_j)$ since they are neither directly accessible by an analytical formula nor by experiments. They contain the dimensionless anisotropic pressure field $f(x_i, y_j)$, generated by the distribution of normalized Burger's vectors along the glide plane. To estimate these parameters, Maresca and Curtin calculated effective prefactors by fitting the reduced theory to the results of the full theory[36]. Then, the full theory was applied using EAM-type potentials and molecular statics simulations.

In this work, an analytic determination of the prefactors corresponding to $f(x_i, y_j)$

is beyond the scope. Hence, absolute strength values of single alloys can not be determined. However, setting the prefactors $= 1$ allows us to compare strengthening trends between different alloys. At this point, we use the fact that the ratio between the stress at zero temperature of two alloys $\frac{\tau_{y,0,1}}{\tau_{y,0,2}}$ is independent of $f^{\tau_{y,0}}$ due to the linear dependency.

In order to evaluate the exponential flow stress decay with increasing temperature, one has to determine the energy barrier ΔE_b together with the logarithmic strain rate factor $\ln(\dot{\epsilon}_0/\dot{\epsilon})$. For this study $\ln(\dot{\epsilon}_0/\dot{\epsilon}) = 16$ is assumed, which corresponds to $\dot{\epsilon}_0 = 10^4\ \mathrm{s}^{-1}$ [36] and a typical experimental strain rate of $\dot{\epsilon} = 10^{-3}\ \mathrm{s}^{-1}$.

The prefactors $f^{\Delta E_b}$ and f^{τ} have been determined to match the prefactors given by a reduced model in [36].

In contrast, this work parametrizes the model with the line tension, shear modulus, and atomic misfit volumes from DFT. DFT calculations have determined the line tension and shear modulus values. For the non-equimolar compositions, this work used the elastic properties of the corresponding four-component equimolar composition. The resulting error is expected to be small due to the high concentration differences in the considered non-equimolar compositions (e.g., 4% Cr in $\mathrm{AlCr_{0.04}MoNbTi}$). In order to determine the misfit volumes, $\Delta V_n = V_n - \bar{V}$, two different approaches have been applied:

1. The rule of mixtures determined the mean atomic volume $\bar{V}$, and the elemental radii determined V_n.

2. The mean atomic volume has been determined from the atomic volume resulting from relaxing an SQS by DFT simulations. The single elemental atomic volumes have been extracted from a Voronoi analysis of relaxed SQS. The influence of the specific atomic environment has been incorporated through the standard deviations $\sigma_{\Delta V_i}$ by $\Delta V_n = \Delta\bar{V}_n^2 + \sigma_{\Delta V_n}^2$.

Both methods have been discussed and compared in Section 4.3. The analysis revealed that the values of $\sum_n c_n \Delta V$ parameterized with misfit volumes from the second method are typically reduced by factor 2.5 - 4 compared to a parameterization with misfit volumes from ROM or the DFT and EAM models [36]. Hence, an empirical scaling factor 3.25 was used to reveal comparable results

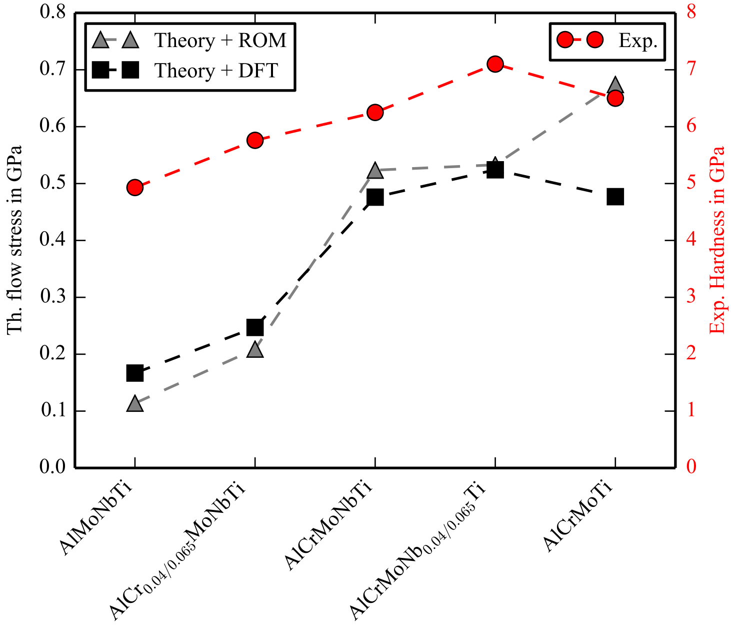

Figure 5.20: Normalized flow stress at RT predicted by Edge strengthening theory with misfit volume parameter from DFT (orange) and from elemental radii (blue). Normalization for better comparability to the corresponding maximum value of the computed alloy series. For the theoretically determined values non-equimolar compositions with 4% Cr or Nb have been considered. The experimental hardness values have determined with non-equimolar samples containing 6.5% Cr or Nb.

from $\sum_n c_n \Delta V^{\mathrm{DFT}}$ and $\sum_n c_n \Delta V^{\mathrm{ROM}}$.

Figure 5.20 compares experimental micro-hardness data with flow stress predictions for five different Al-Cr-Mo-Nb-Ti alloys with different Cr-content and Nb-content. Here only a qualitative discussion is possible since we cannot compare the absolute values of the theoretical flow stress and the experimental micro-hardness. While the theoretical flow stress denotes the stress to move a single dislocation within a single crystal, the micro-hardness describes the resistance of the macroscopic material against plastic deformation. Consequently, there are effects not captured by the used model: the sample's microstructure, the (strain-dependent)

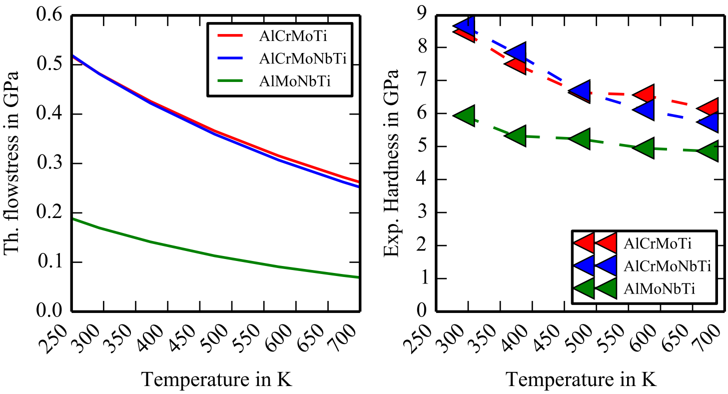

Figure 5.21: Flow stress values from MC-II model (squares and full line) compared to experimental hardness values (triangles and dashed line) from nano-indentation normalized by factor 3.0.

dislocation density, and plastic anisotropy, which influence the hardness.

The data show that the MC-II model predicts increasing strength with increasing Cr-content from AlMoNbTi to AlCrMoNbTi. This trend is consistent with the experimental hardness measurement and is independent of input misfit volumes (ROM vs. DFT).

The reduction of the Nb-content from AlMoNbCrTi to AlMoCrTi shows a non-linear influence on the experimental hardness values, with maximum hardness for AlCrMoNb$_{0.065}$Ti and comparable hardness of AlCrMoNbTi and AlMoCrTi. Only the DFT-informed model predicts the non-linear influence of the Nb reduction. The different predictions of the ROM- and DFT-informed model for the alloys with high Cr-content can be attributed to the inability of the ROM to describe the mean bond lengths of Cr-X bonds in the HEA matrix (see Section 4.3 for a detailed discussion).

Although the DFT-informed model captures the hardness trend very well, it over-predicts the relative changes in the hardness of alloys with high and low Cr-content.

A possible explanation is that through the hardness measurements, it comes to severe plastic deformation in the indent surrounding material, which could lead to material-specific strain hardening[11]. Thus an increased athermal strain hardening contribution on the strength of the tested HEA with low Cr-content could lead to an experimental overprediction of the intrinsic strength of these materials and consequently rationalize the differences between experiment and theory. In order to get additional insights, temperature-dependent hardness values from nano-indentation experiments are compared to flow stress predictions.

Figure 5.21 illustrates that the theory is consistent with several features revealed by the experiment:

- Higher flow stress levels of AlCrMoNbTi and AlCrMoTi compared to AlMoNbTi.
- Similar flow stress of AlCrMoNbTi and AlMoCrTi over a wide temperature range.
- Faster flowstress decay with increasing temperature of AlCrMoNbTi and AlMoCrTi compared to AlMoNbTi.

Based on these observations, the MC-II model can describe the temperature-dependent flow stress in Al-Cr-Mo-Nb-Ti alloys, which implies a dominant role of edge dislocations in the considered alloys.

However, the nano-hardness data of AlCrMoNbTi, AlCrMoTi, and AlMoNbTi show a slope change[5,11], which is not captured by the theory. Therefore, one can interpret the slope change as a change in the deformation mechanism, e.g., from screw dislocation dominated to edge dislocation dominated plasticity. As discussed in Section 5.3.3, such a change of the dominant deformation mechanisms could also appear when the temperature exceeds the knee temperature T_K. However, the slope change appears for AlMoNbTi at $\approx$ 400K and for AlCrMoNbTi and AlCrMoTi at $\approx$ 500K. The predicted knee temperatures corresponding to Seeger's double kink nucleation are according to the findings presented in Section 5.3.3 in the range of 330K-355K and are thus too low to explain the change of the slope of the nano-hardness in AlCrMoTi and AlCrMONbTi.

Consequently, the predicted T_K are either underestimated or the presented models cannot fully capture the operating deformation mechanisms.

The following section discusses another model which describes thermally activated plasticity in BCC HEA. However, in contrast to the MC-II model, within this model, screw dislocations dominate plastic deformation.

5.4.2 Screw dislocation strengthening

This section uses the calculated DFT material parameters to predict the temperature-dependent strength of BCC HEA by applying the MC-I model. The model will be briefly introduced in the following, but for details, it is referred to the original publication[35].

While the MC-II model describes the edge dislocation mobility in random alloys, the screw theory used in this section describes the mobility of screw dislocations. Like Seeger's theory, a fundamental assumption of the screw theory is that the nonplanar core configuration of screw dislocations reduces their mobility. Thus mechanisms based on kink pair formation mediate plastic deformation. The predominant difference between the screw theory and Seeger's theory is the assumption that screw dislocations have a kinked structure already at zero temperature without external stress contribution.

Hence, in contrast to Seeger's theory, the kink energy in the screw theory does not serve as the activation energy for kink pair formation but is one of two fundamental material properties that control the kinked dislocation structure.

Besides the kink energy, the second key input parameter is the potential energy contribution per unit Burgers vector of the dislocation line length $\Delta\tilde{E}_p$. It describes the mean energy difference per Burgers vector if a dislocation segment moves from one Peierls valley to the neighboring valley.

Stochastic simulations determined with these two parameters the critical length ζ_c, which minimizes the dislocation energy[35]. ζ_c defines the spacing between two kinks. The stochastic simulations revealed that this characteristic length could be analytically estimated by

$$\zeta_c = \left(1.083\frac{E_k}{\Delta\tilde{E}_p}\right)^2 b. \tag{5.32}$$

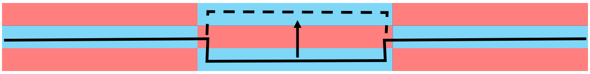

Figure 5.22: Schematic picture of Peierls mechanism corresponding to the Maresca Curtin Model.

given a pre-kinked structure with the characteristic length ζ_c, plastic deformation is proposed to operate by three different mechanisms depending on temperature regimes[35]:

- **Peierls mechanism** at lower temperatures, if the activation stress of Peierls mechanism is lower than that of kink glide.
- **Lateral kink glide** at higher temperatures or all temperatures if the activation stress of lateral kink glide is lower than that of the Peierls mechanism.
- **Cross kink formation** at all temperatures.

In the MC-I model, the Peierls mechanism describes that a straight segment in a low-energy area moves over a high-energy area in the adjacent low-energy area (see Figure 5.22). Within this process, no additional kinks must be formed, and the activation energy depends only on the Peierls barrier V_P, the energy parameter $\Delta\tilde{E}_p$ and the critical length ζ_c. The temperature and strain rate-dependent activation stress for this mechanism is modeled by

$$\tau_P(\dot{\epsilon}, T) = \tau_{P,0}\left[1 - \left(\frac{k_B T}{\Delta E_{b,P}}\right)^{2/3}\right] \tag{5.33}$$

with

$$\tau_{P,0} = \frac{\pi \Delta V_P}{ba} + \frac{0.44 E_k}{ba\zeta_c}\left[1 - \frac{5\Delta V_P \zeta_c}{(20\Delta V_P \zeta_c + 0.7E_k)}\right] \tag{5.34}$$

$$\Delta E_{b,P} = \frac{(10\Delta V_P \zeta_c + 0.7E_k)^3}{(20\Delta V_P \zeta_c + 0.7E_k)^2}, \tag{5.35}$$

where $\tau_{P,0}$ describes the zero temperature Peierls stress and $\Delta E_{b,P}$ the corresponding activation barrier[35].

The equations show that the energy barrier increases with Peierls potential ΔV_P, segment length, and single kink energy E_k. Hence, increasing single kink energy reduces the temperature sensitivity, while a decreasing energy parameter $\Delta\tilde{E}_p$ increases the temperature sensitivity. The zero temperature Peierls stress increases with increasing ΔV_p and $\Delta\tilde{E}_p$.

The second mechanism describes the lateral glide of edge-type kinks along the screw line. The lateral glide of kinks moves a segment in a low-energy area to the adjacent higher-energy area. The higher-energy area is a transition state from which the dislocation segment can spontaneously move to the adjacent lower-energy area. Local energy fluctuations inhibit kink-glide and serve as pinning points. Further, kink-glide is inhibited by moving a segment from a lower to a higher energy area, causing a constant back-stress $\tau_b = \frac{1.08E_k}{ab\zeta_c}$. One can find the exact analytic expression for the resulting activation stress in[35]. Usually, the activation stress of the kink glide mechanism is more temperature sensitive than the activation stress of the Peierls mechanism, which may cause a transition from the Peierls mechanism to the kink glide mechanism at temperatures $T > 0$[35].

The third mechanism is the formation of cross kinks due to the lateral kink glide of two opposing kinks in two different glide planes. These cross kinks serve as pinning points of the dislocation line. In order to overcome these pinning points, the failure of cross kinks is necessary[35]. The failure causes the creation of a vacancy or self-interstitial. The energy barrier is thus modeled by a sinusoidal potential with the amplitude $\frac{E_{\mathrm{v/i}}}{2}$, with the vacancy/interstitial formation energy $E_{\mathrm{v/i}}$. The activation stress is given by[35]

$$\tau_{\mathrm{xk}}(\dot{\epsilon}, T) = \tau_{\mathrm{xk,0}} \left[1 - \left(\frac{k_B T}{E_{\mathrm{v/i}}}\right)^{2/3}\right] \tag{5.36}$$

with

$$\tau_{\mathrm{xk,0}} = \frac{\pi E_{\mathrm{v/i}}}{ab\zeta_{\mathrm{c}}}. \tag{5.37}$$

The equations show that cross kink strengthening at 0K increases with increasing vacancy/interstitial formation energy $E_{\mathrm{v/i}}$ and decreasing segment length ζ_c. Hence, cross-kink strengthening is most decisive in materials with high $\Delta E_{\mathrm{v/i}}$ and small ζ_c.

The resulting flow stress τ depends on the single flow stress contributions in the following way[35]:

$$\tau(\dot{\epsilon}, T) = \tau_{\text{xk}}(\dot{\epsilon}, T) + \min\left[\tau_P(\dot{\epsilon}, T), \tau_k(\dot{\epsilon}, T)\right]. \tag{5.38}$$

The equation assumes that cross-kink failure is always present. The equations also assume that the Peierls mechanism operates only if $\tau_P(\dot{\epsilon}, T) < \tau_k(\dot{\epsilon}, T)$ and kink glide operates only if $\tau_P(\dot{\epsilon}, T) > \tau_k(\dot{\epsilon}, T)$. The temperature sensitivity of τ_k is generally higher than the temperature sensitivity of τ_P[35]. Consequently, the model predicts that transitions from the Peierls mechanism to kink glide as a dominant deformation mechanism can appear.

Figure 5.23 shows how variations of different input parameters influence the stresses corresponding to different mechanisms and the resulting flow stress.

Figure 5.23 (upper left) shows that increasing $\Delta\tilde{E}_p$ increases the flow stress contribution from cross kink failure τ_{xk} and lateral kink glide τ_k at all temperatures. The temperature sensitivity of τ_k increases with increasing $\Delta\tilde{E}_p$. The temperature sensitivity of τ_{xk} is unaffected. Further, increasing $\Delta\tilde{E}_p$ decreases the stress contribution from Peierls mechanism τ_P at all temperatures. Increasing τ_k and decreasing τ_P shifts the intersection between τ_k and τ_P to higher temperatures. Consequently, the transition from Peierls mechanism to lateral kink glide as the dominant deformation mechanism is shifted to higher temperatures.

Figure 5.23 (upper right) shows that increasing the single kink energy E_k increases τ_P and decreases τ_k and τ_{xk}. The resulting flow stress is decreased at all temperatures, and the transition of the dominant deformation mechanism (from Peierls mechanism to lateral kink glide) is shifted to lower temperatures.

Figure 5.23 (lower left) shows that increasing $E_{v/i}$ increases τ_{xp} and does not affect τ_P and τ_k. Hence the flow stress is increased at temperatures.

Figure 5.23 (lower right) shows that increasing the Peierls potential height V_p increases τ_P at all temperatures and does not affect τ_k and τ_{xk}. The transition of the dominant deformation mechanism (from Peierls mechanism to lateral kink glide) is shifted to lower temperatures.

In the following, the MC-I model is applied to predict the flow stress of AlCrMoTi

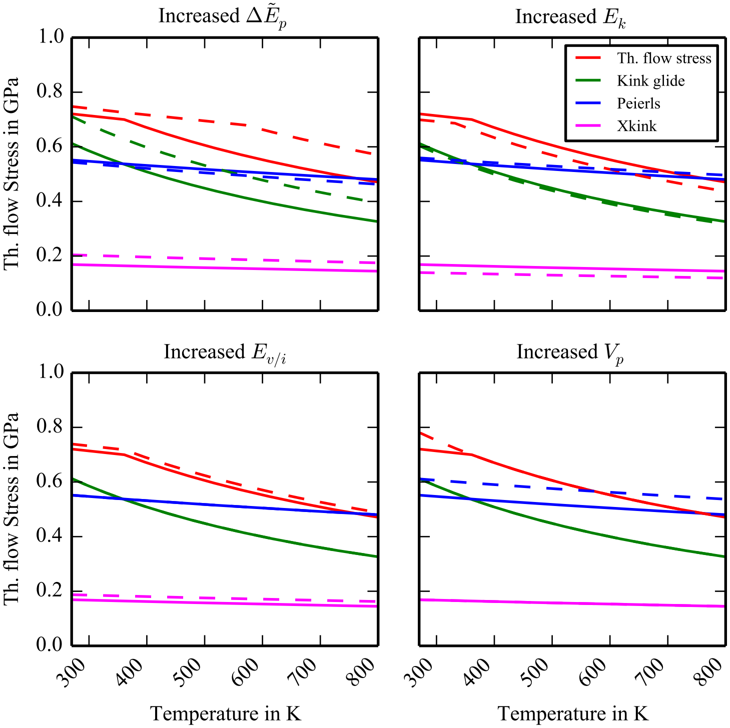

Figure 5.23: Solid lines: Exemplary temperature-dependent theoretical flow stress predictions from the Maresca-Curtin model with input parameters: $a_0 = 3.09$ Å, $E_k = 0.43$ eV, $\Delta\tilde{E}_p = 0.071$ eV, $E_\mathrm{i} = 5.1$ eV, $E_v = 2.22$ eV, $V_p = 0.022$ eV.
Upper left: Dashed lines corresponds to flow stress for $\Delta\tilde{E}_p$ increased by 10 %.
Upper right: Dashed lines corresponds to flow stress for E_p increased by 10 %.
Lower left: Dashed lines corresponds to flow stress for E_i and E_v increased by 10 %.
Lower right: Dashed lines corresponds to flow stress for V_p increased by 10 %.

	a_0 [Å]	E_k [eV]	$\Delta\tilde{E}_p$ [meV]	ΔV_P [meV]	E_i [eV]	E_v[eV]
HfNbTiZr	3.43	0.29	[40 - 85]*	16	[3.3 - 5.9]*	[1.6 - 3.0]*
AlCrMoTi	3.09	0.40	[40 - 85]*	26	[3.3 - 5.9]*	[1.6 - 3.0]*

Table 5.4: Used parameter for MC-I theory. The ranges [...]* belong to values found for different random BCC alloys in[35].

and HfNbTiZr. The lattice constants a_0 are predicted by DFT calculations (see Table 4.1). The single kink energies E_k are predicted by the scaling law presented in Section 5.3.3 (see Table 5.2) and the Peierls potential height is predicted by a similar scaling law $V_P = 0.11 \cdot K_s$ (see Figure 5.12) with the prelogarithmic factor K_s of the screw dislocation line energy. Calculating the interaction parameter $\Delta\tilde{E}_p$ and the interstitial/vacancy creation energies $E_\text{i/v}$ is beyond the scope of this work. The following discussion assumes that HfNbTiZr and AlCrMoTi have $\Delta\tilde{E}_p$ and $E_\text{i/v}$ in the range of different random BCC alloys (Fe$_x$Si, Nb$_x$Mo, Nb$_x$W and Ti$_x$Nb$_y$Zr) given by[35]. We assume $\omega_k = 15 \pm 5$ b[35] for the kink width.

Figure 5.24 shows that the MC-I model predicts $\tau_k < \tau_P$ for $T > 250$K and $\Delta\tilde{E}_p = 0.04$eV. The Figure further shows that the MC-I model predicts $\tau_k = \tau_P$ at $T = 293$K (RT) and $\Delta\tilde{E}_p = 0.054 \pm 0.002$ eV. Hence, in HfNbTiZr, a comparable small $\Delta\tilde{E}_p$ (in[35], values between 0.04 and 0.085 eVare predicted for different random BCC alloys) is sufficient to cause a transition from lateral kink glide to Peierls mechanism dominated plastic deformation at temperatures around RT. Consequently, the MC-I models predict that in HfNbTiZr, deformation is most likely mediated by the Peierls mechanism.

Application of the MC-I model on AlCrMoTi predicts $\tau_k = \tau_P$ at $T = 293$K (RT) and $\Delta\tilde{E}_p = 0.078 \pm 0.003$ eV. Hence in AlCrMoTi, a comparable large $\Delta\tilde{E}_p$ (in[35], values between 0.04eV and 0.085eV are predicted for different random BCC alloys) is necessary to cause a transition from lateral kink glide to Peierls mechanism dominated plastic deformation at temperatures around RT.

Figure 5.25 compares the flow stress of HfNbTiZr and AlCrMoTi predicted by the MC-I model at room temperature ($T = 293$K). The input values for the

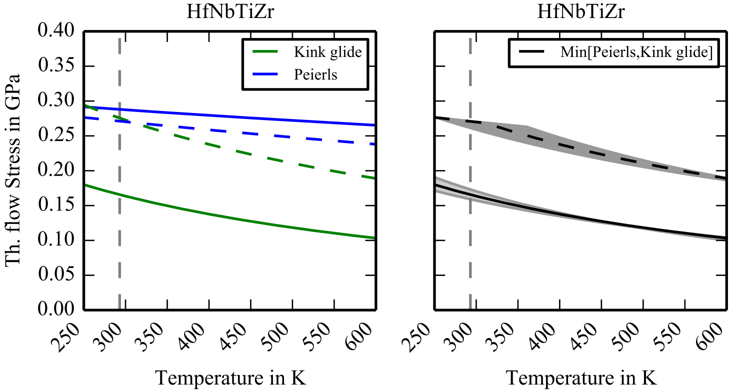

Figure 5.24: Flow stress prediction from MC-I model for HfNbTiZr with parameter from Table 5.4 and $\omega_k/b = 15 \pm 5$. **Left:** Predicted flow stress attributed to kink glide mechanism (green line) and Peierls mechanism (blue line) for $\Delta\tilde{E}_p = 0.04\text{eV}$ (whole line) and $\Delta\tilde{E}_p = 0.054\text{eV}$ (broken line). **Right:** Effective flow stress contribution of Peierls mechanism and lateral kink glide for $\Delta\tilde{E}_p = 0.04\text{eV}$ (whole line) and $\Delta\tilde{E}_p = 0.054\text{eV}$ (broken line).

model have been chosen according to Table 5.4. The flow stress results are also listed in Table 5.5. The values belong to minimum and maximum values resulting from using the ranges in Table 5.4 as input parameters for the MC-I model. The MC-I model predicts small flow stress differences (0.23GPa vs 0.26GPa) between HfNbTiZr and AlCrMoTi if the upper limits of the ranges are used. Using the upper limits of $\Delta\tilde{E}_p$ and $E_{\text{v/i}}$ increases the flow stress differences between HfNbTiZr and AlCrMoTi (0.77GPa vs 1.00GPa). Using the upper limits of $\Delta\tilde{E}_p$ and the lower limits of $E_{\text{v/i}}$ reveals the largest flow stress differences between HfNbTiZr and AlCrMoTi (0.51GPa vs 0.81GPa). Although the predicted τ are larger for AlCrMoTi than for HfNbTiZr, the predicted τ_{xk} are larger for HfNbTiZr than for AlCrMoTi. Both observations can be explained by Equations (5.37) and (5.32). The equations reveal a decreasing critical length ζ_c between two kinks with decreasing E_k and increasing $\Delta\tilde{E}_p$. DFT calculations predicted a smaller E_k for HfNbTiZr than for AlCrMoTi. Hence, ζ_c decreases with increasing $\Delta\tilde{E}_p$ faster for HfNbTiZr than for AlCrMoTi. Consequently, τ_{xk} increases faster

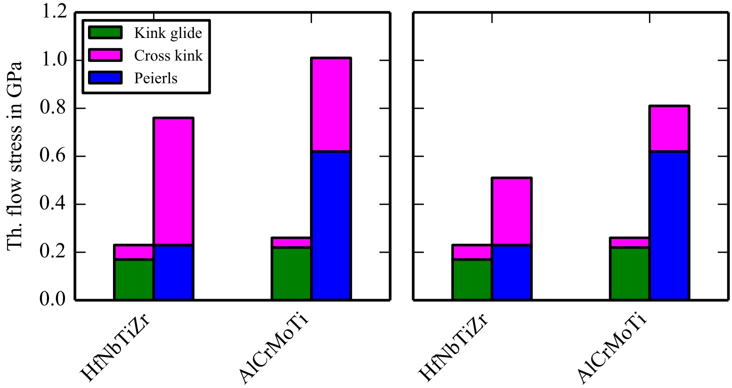

Figure 5.25: Predicted flow stress τ at $T = 293$K for HfNbTiZr and AlCrMoTi. The used input parameter for the MC-I model are listed in Table 5.4. colors denote the contributions according to different deformation mechanisms (Peierls mechanism, lateral kink glide, and cross kink failure) predicted by the MC-I model[35].

with increasing $\Delta\tilde{E}_p$ and $E_{\mathrm{v/i}}$ in HfNbTiZr than in AlCrMoTi.

Figure 5.24 further reveals $\tau_{xk} > \tau_P$ for HfNbTiZr and $\tau_{xk} > \tau_P$ for AlCrMoTi. This observation can also be explained by inspecting the DFT input parameter of both alloys: First, the small E_k of HfNbTiZr yields a rapid increase of τ_{xk} in HfNbTiZr as discussed above. Second, the small Peierls potential height V_P of HfNbTiZr yields a small stress τ_P.

In sum, the analysis shows that the flow stresses of HfNbTiZr and AlCrMoTi strongly depend on $\Delta\tilde{E}_p$ and $E_{\mathrm{v/i}}$. Precise knowledge of both parameters is necessary to predict absolute flow stress values with the MC-I model.

Consequently, this work cannot make a conclusive statement about the strength of HfNbTiZr and AlCrMoTi resulting from screw dislocation solid solution strengthening. Further, the MC-I model cannot be evaluated with experimental data due to the uncertainties of $\Delta\tilde{E}_p$. Nevertheless, the analysis revealed that the MC-I model predicts a proportional larger cross-kink strengthening contribution in HfNbTiZr than in AlCrMoTi. Note that the high energy barriers corresponding

$\Delta\tilde{E}_p \downarrow\uparrow, E_{\text{v/i}} \downarrow\uparrow$	τ_k [GPa]	τ_P [GPa]	τ_{xk} [GPa]	τ [GPa]
HfNbTiZr	**0.17** - 0.57	0.29 - **0.23**	0.06 - 0.53	0.23 - 0.77
AlCrMoTi	**0.22** - 0.73	0.69 - **0.62**	0.04 - 0.39	0.26 - 1.00
$\Delta\tilde{E}_p \downarrow\uparrow, E_{\text{v/i}} \downarrow$	τ_k [GPa]	τ_P [GPa]	τ_{xk} [GPa]	τ [GPa]
HfNbTiZr	**0.17** - 0.57	0.29 - **0.23**	0.06 - 0.28	0.23 - 0.51
AlCrMoTi	**0.22** - 0.73	0.69 - **0.62**	0.04 - 0.19	0.26 - 0.81

Table 5.5: Flow stress results for HfNbTiZr and AlCrMoTi. The values are predicted by the MC-I model with input parameters from Table 5.4. **Top:** Values belong to lower and upper limits of $\Delta\tilde{E}_p$ and $E_{\text{v/i}}$ as input parameter. **Bottom:** Values belong to lower and upper limits of $\Delta\tilde{E}_p$ and lower limits $E_{\text{v/i}}$ as input parameter.

to cross-kink failure can explain the high temperature strength of BCC HEA discussed in Section 5.3.3. Finally, the observation that cross-kink strengthening can be defeated at sufficiently high temperatures by the migration of vacancies can explain the rapid loss of strength of some BCC HEA in the vicinity of $0.6T_m$ (melting temperature)[35,32].

5.4.3 Conclusions

Section 5.4.1 introduced and applied the MC-II model[36] with the DFT input parameter from this work. The MC-II model predicts the strength of BCC HEA based on reduced edge dislocation mobility. The model was applied with input parameters from this work to predict the strength of five Al-Cr-Mo-Nb-Ti alloys with different Cr- and Nb-content. The predicted strengths have been compared with hardness values from nano-indentation experiments[5]. Analysis of the model and the experimental results revealed the following observations:

- The MC-II model predicts increasing strength with increasing Cr-content, consistent with experimental hardness values.

- The DFT-informed MC-II model predicts a non-linear dependency of strength and Nb-content. The predicted trend is consistent with experimental hardness results.

Section 5.4.2 introduced and applied the MC-I model[35] with the DFT input parameter from this work. The MC-I model predicts the strength of BCC HEA based on reduced screw dislocation mobility. The model was applied with input parameters from this work to compare and discuss predictions for HfNbTiZr and AlCrMoTi. Analysis of the model revealed the following observations:

- The MC-I model predicts due to the low Peierls potential height and single kink energy of HfNbTiZr (predicted by DFT), that plastic deformation in HfNbTiZr is mediated predominantly by the Peierls mechanism and by cross kink failure.
- The MC-I model predicts, due to the high Peierls potential height and single kink energy of AlCrMoTi (predicted by DFT), that lateral kink glide is likely to be the predominant deformation mechanism in AlCrMoTi.

6 Conclusions and Outlook

This work aimed to investigate the deformation mechanisms of BCC HEA with a combination of ab Initio calculations and different models from dislocation theory. Investigating deformation mechanisms provides insights into the reasons for different macroscopic material properties of different HEA, e.g., strength and ductility.

This work observed mainly two BCC HEA, AlCrMoTi and HfNbTiZr since they are considered representatives of the room temperature brittle HEA family Al-Cr-Mo-Nb-Ti and the room temperature ductile HEA family Hf-Nb-Ta-Ti-Zr.

In order to inform the different dislocation models, various material quantities have been calculated by DFT calculations. In the cases where experimental values had been accessible, comparisons revealed that theoretical values were consistent with experimental values. An analysis of values resulting from Vegard's law revealed that material parameters from Vegard's law are consistent with DFT- and experimental results.

In order to involve and investigate the influence of crystallographic ordering on material properties, the first chapter showed and discussed electronic ground state energy results from differently ordered lattice configurations of AlCrMoTi and HfNbTiZr based on a free energy model. This investigation indicated that chemical order does not play a role in HfNbTiZr at room temperature, but it is expected in AlCrMoTi.

In AlCrMoTi, Al and Ti atoms are distributed on two different simple cubic superlattices in the energetically favorable lattice configurations. Based on these findings, this work suggests that in AlCrMoTi Al-Al and Al-Ti bonds are energetically favorable over all other bond types. After making this observation, a model was created to explain the order-disorder phase transition in relation to the concentration of Al.

The appearance of crystallographic ordering in AlCrMoTi can be interpreted as the reason for the room temperature brittleness in AlCrMoTi. However, to understand the distinct connection between ductility and crystallographic ordering, the influence of crystallographic ordering on the deformation mechanisms had to be evaluated. Thus, the appearance of crystallographic ordering was considered for all material quantity calculations in the case of AlCrMoTi.

DFT calculations predicted only a small influence on the elastic tensor, resulting in an increased elastic anisotropy of ordered AlCrMoTi compared to the disordered one. Within a line tension model, the increased anisotropy of ordered AlCrMoTi implies an increased resistance of screw dislocations against bowing out around obstacles like precipitates or energetically unfavorable environments.

However, the influence of chemical ordering is small compared to the differences between AlCrMoTi and HfNbTiZr. Hence, it is questionable whether the influence of crystallographic ordering on the elastic constants is large enough to impact deformation mechanisms.

The lattice and elastic constants calculated through DFT are utilized as input parameters to predict single kink energies using a scaling law. The scaling law predicts a significantly reduced single kink energy of HfNbTiZr compared to AlCrMoTi. Thus, the model indicates different active deformation mechanisms at room temperature in both alloys. However, the kink pair nucleation model considers HEA as monoatomic metals with material properties revealed from the average over the whole HEA crystal matrix. The possible influence of chemical fluctuations is completely neglected. Hence, additional material parameters, which include chemical fluctuations, are calculated by DFT.

First, standard deviations corresponding to atomic bond lengths and atomic misfit volumes are extracted from relaxed supercells representing HfNbTiZr and several alloys from the Al-Cr-Mo-Nb-Ti family. Based on the assumption of a dominant role of edge dislocations, an interpretation of these values within a solid solution strengthening model from Maresca and Curtin[36] is consistent with experimental hardness values from the Al-Cr-Mo-Nb-Ti family. However, further studies are necessary to make conclusive statements about the role of edge dislocations in BCC HEA. Primarily since the exact nature of dislocation-solute interaction has yet to be understood.

Second, DFT calculations have revealed generalized stacking fault energies (GSFE) of HfNbTiZr and chemically ordered and disordered AlCrMoTi. The results revealed an increased mean unstable stacking fault energy $\overline{\gamma}_{\mathrm{usf}}$ as well as increased fluctuations of γ_{usf} in AlCrMoTi compared to HfNbTiZr. The GSFE can be interpreted within a model where the GSFE serve as a stand-in for an energy landscape felt by moving dislocations (see, e.g.,[39]). The energy landscape model combined with the GSFE results from this work implies that the fluctuations of the GSFE serve as dislocation pinning points and could thus explain the strength of AlCrMoTi by a decreased dislocation mobility.

The appearance of a non-zero antiphase boundary energy APBE in chemically ordered AlCrMoTi provides an alternative explanation for a decreased dislocation mobility in this alloy. However, even if the connection between dislocation mobility and GSFE fluctuations is reasonable, a fundamentally derived theory describing the interaction between dislocations and chemical fluctuations is lacking.

The uncertainty of the dislocation solute interaction leads to uncertainties evolving when applying a second model (MC-I) from Maresca and Curtin[35], which connects the strength of random alloys with the screw dislocation mobility. The model is applied with material quantities from this work for HfNbTiZr and AlCrMoTi. The model predicts that cross-kink strengthening is proportionally stronger in HfNbTiZr than in AlCrMoTi. According to the MC-I model, the strength of HfNbTiZr is mainly defined by the Peierls mechanism and cross-kink failure. In contrast, the strength of AlCrMoTi is mainly defined by lateral kink glide and cross-kink failure, as predicted by the MC-I model.

Finally, the results of this work and their interpretation recommend that future studies focus on the interaction between dislocations and chemical fluctuations within the crystal matrix. This recommendation is based on the observation that averaged material quantities in HEA follow Vegard's law. Thus, the average material properties of HEA will always have average values compared to BCC metals and cannot explain outstanding mechanical properties. Thus, it is very likely, that the outstanding mechanical properties are hidden in the complex dislocation-solute interaction, which is exclusive to HEA.

Bibliography

[1] E. P. George, W. A. Curtin, C. C. Tasan, High entropy alloys: A focused review of mechanical properties and deformation mechanisms, Acta Materialia 188 (2020) 435–474.

[2] O. N. Senkov, D. B. Miracle, K. J. Chaput, J.-P. Couzinie, Development and exploration of refractory high entropy alloys—a review, Journal of materials research 33 (19) (2018) 3092–3128.

[3] O. N. Senkov, G. B. Wilks, J. M. Scott, D. B. Miracle, Mechanical properties of Nb25Mo25Ta25W25 and V20Nb20Mo20Ta20W20 refractory high entropy alloys, Intermetallics 19 (2011) 698–706.

[4] O. N. Senkov, J. M. Scott, S. V. Senkova, D. B. Miracle, C. F. Woodward, Microstructure and room temperature properties of a high-entropy TaNbHfZrTi alloy, Journal of Alloys and Compounds 509 (2011) 6043–6048.

[5] H. Chen, A. Kauffmann, S. Laube, I. C. Choi, R. Schwaiger, Y. Huang, K. Lichtenberg, F. Müller, B. Gorr, H. J. Christ, M. Heilmaier, Contribution of lattice distortion to solid solution strengthening in a series of refractory high entropy alloys, Metallurgical and Materials Transactions A 49 (2018) 772–781.

[6] G. Dirras, L. Lilensten, P. Djemia, M. Laurent-Brocq, D. Tingaud, J.-P. Couzinié, L. Perrière, T. Chauveau, I. Guillot, Elastic and plastic properties of as-cast equimolar TiHfZrTaNb high-entropy alloy, Materials Science and Engineering A 654 (2016) 30–38.

[7] L. Lilensten, J.-P. Couzinié, L. Perrière, A. Hocini, C. Keller, G. Dirras, I. Guillot, Study of a bcc multi-principal element alloy: Tensile and simple shear properties and underlying deformation mechanisms, Acta Materialia 142 (2018) 131–141.

[8] Y. D. Wu, Y. H. Cai, T. Wang, J. J. Si, J. Zhu, Y. D. Wang, X. D. Hui, A refractory Hf25Nb25Ti25Zr25 high-entropy alloy with excellent structural stability and tensile properties, Materials Letters 130 (2014) 277–280.

[9] H. Chen, A. Kauffmann, S. Seils, T. Boll, C. H. Liebscher, I. Harding, K. S. Kumar, D. V. Szabó, S. Schlabach, S. Kauffmann-Weiss, F. Müller, B. Gorr, H. J. Christ, M. Heilmaier, Crystallographic ordering in a series of Al-containing refractory high entropy alloys Ta–Nb–Mo–Cr–Ti–Al, Acta Materialia 176 (2019) 123–133.

[10] S. Laube, H. Chen, A. Kauffmann, S. Schellert, F. Müller, B. Gorr, J. Müller, B. Butz, H. J. Christ, M. Heilmaier, Controlling crystallographic ordering in Mo–Cr–Ti–Al high entropy alloys to enhance ductility, Journal of Alloys and Compounds 823 (2020) 153805.

[11] H. Chen, Gefüge und eigenschaften von äquiatomaren legierungen aus dem system Ta-Nb-Mo-Cr-Ti-Al.

[12] P. M. Anderson, J. P. Hirth, J. Lothe, Theory of dislocations, Cambridge University Press, 2017.

[13] D. Hull, D. J. Bacon, Introduction to dislocations, Vol. 37, Elsevier, 2011.

[14] D. Caillard, J.-L. Martin, Thermally activated mechanisms in crystal plasticity, Elsevier, 2003.

[15] R. Peierls, The size of a dislocation, Proceedings of the Physical Society 52 (1940) 34–37.

[16] J. W. Christian, V. Vítek, Dislocations and stacking faults, Reports on Progress in Physics 33 (1970) 307–411.

[17] B. Escaig, Sur l'origine de la limite élastique des métaux cubiques centrés a basse température, Le Journal de Physique Colloques 27 (1966) C3–205.

[18] V. Vitek, F. Kroupa, Dislocation theory of slip geometry and temperature dependence of flow stress in bcc metals, Physica Status Solidi (B) 18 (1966) 703–713.

[19] M. S. Duesbery, The influence of core structure on dislocation mobility, Philosophical Magazine 19 (1969) 501–526.

[20] A. S. Argon, strengthening mechanisms in crystal plasticity, OUP Oxford, 2007.

[21] A. Seeger, Peierls barriers, kinks, and flow stress: Recent progress, Zeitschrift für Metallkunde 93 (2013) 760–777.

[22] A. Seeger, U. Holzwarth, Slip planes and kink properties of screw dislocations in high-purity niobium, Philosophical Magazine 86 (2006) 3861–3892.

[23] D. Brunner, J. Diehl, The use of stress-relaxation measurements for investigations on the flow stress of α-iron, Physica Status Solidi (a) 104 (1987) 145–155.

[24] D. Brunner, Comparism of flow-stress measurements on high-purity tungsten single crystals with the kink-pair theory, Materials Transactions 41 (1999) 152–160.

[25] L. Hollang, M. Hommel, A. Seeger, The flow stress of ultra-high-purity molybdenum single crystals, Physica Status Solidi (A) 160 (1997) 329–354.

[26] M. Werner, Temperature and strain-rate dependence of the flow stress of ultrapure tantalum single crystals, Physica Status Solidi (A) 104 63–78.

[27] J.-P. Couzinié, L. Lilensten, Y. Champion, G. Dirras, L. Perrière, I. Guillot, On the room temperature deformation mechanisms of a TiZrHfNbTa refractory high-entropy alloy, Materials Science and Engineering A 645 (2015) 255–263.

[28] J. W. Christian, Some surprising features of the plastic deformation of body-centered cubic metals and alloys, Metallurgical transactions A 14 (1983) 1237–1256.

[29] R. J. Arsenault, A. Lawley, Work hardening and dislocation structure in Ta and Ta-base alloys, The Philosophical Magazine: A Journal of Theoretical Experimental and Applied Physics 15 (135) (1967) 549–565.

[30] S. Takeuchi, E. Furubayashi, T. Taoka, Orientation dependence of yield stress in 4.4% silicon iron single crystals, Acta Metallurgica 15 (1967) 1179–1191.

[31] R. A. Foxall, C. D. Statham, Dislocation arrangements in deformed single crystals of niobium-molybdenum alloys and niobium-9 at.% rhenium, Acta Metallurgica 18 (1970) 1147–1158.

[32] F. G. Coury, M. Kaufman, A. J. Clarke, Solid-solution strengthening in refractory high entropy alloys, Acta Materialia 175 (2019) 66–81.

[33] C. Lee, F. Maresca, R. Feng, Y. Chou, T. Ungar, M. Widom, K. An, J. D. Poplawsky, Y. C. Chou, P. K. Liaw, W. A. Curtin, Strength can be controlled by edge dislocations in refractory high-entropy alloys, Nature Communications 12 (2021) 6–13.

[34] F. Wang, G. H. Balbus, S. Xu, Y. Su, J. Shin, P. F. Rottmann, K. E. Knipling, J. C. Stinville, L. H. Mills, O. N. Senkov, I. J. Beyerlein, T. M. Pollock, D. S. Gianola, Multiplicity of dislocation pathways in a refractory multiprincipal element alloy, Science 370 (2020) 95–101.

[35] F. Maresca, W. A. Curtin, Theory of screw dislocation strengthening in random bcc alloys from dilute to “high-entropy” alloys, Acta Materialia 182 (2020) 144–162.

[36] F. Maresca, W. A. Curtin, Mechanistic origin of high strength in refractory bcc high entropy alloys up to 1900k, Acta Materialia 182 (2020) 235–249.

[37] S. I. Rao, E. Antillon, C. Woodward, B. Akdim, T. A. Parthasarathy, O. N. Senkov, Solution hardening in body-centered cubic quaternary alloys interpreted using suzuki's kink-solute interaction model, Scripta Materialia 165 (2019) 103–106.

[38] A. Ghafarollahi, F. Maresca, W. A. Curtin, Solute/screw dislocation interaction energy parameter for strengthening in bcc dilute to high entropy alloys, Modelling and Simulation in Materials Science and Engineering 27 (2019) 085011.

[39] D. Utt, S. Lee, A. Stukowski, S. H. Oh, G. Dehm, K. Albe, Jerky motion of dislocations in high-entropy alloys: The linkage between local Peierls stress fluctuations and dislocation mobility, arXiv preprint arXiv:2007.11489 (2020).

[40] F. Körmann, M. H. F. Sluiter, Interplay between lattice distortions, vibrations and phase stability in NbMoTaW high entropy alloys, Entropy 18 (2016).

[41] G. Kresse, J. Furthmüller, Efficient iterative schemes for ab initio total-energy calculations using a plane-wave basis set, Physical Review B 54 (1996) 11169–11186.

[42] G. Kresse, J. Furthmüller, Efficiency of ab-initio total energy calculations for metals and semiconductors using a plane-wave basis set, Computational Materials Science 6 (1996) 15–50.

[43] P. C. Hohenberg, W. Kohn, Inhomogeneous electron gas, Physical Review Letters 7 (1964) 1912–1919.

[44] W. Kohn, L. J. Sham, Self-consistent equations including exchange and correlation effects, Physical Review 140 (1965) A1133.

[45] N. W. Ashcroft, D. N. Mermin, Solid state physics (german edition Festkörperphysik) (2013).

[46] W. A. Curtin, S. I. Rao, C. Woodward, Progress and challenges in the theory and modeling of complex concentrated alloys, MRS Bulletin 47 (2022) 151–157.

[47] B. L. Gyorffy, Coherent-potential approximation for a nonoverlapping-muffin-tin-potential model of random substitutional alloys, Physical Review B 5 (1972) 2382–2384.

[48] C. Varvenne, A. Luque, W. A. Curtin, Theory of strengthening in fcc high entropy alloys, Acta Materialia 118 (2016) 164–176.

[49] C. Jiang, B. P. Uberuaga, Efficient ab initio modeling of random multicomponent alloys, Physical Review Letters 116 (2016) 1–5.

[50] A. Zunger, S.-H. Wei, L. G. Ferreira, E. Bernard, Physical Review Letters 65 (1989) 353–356.

[51] A. Van de Walle, P. Tiwary, M. De Jong, D. Olmsted, M. Asta, A. Dick, D. Shin, Y. Wang, L.-Q. Chen, Z.-K. Liu, Efficient stochastic generation of special quasirandom structures, Calphad 42 (2013) 13–18.

[52] J. Sanchez, F. Ducastelle, D. Gratias, Generalized cluster description of multicomponent systems, Physica A 128 (1984) 334–350.

[53] W. H. Press, B. P. Flannery, S. A. Teukolsky, W. T. Vetterling, Numerical recipes, 628 cambridge university press, New York (1986).

[54] A. H. Larsen, J. J. Mortensen, J. Blomqvist, I. E. Castelli, R. Christensen, M. Dułak, J. Friis, M. N. Groves, B. Hammer, C. Hargus, E. D. Hermes, P. C. Jennings, P. B. Jensen, J. Kermode, J. R. Kitchin, E. L. Kolsbjerg, J. Kubal, K. Kaasbjerg, S. Lysgaard, J. B. Maronsson, T. Maxson, T. Olsen, L. Pastewka, A. Peterson, C. Rostgaard, J. Schiøtz, O. Schütt, M. Strange, K. S. Thygesen, T. Vegge, L. Vilhelmsen, M. Walter, Z. Zeng, K. W. Jacobsen, The atomic simulation environment—a Python library for working with atoms, Journal of Physics: Condensed Matter 29 (2017) 273002.

[55] C. Marker, S. L. Shang, J. C. Zhao, Z. K. Liu, Effects of alloying elements on the elastic properties of bcc Ti-X alloys from first-principles calculations, Computational Materials Science 142 (2018) 215–226.

[56] Y. Le Page, P. Saxe, Symmetry-general least-squares extraction of elastic data for strained materials from ab initio calculations of stress, Physical Review B 65 (2002) 1–14.

[57] J. A. Łopuszyński Michał and Majewski, Ab initio calculations of third-order elastic constants and related properties for selected semiconductors, Physical Review B 76 (2007) 45202.

[58] V. Vitek, Intrinsic stacking faults in body-centred cubic crystals, Philosophical Magazine 18 (1968) 773–786.

[59] D. Rodney, L. Ventelon, E. Clouet, L. Pizzagalli, F. Willaime, Ab initio modeling of dislocation core properties in metals and semiconductors, Acta Materialia 124 (2017) 633–659.

[60] W. G. Nöhring, W. A. Curtin, Design using randomness: a new dimension for metallurgy, Scripta Materialia 187 (2020) 210–215.

[61] W. P. Huhn, M. Widom, Prediction of a2 to b2 phase transition in the high-entropy alloy mo-nb-ta-w, JOM 65 (2013) 1772–1779.

[62] F. Körmann, A. V. Ruban, M. H. Sluiter, Long-ranged interactions in bcc NbMoTaW high-entropy alloys, Materials Research Letters 5 (1) (2017) 35–40.

[63] M. Widom, W. P. Huhn, S. Maiti, W. Steurer, Hybrid monte carlo/molecular dynamics simulation of a refractory metal high entropy alloy, Metallurgical and Materials Transactions A 45 (2014) 196–200.

[64] Y. Ikeda, B. Grabowski, F. Körmann, Ab initio phase stabilities and mechanical properties of multicomponent alloys: A comprehensive review for high entropy alloys and compositionally complex alloys, Materials Characterization (2018) 1–48.

[65] W. Nolting, W. Nolting, Grundkurs Theoretische Physik. 6. Statistische Physik, Springer, 2014.

[66] B. Gorr, M. Azim, H.-J. Christ, T. Mueller, D. Schliephake, M. Heilmaier, Phase equilibria, microstructure, and high temperature oxidation resistance of novel refractory high-entropy alloys, Journal of Alloys and Compounds 624 (2015) 270–278.

[67] N. Guo, L. Wang, L. Luo, X. Li, Y. Su, J. Guo, H. Fu, Microstructure and mechanical properties of refractory MoNbHfZrTi high-entropy alloy, Materials Design 81 (2015) 87–94.

[68] Fazakas, V. Zadorozhnyy, L. K. Varga, A. Inoue, D. V. Louzguine-Luzgin, F. Tian, L. Vitos, Experimental and theoretical study of Ti20Zr20Hf20Nb20X20 (X=V or Cr) refractory high-entropy alloys, International Journal of Refractory Metals and Hard Materials 47 (2014) 131–138.

[69] O. N. Senkov, G. B. Wilks, D. B. Miracle, C. P. Chuang, P. K. Liaw, Refractory high-entropy alloys, Intermetallics 18 (2010) 1758–1765.

[70] S. F. Pugh, Xcii. relations between the elastic moduli and the plastic properties of polycrystalline pure metals, The London, Edinburgh, and Dublin Philosophical Magazine and Journal of Science 45 (1954) 823–843.

[71] D. G. Pettifor, M. Aoki, Bonding and structure of intermetallics: a new bond order potential, Philosophical Transactions of the Royal Society of London. Series A: Physical and Engineering Sciences 334 (1991) 439–449.

[72] M. De Jong, W. Chen, T. Angsten, A. Jain, R. Notestine, A. Gamst, M. Sluiter, C. K. Ande, S. Van Der Zwaag, J. J. Plata, C. Toher, S. Curtarolo, G. Ceder, K. A. Persson, M. Asta, Charting the complete elastic properties of inorganic crystalline compounds, Scientific Data 2 (2015) 1–13.

[73] S. A. Kube, S. Sohn, D. Uhl, A. Datye, A. Mehta, J. Schroers, Phase selection motifs in high entropy alloys revealed through combinatorial methods: Large atomic size difference favors bcc over fcc, Acta Materialia 166 (2019) 677–686.

[74] L. Casillas-Trujillo, U. Jansson, M. Sahlberg, G. Ek, M. M. Nygård, M. H. Sørby, B. C. Hauback, I. A. Abrikosov, B. Alling, Interstitial carbon in bcc

HfNbTiVZr high-entropy alloy from first principles, Physical Review Materials 4 (2020) 123601.

[75] Z. Lei, X. Liu, Y. Wu, H. Wang, S. Jiang, S. Wang, X. Hui, Y. Wu, B. Gault, P. Kontis, D. Raabe, L. Gu, Q. Zhang, H. Chen, H. Wang, J. Liu, K. An, Q. Zeng, T. G. Nieh, Z. Lu, Enhanced strength and ductility in a high-entropy alloy via ordered oxygen complexes, Nature 563 (2018) 546–550.

[76] E. Antillon, C. Woodward, S. I. Rao, B. Akdim, T. A. Parthasarathy, Chemical short range order strengthening in a model fcc high entropy alloy, Acta Materialia 190 (2020) 29–42.

[77] S. Xu, Y. Su, L. T. W. Smith, I. J. Beyerlein, Frank-read source operation in six body-centered cubic refractory metals, Journal of the Mechanics and Physics of Solids 141 (2020) 104017.

[78] J. Ding, Q. Yu, M. Asta, R. O. Ritchie, Tunable stacking fault energies by tailoring local chemical order in CrCoNi medium-entropy alloys, Proceedings of the National Academy of Sciences of the United States of America 115 (2018) 8919–8924.

[79] S. Yin, J. Ding, M. Asta, R. O. Ritchie, Ab initio modeling of the energy landscape for screw dislocations in body-centered cubic high-entropy alloys, npj Computational Materials 6 (2020).

[80] F. R. N. Nabarro, Dislocations in a simple cubic lattice, Proceedings of the Physical Society of London 59 (1947) 256–272.

[81] A. N. Stroh, Dislocations and cracks in anisotropic elasticity, Philosophical Magazine 3 (1958) 625–646.

[82] A. Giannattasio, M. Tanaka, T. D. Joseph, S. G. Roberts, An empirical correlation between temperature and activation energy for brittle-to-ductile transitions in single-phase materials, Physica Scripta T T128 (2007) 87–90.

[83] A. Giannattasio, S. G. Roberts, Strain-rate dependence of the brittle-to-ductile transition temperature in tungsten, Philosophical Magazine 87 (2007) 2589–2598.

[84] T. D. Swinburne, S. L. Dudarev, Kink-limited Orowan strengthening explains the brittle to ductile transition of irradiated and unirradiated bcc metals, Physical Review Materials 2 (2018) 073608.

[85] E. A. Brandes, H. T. Greenaway, H. E. N. Stone, Ductility in chromium, Nature 178 (4533) (1956) 587–587.

[86] V. V. Satya Prasad, R. G. Baligidad, A. A. Gokhale, Niobium and other high temperature refractory metals for aerospace applications, in: Aerospace Materials and Material Technologies, Springer, 2017, pp. 267–288.

[87] C. R. Weinberger, G. J. Tucker, S. M. Foiles, Peierls potential of screw dislocations in bcc transition metals: Predictions from density functional theory, Physical Review B 87 (2013) 054114.

[88] Q. J. Li, H. Sheng, E. Ma, Strengthening in multi-principal element alloys with local-chemical-order roughened dislocation pathways, Nature Communications 10 (2019) 1–11.

[89] Z. Pei, B. Dutta, F. Körmann, M. Chen, Hidden effects of negative stacking fault energies in complex concentrated alloys, Physical Review Letters 126 (2021) 255502.

[90] M. Shih, J. Miao, M. Mills, M. Ghazisaeidi, Stacking fault energy in concentrated alloys, Nature Communications 12 (2021) 1–10.

[91] J. R. Rice, Dislocation nucleation from a crack tip: An analysis based on the peierls concept, Journal of the Mechanics and Physics of Solids 40 (1992) 239–271.

[92] J. R. Rice, G. E. Beltz, The activation energy for dislocation nucleation at a crack, Journal of the Mechanics and Physics of Solids 42 (1994) 333–360.

[93] X. Li, W. Li, D. L. Irving, L. K. Varga, L. Vitos, S. Schönecker, Ductile and brittle crack-tip response in equimolar refractory high-entropy alloys, Acta Materialia 189 (2020) 174–187.

[94] M. J. Marcinkowski, H. Chessin, Relationship between flow stress and atomic order in the FeCo alloy, Philosophical Magazine 10 (1964) 837–859.

[95] J.-P. Couzinié, G. Dirras, Body-centered cubic high-entropy alloys: From processing to underlying deformation mechanisms, Materials Characterization 147 (2019) 533–544.

[96] J. D. Eshelby, The interaction of kinks and elastic waves, The royal society publishing 266 (1962) 222–246.

[97] D. Brunner, J. Diehl, Strain-rate and temperature dependence of the tensile flow stress of high-purity a-iron above 250 k (regime i) studied by means of stress-relaxation tests, Physica Status Solidi (a) 124 (1991) 155–170.

[98] M. Boleininger, M. Gallauer, S. L. Dudarev, T. D. Swinburne, D. R. Mason, D. Perez, Statistical mechanics of kinks on a gliding screw dislocation, Phys. Rev. Research 2 (2020) 043254.

[99] H. Eckerlin, Kandler, Structure data of elements and intermetallic phases · Ac - Mn: Datasheet from Landolt-Börnstein.

[100] M. C. Gao, P. Gao, J. A. Hawk, L. Ouyang, D. E. Alman, M. Widom, Computational modeling of high-entropy alloys: Structures, thermodynamics and elasticity, Journal of Materials Research 32 (2017) 3627–3641.

List of Figures

List of Tables

A Appendix

A.1 Peculiarities of DFT elastic constant calculations for HEA using the SQS approach

This section investigates the influence of the SQS size and preperformed relaxations on elastic constants. In this context, "SQS size" means how many atoms the SQS contains. "Preperformed relaxations" means, in the context of this section, the number of degrees of freedom that have been used in order to relax the SQS (or SSOS) before the actual elastic constant calculation (see Section 2.4).
Figure A.1 shows DFT calculated elastic constants from different calculation sets, which differ in N_{atoms} and the preperformed relaxations. The data reveal an increasing C_{11} with increasing N_{atoms}, while C_{12} and C_{44} show no N_{atoms} dependency. The increase of $C_{11}(N_{\text{atoms}} = 4)$ to $C_{11}(N_{\text{atoms}} = 128)$ is $\approx 5\%$, while the standard deviation of C_{11} from the largest SQS is $\approx 2\%$. Further DFT calculations suffer intrinsically from uncertainties (Section 2.1). DFT calculations are valid at 0K, and elastic constants usually decrease with increasing temperature[99]. Consequently, the presented results allow us to argue that the results from the $N_{\text{atoms}} = 4$ SQS set are accurate enough. In this context, it is important to mention that within this calculation set, only one SQS containing four atoms has been used. The $N_{\text{atoms}} = 4$ SQS has been permutated three times (AlCrMoTi, AlCrTiMo, AlMoTiCr) since the elastic constants are symmetry-invariant by all other permutations. The resulting standard deviation of $\overline{C}_{11}$ is high $(16\ \text{GPa})$, while the standard deviations of C_{12} and C_{44} are not increased compared to values from larger SQS. This indicates that the periodicity error in the investigated

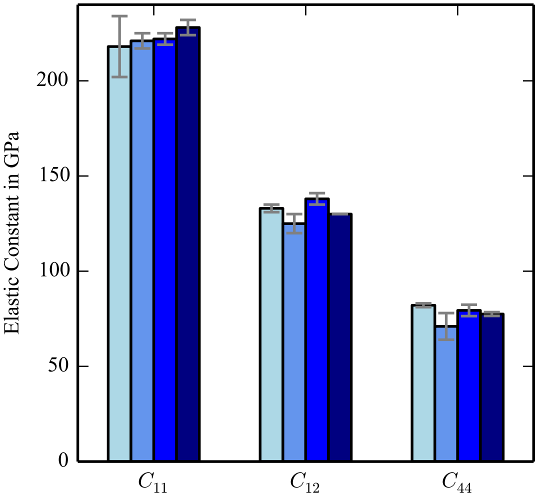

Figure A.1: Cubic elastic constants of AlCrMoTi **(left)** and HfNbTiZr **(right)**. The results are obtained by calculation sets differing between each other in N_{atoms} and the number of degrees of freedom used for SQS relaxation. N_{atoms} are The results from light to dark blue are obtained using SQS's with N_{atoms} : 4, 16, 64 and 128. The 4, 16, and 128 SQS have been totally relaxed before the actual elastic constant calculation, while the 64-atom SQS has been relaxed with respect to cell volume and atomic positions.

four-atom SQS size especially affects C_{11}. However, this observation does not allow us to make a general statement since, besides the number of atoms, the shape (or symmetry) of the used SQS is expected to influence the periodicity error of specific quantities. This statement is supported by the data from the $N_{\text{atoms}} = 16$ calculation set. Here, five permutations have been used to calculate the elastic constants since the elastic constants are symmetry invariant to further permutations. In this case, the standard deviations of C_{12} and C_{44} are slightly increased compared to the one of C_{11} and are increased compared to the standard deviations of C_{12} and C_{44} from the calculation set with the smaller $N_{\text{atom}} = 4$ SQS. The data further reveal, that $\overline{C}_{12}$ and $\overline{C}_{44}$ from the 16 atom SQS set are smaller compared to $\overline{C}_{12}$ and $\overline{C}_{44}$ from the other investigated calculation sets. The calculation sets with $N_{\text{atom}} = 64$ and $N_{\text{atom}} = 128$ reveal elastic constants

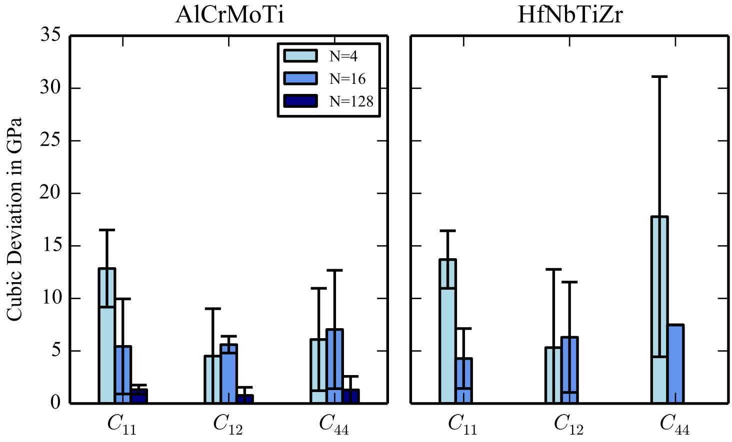

Figure A.2: Deviation of elastic constants from cubic symmetry.

with comparable low standard deviations (0 - 4 GPa). Both calculation sets use several different SQS instead of permutations of the same SQS to investigate the periodicity error. The resulting $\overline{C}_{11}$ is increased by $\approx 3\%$ from the $N_{\text{atom}} = 64$ to the $N_{\text{atom}} = 128$ calculations set, while $\overline{C}_{12}$ and $\overline{C}_{44}$ are increased by $\approx 6\%$ and $\approx 3\%$. Note that in the $N_{\text{atom}} = 64$ calculation set, only three (instead of nine) affine transformations per SQS have been applied. This means that the broken cubic symmetry of the SQS has been neglected in the $N_{\text{atom}} = 64$ atom calculation set. Therefore, the quality of the calculated elastic constants could be affected by the cubic deviation of the used SQS. However, the observed deviations between the 64 and 128-atom calculation sets can be considered negligible with respect to other expected inaccuracies, such as evolving from the DFT approach. Figure A.2 compares the averaged (within a particular calculation set) standard deviations of cubic equivalent elastic constants. This result shows that C_{11} is increasingly directional dependent with increasing SQS size.

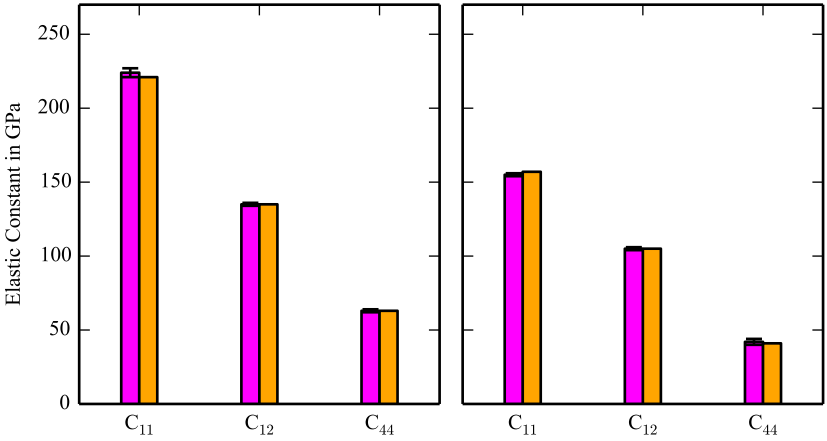

Figure A.3: Elastic constants calculated by DFT calculations with SSOS (magenta), SQS (orange) of AlCrMoNbTi (left) and HfNbTaTiZr (right). Error bars in the SSOS approach are from permutations of elements within one SSOS.

A.2 SQS vs SSOS approach

This section presents the results of two supercell approaches (SQS and SSOS) used to calculate the cubic elastic constants of two five-component BCC HEA, AlCrMoNbTi and HfNbTaTiZr. The SQS approach was used to obtain results for AlCrMoNbTi (125 atoms SQS) and HfNbTaTiZr (250 atoms SQS). The 125-atom SQS is given by[100], and the 250-atom SQS was generated using the ATAT toolkit[51]. The used SSOS consists of three 5-atom supercells and is given by[49]. Figure A.3 compares the different elastic constants results from the mentioned approaches. It shows that the deviations between the SSOS and the SQS results are $\lesssim 2.5$ %. The observed deviations are smaller than the expected uncertainties connected to the DFT - approach.

The results show that using the SSOS approach for elastic constant calculations of equimolar HEA is equivalent to using the SQS approach, but the latter requires much higher computational effort.

A.3 Yield stress vs temperature of BCC HEA

This section presents flow stress measurements of various BCC HEA from[32]. The experimental values were fitted using the function $\sigma = A(T - T_K)$.

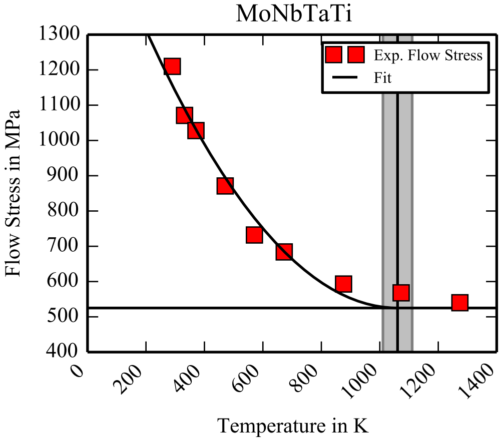

Figure A.4: Temperature vs flow stress of MoNbTaTi from compression tests[32] and theoretical fit function $\sigma = A(T - T_K)$.

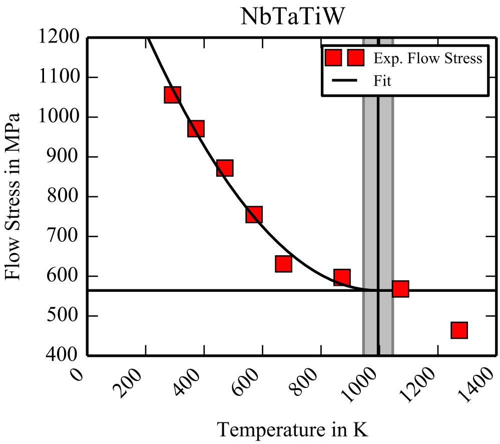

Figure A.5: Temperature vs flow stress of NbTaTiW from compression tests [32] and theoretical fit function $\sigma = A(T - T_K)$.

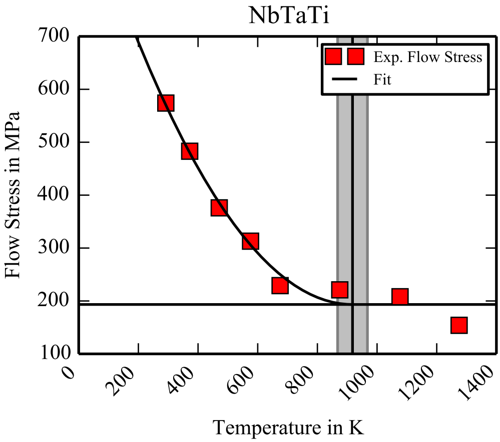

Figure A.6: Temperature vs flow stress of NbTaTi from compression tests [32] and theoretical fit function $\sigma = A(T - T_K)$.

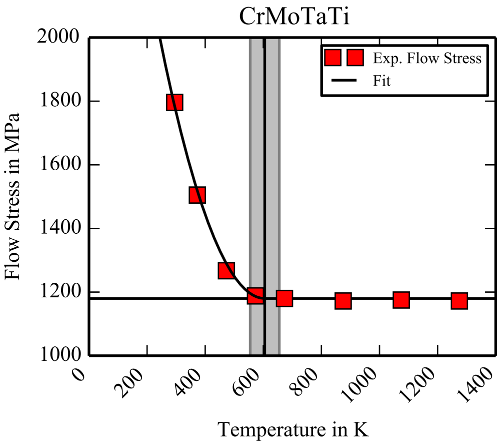

Figure A.7: Temperature vs flow stress of CrMoTaTi from compression tests[32] and theoretical fit function $\sigma = A(T - T_K)$.

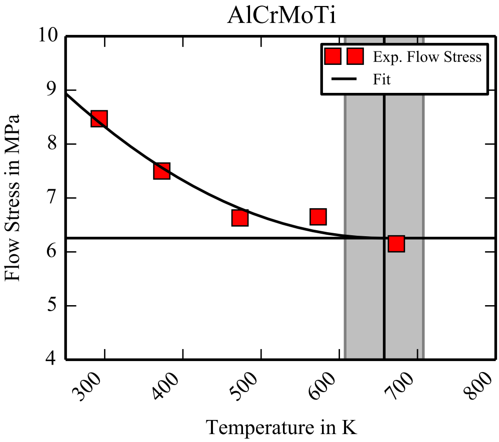

Figure A.8: Temperature vs flow stress of AlCrMoTi from nano-indentaion[5] and theoretical fit function $\sigma = A(T - T_K)$.

A.4 Lattice constants

Metal	a_0 from DFT [Å]	a_0 from Exp. [Å]
Al	3.2205	-
Cr	2.874	2.88
Fe	2.84	2.87
Hf	3.5 (own calc.)	3.559
Mo	3.1673	3.15
Nb	3.3209	3.3
Ta	3.3221	3.31
Ti	3.2516	3.276
V	2.9930	3.02
W	3.1870	3.16
Zr	3.5830	3.582

Table A.1: Lattice constants from DFT and experiment of different metals in BCC configuration. All DFT values are from Materials Project[72] except the one of Hf, which was calculated from this work. The experimental values have been extracted from[45] except the ones of Hf, Ti and Zr, which have been extracted from[4].